UNIVERSIDADE FEDERAL DO CEARÁ
CENTRO DE CIÊNCIAS
DEPARTAMENTO DE FÍSICA
PROGRAMA DE PÓS-GRADUAÇÃO EM FÍSICA

WELLINGTON CASTRO FERREIRA

OPTICAL AND STRUCTURAL PROPERTIES OF PEROVSKITE-RELATED STRUCTURES UNDER EXTREME CONDITIONS OF PRESSURE AND TEMPERATURE

FORTALEZA-CE

2020

WELLINGTON CASTRO FERREIRA

OPTICAL AND STRUCTURAL PROPERTIES OF PEROVSKITE-RELATED STRUCTURES UNDER EXTREME CONDITIONS OF PRESSURE AND TEMPERATURE

Ph.D. thesis presented to the Post-Graduation Program in Physics of the Federal University of Ceara as part of the requisites for obtaining the Degree of Doctor in Physics.

Advisor: Prof. Dr. Alejandro Pedro Ayala

FORTALEZA

2020

Dados Internacionais de Catalogação na Publicação
Universidade Federal do Ceará
Biblioteca Universitária
Gerada automaticamente pelo módulo Catalog, mediante os dados fornecidos pelo(a) autor(a)

F444o Ferreira, Wellington Castro.
Optical and Structural Properties of Perovskite-Related Structures Under Extreme Conditions of Pressure and Temperature / Wellington Castro Ferreira. – 2020.
120 f. : il. color.

Tese (doutorado) – Universidade Federal do Ceará, Centro de Ciências, Programa de Pós-Graduação em Física , Fortaleza, 2020.
Orientação: Prof. Dr. Alejandro Pedro Ayala.

1. Multiferroic compounds. 2. Halide perovskites. 3. Ruddlesden-Popper phase. 4. Structural phase transitions. 5. Electron-phonon coupling. I. Título.

CDD 530

WELLINGTON CASTRO FERREIRA

OPTICAL AND STRUCTURAL PROPERTIES OF PEROVSKITE-RELATED STRUCTURES UNDER EXTREME CONDITIONS OF PRESSURE AND TEMPERATURE

Ph.D. thesis presented to the Post-Graduation Program in Physics of the Federal University of Ceara as part of the requisites for obtaining the Degree of Doctor in Physics.
Advisor: Prof. Dr. Alejandro Pedro Ayala

Approval date: 27/03/2020.

THESIS COMMITTEE

Prof. Dr. Alejandro Pedro Ayala (Advisor)

Universidade Federal do Ceará (UFC)

Prof. Dr. Carlos William de Araújo Paschoal

Universidade Federal do Ceará (UFC)

Prof. Dr. Paulo de Tarso Cavalcante Freire

Universidade Federal do Ceará (UFC)

Prof. Dr. Ricardo Donizeth dos Reis

Laboratório Nacional de Luz Síncrotron (LNLS)

Prof. Dra. Ariete Righi

Universidade Federal de Minas Gerais (UFMG)

Dedication

To my wife Ivonilde Ribeiro.

Acknowledgments

I thank God for my life and for everything he has helped me to achieve, for force in darkens moments always showing me what matters in life.

I thank my wife, Ivonilde Ribeiro, for always supporting my decisions, understanding my constant absence, and believing in my dreams. I thank her for the good moments, because they made us happy, and also for the bad ones because they made us stronger.

I would like to thank my family for their support. To my parents, João Costa and Francisca Castro, and my brothers, Virgulino, Warlington, and Joanny, despite the distance, they have always supported me.

I am very grateful to my advisor Professor Alejandro Pedro Ayala, for having accepted the challenge of guiding me and for trusting me over the years. Thanks for always being present with patience, dedication and for giving me good projects to work on, thanks for the motivation, thanks for showing me what I could do. Some people are lucky for having a good boss as a scientist, some are lucky for having a good boss as a person; I was lucky for having both.

I would like to thank professor Carlos William Paschoal for the collaboration with the multiferroic perovskites samples and for the valuable comments and discussions that we had, and that contributed significantly to this final work.

I would like to thank Professor Pierre Fantine for the $Bi_5FeTi_3O_{15}$ sample.

I would like to thank Dieric Abreu for his help in synthesizing samples from the Ruddlesden-Popper family and by our dialogues about how we can become better researchers. Thanks for everything my friend!

I would like to thank Gelson Rodrigues for your collaboration with the pressure measurements of the $Bi_5FeTi_3O_{15}$ sample.

I would like to thank Mayra Alexandra for your collaboration with the Cs_4PbBr_6 synthesis.

I would like to thank Bruno Sousa and Fabio Medeiros for your friendship and help throughout my Ph.D., especially in the instrumental part, as well as for the ideas and discussions about experiments and results.

I would like to thank Professor Gardênia for her friendship and especially for introducing me to Professor Alejandro's group.

I would like to thank the professor Eduardo Girão for his friendship and discussions about academic life over those years.

I thank the other colleagues in the group who contributed with help in instrumentation and in the use of some equipments, in addition to good confraternization moments and valuable discussions throughout the thesis; Keilla Façanha, Nailson Vasconcelos, Renata Santos, Beatriz Pinheiro, Laura Vidal, Silmara Alves, Yara Santiago, Wendell Saraiva, Ana Georgina, and Vasco Stascxak.

Solomon once said "There are friends who sticks closer than brothers" (Proverbs 18.24). João Victor and Nubia Ribeiro, you are an example of this. Thanks for having received me in Fortaleza, and for the strong friendship throughout our academic career! Dr. João Victor, thanks for introducing me to the spectroscopy area!

I would like to thank my friends Fabrício Vasconcelos and Paloma Vieira for the friendly interaction and conversations throughout my academic career.

This study was financed in part by the Coordenação de Aperfeiçoamento de Pessoal de Nível Superior - Brasil (CAPES) - Finance Code 001. Therefore, I would like to thank the research funding agencies that gave me financial support for activities carried out in this doctorate, CAPES, CNPq, FUNCAP, and the Brazilian Synchrotron Light Laboratory (LNLS).

RESUMO

Blocos octaédricos são a principal característica geométrica de estruturas relacionadas à perovskita, e podem sofrer distorções pela aplicação de campos externos. Muitas propriedades físicas, tais como ferroeletricidade, piezoeletricidade, multiferroicidade, e propriedades fotovoltaícas podem estar relacionadas aos octaedros nessas estruturas. Mudanças nessas propriedades físicas podem ser esperadas em condições de altas pressões e altas temperaturas, uma vez que os deslocamentos dos cátions e distorções nos octaedros são sensíveis a pressão e temperatura. Portanto, experimentos de alta pressão/temperatura são uma maneira direta e robusta de explorar as propriedades estruturais, ópticas e ferróicas de materiais do tipo perovskita. Nesta tese estudamos várias estruturas deste tipo sob condições extremas de pressão e temperatura. Dois grupos de perovskitas foram estudadas, materiais multiferróicos e o perovskitas de haletos. No grupo dos materiais multiferróicos foram considerados um membro de quatro camadas da família Aurivillius ($Bi_5FeTi_3O_{15}$ (BFTO)), e uma perovskita quadrupla ($CaMn_7O_{12}$ (CMO)). Apesar do interesse tecnológico dos compostos multiferróicos, estudos reportando a estabilidade estrutural em perovskitas multiferróicas complexas sob pressão hidrostática são escassos. Esta tese visa preencher esta lacuna de informações, investigando as transições de fase induzidas por pressão do BFTO e CMO. Para o BFTO, uma rica sequência de transições de fase foi verificada combinando espectroscopia Raman com difração de raios-X síncrotron de pó. Ambas as técnicas confirmam a existência de três transições de fase, e análises de strain induzidas pela distorção ortorrômbica nos permitiram inferir a ordem de duas destas transições. Por sua vez, mostramos que o CMO experimenta ao menos duas transições de fase estruturais até 19 Gpa, o que é incomum para perovskitas quádruplas.

No grupo das perovskitas de haleto foram consideradas o composto da fase Ruddlesden-Popper $Cs_2PbI_2Cl_2$ e a perovskita do tipo 0-D Cs_4PbBr_6. As estruturas de haletos metálicas tem surgido como o estado-da-arte dos matérias fotovoltaicos, devido às suas extraordinárias propriedades optoeletrônicas, baixo custo e métodos simples de fabricação baseados em soluções. Medidas de fotoluminescência (PL) e Raman Stokes e anti-Stokes dependentes da temperatura na faixa de (300 - 16 K) foram realizadas para o composto $Cs_2PbI_2Cl_2$. Os espectros Raman não revelaram evidencia de transição de fase estrutural, entretanto, observamos características de Raman de segunda ordem e uma nova banda PL surgindo em baixas temperaturas. Análises da largura de linha da emissão em função da temperatura nos permitiram

estabelecer que um forte acoplamento elétron-fônon ainda não relatado para este tipo de perovskitas de halogeneto está presente na fase $Cs_2PbI_2Cl_2$. Por fim, discutimos as mudanças na estrutura e no comportamento da PL de monocristais (SCs) da perovskita 0D luminescente Cs_4PbBr_6 sob condições de alta pressões. A análise estrutural demonstrou que sua estrutura passa por duas transições de fase em torno de 3,2 e 4,5 GPa. A primeira transição de fase também foi observada em nanocristais, mas a segunda parece ser característica de cristais bulk. Em nosso (SCs) bulk de Cs_4PbBr_6 a emissão da PL é completamente suprimida em 3,5 GPa, indicando que nessa estrutura a fase de alta pressão (monoclínica) não produz uma condição favorável para o fenômeno da PL. Alinhado com os outros estudos de sistemas de perovskitas 0D sob condições de alta pressão, a PL do nosso sistema é muito semelhante ao relatado para o composto $Cs_3Bi_2I_9$. Propomos que a PL dos SCs luminescentes de Cs_4PbBr_6 possam estar associadas com a distribuição de diferentes tamanhos de quantum dots ou nanocristais (NCs) de $CsPbBr_3$ incorporados no Cs_4PbBr_6. Nossas descobertas fornecem informações valiosas sobre o mecanismo de luminescência, fazendo incursões significativas na origem da fotoluminescência na região do verde, compreendendo e lançando luz sobre as características estruturais e propriedades de PL dos cristais luminosos de Cs_4PbBr_6 sob condições extremas.

Palavras-chave: Compostos multiferróicos, Perovskitas de haleto, Fase Ruddlesden-Popper, Transições de fase estrutural, Acoplamento elétron-fônon.

ABSTRACT

Octahedra blocks are the main geometrical features of perovskite-related structures and can undergo distortions by application of external fields. Many physical properties, such as ferroelectricity, piezoelectricity, multiferroicity and photovoltaic properties can be related to the octahedra in these structures. Changes in these physical properties can be expected at high-pressure and high-temperature conditions once cations displacements and octahedral distortions are temperature and pressure-sensitive. Therefore, high-pressure/temperature experiments are a straightforward and robust way to explore the structural, optical, and ferroic properties of perovskites-related materials. In this thesis, we studied several perovskites-related structures under extreme conditions of pressure and temperature. Two groups of perovskites were studied, multiferroics materials and halide perovskites. In the multiferroic materials group, a four-layered member of the Aurivillius family ($Bi_5FeTi_3O_{15}$ (BFTO)), and a quadruple perovskite ($CaMn_7O_{12}$ (CMO)) were considered. Despite the technological interest of multiferroic compounds, studies reporting the structural stability in complex multiferroic perovskites under hydrostatic pressure are scarce. This thesis aims to fill this gap of information by investigating the pressure-induced phase transitions of BFTO and CMO. For BFTO, a rich sequence of phase transitions was identified by combining Raman spectroscopy with synchrotron powder x-ray diffraction. Both techniques confirm the existence of three phase transition, and the analysis of the strain induced by the orthorhombic distortion allowed us to infer the order of two of them. In turn, we showed that CMO undergoes at least two structural phase transitions up to 19 GPa, which is unusual for quadruple perovskites.

In the halide perovskites group, the Ruddlesden-Popper compound $Cs_2PbI_2Cl_2$, and the 0-D perovskite Cs_4PbBr_6 were considered. Metal halide structures have emerged as a state-of-the-art photovoltaic material owing to their extraordinary optoelectrical properties, low cost, and simple solution-based fabrication methods. Temperature-dependent photoluminesce (PL), and Stokes-Anti-Stokes Raman measurements in the range (300 – 16 K) were performed for the $Cs_2PbI_2Cl_2$ compound. The Raman spectra revealed no evidence of structural phase transitions; however, we observed second-order Raman features, and a new PL band arising at low temperatures. Analyses of the temperature-dependent emission linewidth allowed us to

establish that a strong electron-phonon coupling not yet reported for this kind of halide perovskites is present in the $Cs_2PbI_2Cl_2$ phase. Finally, we discuss the changes in the structure and the PL behavior of luminescent Cs_4PbBr_6 single crystals (SCs) under high-pressure conditions. The structural analysis demonstrated that its structure undergoes two phase transitions around 3.2 and 4.5 GPa. The first phase transition was also observed in nanocrystals, but the second seems to be characteristic of bulk crystals. In our Cs_4PbBr_6 bulk SCs, the PL emission is completely suppressed at 3.5 GPa, indicating that in this structure, the high-pressure (monoclinic) phase does not produce a favorable condition for the PL phenomena. In line with the other 0D perovskites systems studies under high-pressure conditions, the PL of our system is very similar to the one reported for $Cs_3Bi_2I_9$. We proposed that the PL of the luminescent Cs_4PbBr_6 SCs can be associated with the different size distribution of quantum dots or NCs of $CsPbBr_3$ embedded in Cs_4PbBr_6. Our findings provide valuable insight into the luminescence mechanism making significant inroads into green photoluminescence origin understanding and shedding light on the structural characteristics and PL properties of luminescent Cs_4PbBr_6 single crystals under extremes conditions.

Keywords: Multiferroic compounds, Halide perovskites, Ruddlesden-Popper phase, Structural phase transitions, Electron-phonon coupling.

LIST OF FIGURES

LIST OF TABLES

TABLE OF CONTENTS

1. Introduction

The crystal structures encompassed by the term perovskite embrace a vast range of compounds, from the simple cubic 'aristotype' $SrTiO_3$ to cation-and anion deficient phases [1,2]. The main feature that makes the perovskite structures fascinating is the possibility to tune over wide ranges of their physical and chemical properties by relatively simple atomic substitutions [3]. As an example of this flexibility, we can quote the syntheses of perovskites in which the large cations are replaced by an organic molecule, such as in the inorganic-organic hybrid compound $(CH_3NH_3)PbX_3$ [4], where X is typically Cl, Br, I, or a combination of these anions. Recently, inorganic-organic hybrid compounds have drawn significant attention as the core of photovoltaic cells [5–7]. Therefore, depending on which atoms or molecules are arranged in the structure, perovskite materials exhibit different structures and interesting physical properties that have been intensively studied since the middle of the twentieth century [3]. So, it is this flexibility that makes the perovskite an important family of compounds, in which the easy replacement of any of the atoms (respecting the Goldschmidt tolerance factor [8]) can be used to modify physical properties in a controlled way.

Among the various applications fields and physical properties, two major areas have been in the focus of the scientific community: multiferroic perovskites [9], and, most recently, photovoltaic perovskites [10,11]. Multiferroics are a class of materials that simultaneously exhibit more than one primary ferroic ordering (ferroelectricity, ferromagnetism, ferroelasticity, or ferrotoroidicity) in the same phase [12]. The possibility of combining electrical and magnetic properties in a single phase (multiferroicity) and, mainly, the coupling between these properties (magnetoelectricity) has implied in great interest for these compounds [13]. In turn, photovoltaic perovskites have emerged as a promising class of functional materials for photovoltaic and optoelectronic applications with high efficiency and low costs [11]. In less than half a decade of rigorous research and development in perovskite solar cells, its efficiency has increased by up to 25.2% (certified PCE of PSCs), as can be found in the NREL PV chart https://www.nrel.gov/pv/assets/pdfs/best-research-cell-efficiencies.20191106.pdf.

.

The *in situ* high-pressure analysis is a valuable technique to shed light on the physical properties of perovskites [14,15]. Their interatomic distances and bond lengths can be adjusted, and pressure can thereby effectively tune the lattice and electronic structures, as well as their properties and functionalities [16–18]. In the last years, high-pressure science and technology have developed, and it is becoming a major area in the materials science field with an increasing number of discoveries that have been reported [19]. In this thesis, we investigate the structural and physical properties of multiferroic and photovoltaic perovskites under extreme conditions of pressure and temperature. In Chapter 1, a general review of the different perovskite structures and their variations is presented; then, we focus on multiferroic and photovoltaic perovskites and the effects of pressure on them. A description of the experimental apparatus used in the experiments is given in the methodology chapter. The results of the thesis are divided in four chapters, one for each studied sample.

In chapter 4, the structural stability of the multiferroic four-layer Aurivillius ceramic $Bi_5FeTi_3O_{15}$ (BFTO) under hydrostatic pressure was investigated in situ by synchrotron X-ray powder diffraction (SXRPD) and Raman spectroscopy. Measures performed up to 15 GPa allowed the identification of two well-defined structural phase transition. The ambient conditions orthorhombic phase transforms into a tetragonal one around 3.2 GPa, and around 7.5 GPa rises a new orthorhombic phase. Both phase transitions are evidenced by the pressure dependence of the lattice parameters and vibrational modes frequencies. The analysis of the induced strain indicates the transitions are, respectively, of second-order and first-order. Subtle changes in the Raman spectra and powder patterns suggest the onset of a new phase transition around 10.5 GPa.

In chapter 5, we investigated the pressure-induced structural phase transitions (SPT) in $CaMn_7O_{12}$ (CMO) quadruple perovskite by synchrotron X-ray powder diffraction. Despite the thorough discussion on the CMO ferroelectric and magnetic properties, few investigations were focused on the structural phase transitions (SPT) undergone by this compound. In this thesis, we show that CMO undergoes at least two SPT induced by hydrostatic pressure. CMO transforms successively into a monoclinic structure around 9.9 GPa and into another monoclinic phase for pressures higher than 13.3 GPa. For pressures above 17.0 GPa, subtle changes in the lattice parameters are observed, suggesting a new phase transformation of CMO.

In chapter 6, we address a 2D layered perovskite from the Ruddlesden-Popper family. A recent study has shown that $Cs_2PbI_2Cl_2$ has excellent stability to moisture and interesting optical properties. In this thesis, we present the synthesis as well as temperature-dependent anti-Stokes and Stokes Raman vibrational spectra measurements in the range (300 – 16 K) for $Cs_2PbI_2Cl_2$ single crystal, combined with DFPT first-principles calculations. The Raman spectra show the second-order features as temperature decreases. The second-order Raman generation by excitons interacting with phonons was investigated, and insights into the excitonic process were given.

Finally, Chapter 7 is dedicated to the low-dimensional photovoltaic perovskite Cs_4PbBr_6. We discuss the changes in the structure and the PL behavior of luminescent Cs_4PbBr_6 single crystals (SCs) under high-pressure conditions. A phase transition at approximately 3.0 GPa from rhombohedral to monoclinic phase was determined by high-pressure synchrotron X-ray diffraction and Raman spectroscopy. The structural phase transitions observed are similar to those found from initially non-luminescent Cs_4PbBr_6 nanocrystals (NCs)[14]. However, although the structural characteristics are similar for both systems, the pressure-induced PL response is quite different from each other. Also, adding value in the great debate about the origin of the green luminescence in Cs_4PbBr_6, our results suggest that the PL of the luminescent Cs_4PbBr_6 SCs can be associated to the different size distribution of quantum dots or NCs of $CsPbBr_3$ embedded in Cs_4PbBr_6 SCs.

2. Perovskite Structure

The Russian mineralogist Gustav Rose discovered calcium titanate ($CaTiO_3$) in 1839, which was named in honor of mineralogist Petrovski as perovskite, and materials with the same type of crystalline structure were known as perovskite compounds [3]. Therefore, perovskites are a class of compounds with a general formula close to or derived from the composition ABX_3. The ABX_3 perovskite family is formed by ionic compounds, where, usually, A is a large cation, B is a medium-sized cation, and X is an anion. The diversity of perovskite and perovskite-like layered compounds can be understood in terms of its idealized structure which is cubic (space group $Pm\bar{3}m$), as it is adopted by $SrTiO_3$ at room temperature. There are two general ways to describe this structure. The first one, depicted in Figure 1a, place A ions at the corners of the unit cell (Wyckoff position 1(a) 0, 0, 0). B ions lie at the center (Wyckoff position 1(b) 1/2, 1/2, 1/2) and form a regular octahedron with X anions (Wyckoff position 3(c) 1/2, 1/2, 0; 1/2, 0, 1/2; 0, 1/2, 1/2). The second description, which is commonly used for discussions of the chemical and physical properties of perovskites, translates the cell origin to B ions (Figure 1b). Large A ions are located at the unit cell center and are surrounded by a cuboctahedral cage of X ions. This structure is visualized as an array of corner-sharing BX_6 octahedra.

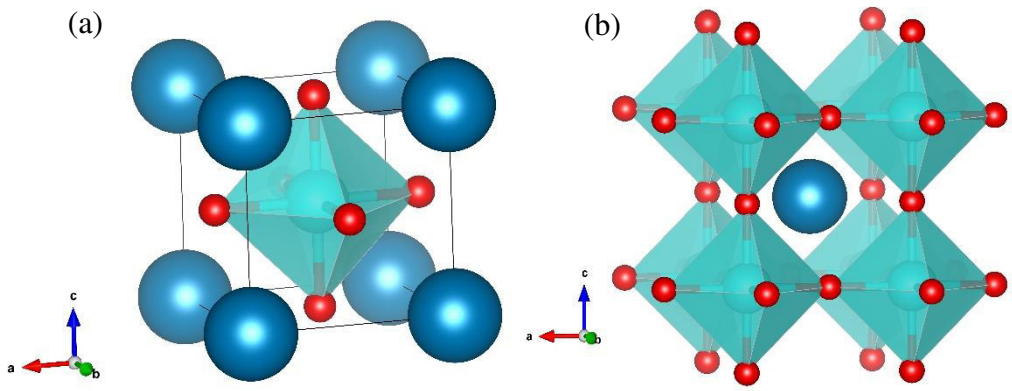

Figure 1: The ideal cubic (aristotype) perovskite of formula ABX_3 (A,B =cation, X= anion). (a) A ions (blue balls) located at the corners of the unit cell. (b) A ions located at the unit cell center. The X anions are represented by red balls.

2.1. The Goldschmidt Tolerance Factor

As aforementioned, materials with ABX_3 composition can adopt different crystalline structures depending on the size and interaction of the A cation and the corner-sharing BX_6 octahedra, from "aristotype" (more symmetric) cubic perovskite to more complex structures. Goldschmidt tolerance factor (t) is a reliable empirical index to predict which structure is preferentially formed [8]. From a crystallographic view, the ideal perovskite structure is inflexible, as the unit cell has no adjustable atomic position parameter, so that any compositional change must be accompanied by a change in the lattice parameters. In a cubic unit cell edge, lattice parameter *a* is equal to twice the B – X bond length ($2(\mathrm{B}-\mathrm{X})=\mathrm{a}$). In the same way the width of the cuboctahedral cage site, $\sqrt{2}a$, is equal to twice the $\mathrm{A}-\mathrm{X}$ bond length. Thus, the ideal structure forms when the ratio of the bond lengths is given by:

$$t = \frac{(r_A + r_X)}{\sqrt{2}(r_B + r_X)} = 1 \qquad (1)$$

where r_A is the radius of the A cation, r_B is the radius of the B cation, and r_X is the radius of the anion. In general, the ideal cubic structure is formed when the tolerance factor is in the approximate range of 0.9 – 1.0. If t > 1, that is, large A and small B, a hexagonal packing of the AX_3 layers is preferred, and hexagonal phases are formed. A tolerance factor of 0.71−0.9 results in a distorted perovskite structure with lower symmetry than cubic due to the octahedral framework distortions. There are three distortions in perovskites structures that arise from the octahedra and are responsible for the symmetry lowering: tilting or rotation of the octahedra (mostly associated with A cations that are too small for the cuboctahedral cage site), displacements of the cation B (the cations are displaced away from the center of the octahedron, leading to a tolerance factor significantly less than 1, and the structure becomes tetragonal, trigonal or orthorhombic depending of the direction and magnitude of the displacements), and the octahedral distortion (the octahedron itself can distort to give elongated or flattened octahedra) [20,21]. These distortions in geometry from ideal structure play a crucial role in tune the physical properties of the perovskites [22].

2.2. Describing The ABX_3 Structure Derivatives

The perovskites structures allow not only a wide variety of different ions in its compositions but also more chemically complex phases, which can contain mixtures of A, B,

and X ions, as well as chemical defects [3]. In many instances, these ions are randomly distributed over the available sites, but for some ratios, they can order to form phases with double, triple, or quadruple perovskite-type unit cells [23]. Thus, the perovskite family is widened by ion substitution, particularly at the A or B sites and at varying degrees [24,25]. However, particular interest is given in the case where exactly half of the B-site cations are substituted with another cation, enabling in many cases improved efficiency of the physical properties for specific applications [26,27]. In this case, the two different cations B and B', may remain disordered at the B site, or they can order, depending on whether they are sufficiently different in charge, size, and/or bonding preference of the B and B' cations. In general, when the oxidation states of B and B' differ by less than two, a disordered arrangement is observed, whereas a difference higher than two nearly always produces an ordered arrangement. When the difference in oxidation states is exactly two, disordered, partially ordered, or fully ordered arrangements can result [23]. In the next section, will be discussed some structures phases derive from the ABX_3 structure.

2.2.1. Double, Triple and Quadruple Perovskites

The most widely encountered ordered pattern is found in the double perovskites with the formula $A_2BB'X_6$ [26]. The unit cell of the double perovskites is no longer primitive ($Pm\bar{3}m$), as in simple aristotype perovskite, but gives a face-centered unit cell $Fm\bar{3}m$ [28]. The axes run parallel to the simple cubic perovskite axes, and the lattice parameters double the one of the simple cubic lattice a_p. There are three different ways in which A or B-site cations can order in the double perovskites. The most familiar ordering pattern corresponds to the two different cations arranged in a chessboard pattern, often called rock-salt ordering (Figure 2a) because the B and B' (or A and A') pattern is equivalent to the anion and cation positions in the rock-salt structure [23].

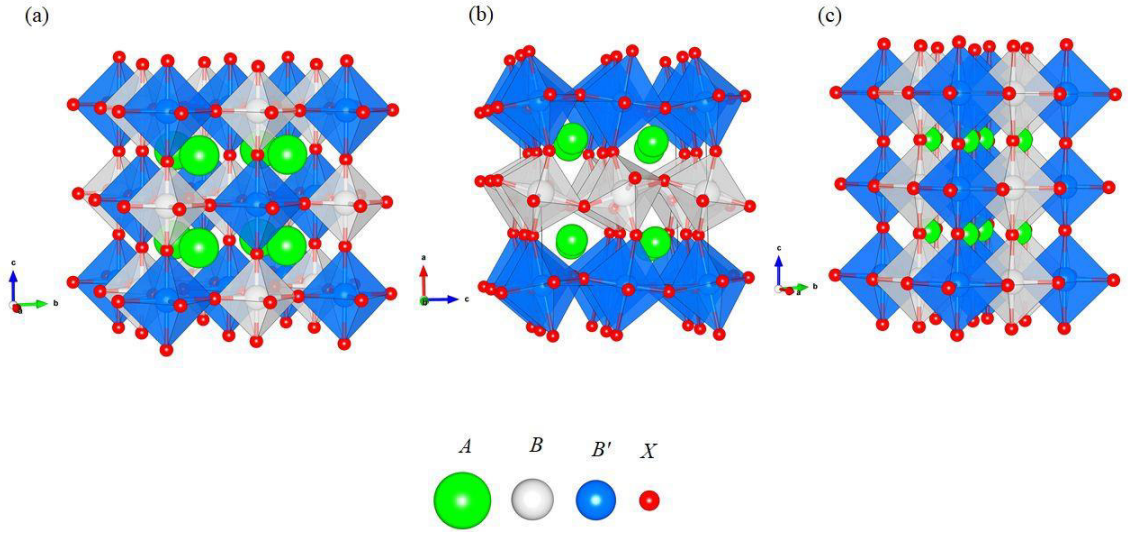

Figure 2: Different B-site cation orderings schemes found in perovskites. (a) the rock-salt ordering, (b) layered ordering, and (c) columnar ordering. The rock-salt scheme corresponds to the Ba_2MgWO_6 [28] structure with space group $Fm\bar{3}m$. The layered scheme corresponds to the La_2CuSnO_6 [29] structure with space group P4/mmm. The columnar scheme is idealized and does not correspond to a real structure.

Although not as common as the rock salt ordering, there are a few examples of columnar and layered ordering among $A_2BB'X_6$ perovskites, as shown in Figure 2(b, c) [28,29]. Cases of columnar ordering arise from charge ordering in mixed-valence perovskites (e.g., $LaCaMn^{3+}Mn^{4+}O_6$, and $NdSrMn^{3+}Mn^{4+}O_6$) [23], whereas for layered perovskites, there are only a handful of cases of layered B-site cation ordering, as the structures Ln_2CuSnO_6 (Ln = La, Pr, Nd, Sm) and La_2CuZrO_6 [23]. It is interesting to comment that considering the octahedral connectivity, the ordered double perovskites can be classified as 0D, 1D, 2D, and 3D perovskites. The rock-salt arrangement can be thought of like a 0D case, where each $B'X_6$ octahedra are isolated from each other by B cations. Similarly, columnar ordering can be considered a 1D case where the $B'X_6$ octahedra are connected in one dimension, whereas the layered perovskites can be associated with 2D structures because it allows connectivity of $B'X_6$ octahedra in two dimensions. The 3D case arises when the octahedra are corner-shared in all directions, such as happens in the simple perovskites. The classification of the perovskite structures regarding the connectivity of octahedra gained notoriety in the last five years with the halide perovskites for photovoltaic applications [30], which is discussed in more details in the next sections.

Although double perovskites with rock-salt ordering are dominant, there are other types of B-site cation ordering, such as those found in triple $A_3BB'_2X_9$ (1: 2 ordering) and quadruple

$A_4BB'_3X_{12}$ (1: 3 ordering) perovskites. As an example of the triple perovskites, we can cite the series of $Ba_3BB'_2O_9$ (B = Mg, Ni, Zn; B' = Nb, Ta) perovskites [31]. The crystal structure (Figure 3a) of these perovskites generally consists of a cubic close-packed array of BaO_3 layers wherein B and B′ atoms are ordered in the 1:2 sequence …B B′ B′ B B′ B′… resulting in a rhombohedral/hexagonal structure [31]. The perfect 1:2 ordering of B-site cations influences the dielectric properties, being 1:2 more efficient than 1:1 ordered perovskites [32]. They present excellent dielectric properties, such as high dielectric constants ($\varepsilon \approx 30$ - 40) and low dielectric loss in the microwave region, that find applications as resonators in microwave telecommunications technology [31,32]. An illustrative example of a quadruple unit cell with a stacking sequence (1:3) along the c-axis of …B B′ B′ B′… is given by the compounds $Sr_2LiSb_3O_{12}$, $Ca_2LiSb_3O_{12}$, and $Sr_2La_2CuTi_3O_{12}$ [33]. The crystal structure, which crystallizes in the tetragonal *P4/mmm* space group, is shown in Figure 3b.

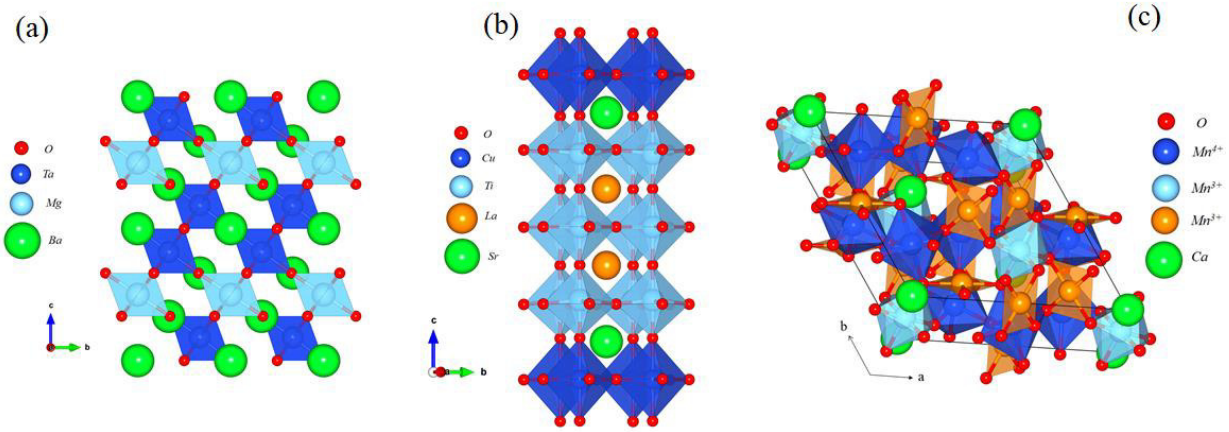

Figure 3: (a) Crystal structure of the triple perovskite $BaMgTa_2O_9$ [31]. (b) An illustrative example of a quadruple unit cell with a stacking sequence (1:3) along the c-axis of B B' B' B' (structure of $Sr_2La_2CuTi_3O_{12}$ [33]). Both the A and B-site cations are ordered. (c) A-site cation ordering of $CaMn_7O_{12}$ [34] structure with square planar coordinated sites.

In the double perovskites, A-site cation ordering is much less common than B- site cation ordering [3,23,35]. However, an example of A-site cation ordering is provided by a group of quadrupole oxide perovskites $AA'_3B_4O_{12}$ [23,36]. In this case, A can be an alkali metal, alkaline earth, lanthanoid, Pb, or Bi, and the A' cation is a 3d transition metal ion [36]. The accommodation of a 3d transition metal ion into the large cage sites is unusual because these are commonly found as high-charge medium-sized cations that prefer octahedral coordination [23,36]. So, to adopt this site, the A′ transition metal cations must show a strong Jahn–Teller effect [37]. So far, the phases synthesized have been limited to the Jahn–Teller ions Mn^{3+} and

Cu^{2+} [3]. In these, the Jahn–Teller distortion usually takes the form of an elongated octahedron or, when the deformity is extreme, a square planar configuration [3]. The perovskites with this stoichiometry show a framework of corner-linked BO_6 octahedra, together with typical A-site cations at the unit cell corner and center, and square planar coordinated sites formed from the apical and equatorial oxygen anions of the BO_6 octahedra [3,38]. $CaMn_7O_{12}$ is an example of this structure, with general molecular formula $AA'_3(B'_3B)O_{12}$, where A'/ B' = Mn^{3+} and B = Mn^{+4} [34]. $CaMn_7O_{12}$ crystallizes in the rhombohedral space group $R\bar{3}$ (See Figure 3c). This compound is studied in more detail in Chapter 5.

2.2.2. Layered Perovskites: Ruddlesden–Popper, Dion-Jacobson, and Aurivillius Phases

Due to the rising interest in photovoltaic perovskites, 2D layered compounds with perovskite-related structures have received much attention from researchers in the last years [39]. The layered perovskites are built from slabs of perovskite blocks interleaved with a second motif. The general formula of the layers is $A_{n-1}B_nX_{3n+1}$, but it is convenient to describe the structures singling out the motifs, which are the main characteristics among the layered structures. These layered compounds can be classified into three major groups: Ruddlesden-Popper, Dion-Jacobson, and Aurivillius structures. Table 1 summarizes the structural relationships between these three important series.

Table 1: Modular Perovskites. Adapted from [3].

Name	Interlayer (motif)	Layer	Perovskite slab displacement	Series formula	Examples
Ruddlesdn-Popper	A'_2	$A_{n-1}B_nO_{3n+1}$	$(\boldsymbol{a}_p + \boldsymbol{b}_p)/2$	$A_{n-1}B_nO_{3n+1}$	Sr_2TiO_4 (n=1) $Sr_3Ti_2O_4$ (n=2)
Dion-Jacobson	A'	$A_{n-1}B_nO_{3n+1}$	0 (Type I); **a**/2 (Type II) $(\boldsymbol{a}_p + \boldsymbol{b}_p)/2$; (Type III)	$A'A_{n-1}B_nO_{3n+1}$	$LiLaNb_2O_7$ (n=2) $RbCa_2Ta_3O_{10}$ (n = 3)
Aurivillius	Bi_2O_2	$A_{n-1}B_nO_{3n+1}$	$(\boldsymbol{a}_p + \boldsymbol{b}_p)/2$	(Bi_2O_2) ($A_{n-1}B_nO_{3n+1}$)	Bi_2WO_6 (n=1) $Bi_4Ti_3O_{12}$ (n=3)

Nowadays, one of the most studied 2D perovskites is the Ruddlesden–Popper phase, which is composed of two-dimensional perovskite-like slabs interleaved with cations [40,41]. The first report of a Ruddlesden–Popper phase can be traced back to the 1950s when three compounds with the K_2NiF_4-type structure were discovered by Ruddlesden and Popper, which were Sr_2TiO_4, Ca_2MnO_4, and $SrLaAlO_4$ [42,43]. The Sr_2TiO_4 (*n=1*) is described as a stacking

of single slabs of ideal $SrTiO_3$ separated by the motif, a layer of Sr_2 (see Figure 4a). Increasing the perovskite slab thickness while keeping the inter-slab structure the same, generates the phases $Sr_3Ti_2O_7$ *(n = 2)* and $Sr_4Ti_3O_{10}$ *(n = 3)*. The aristotype perovskite $SrTiO_3$ corresponds to the limit case for $n = \infty$. Each slab is displaced relative to its neighbors by (in the ideal case) a vector $(\boldsymbol{a}_p + \boldsymbol{b}_p)/2$, where $\boldsymbol{a}_p$ and $\boldsymbol{b}_p$ are the typical cubic unit cell vectors.

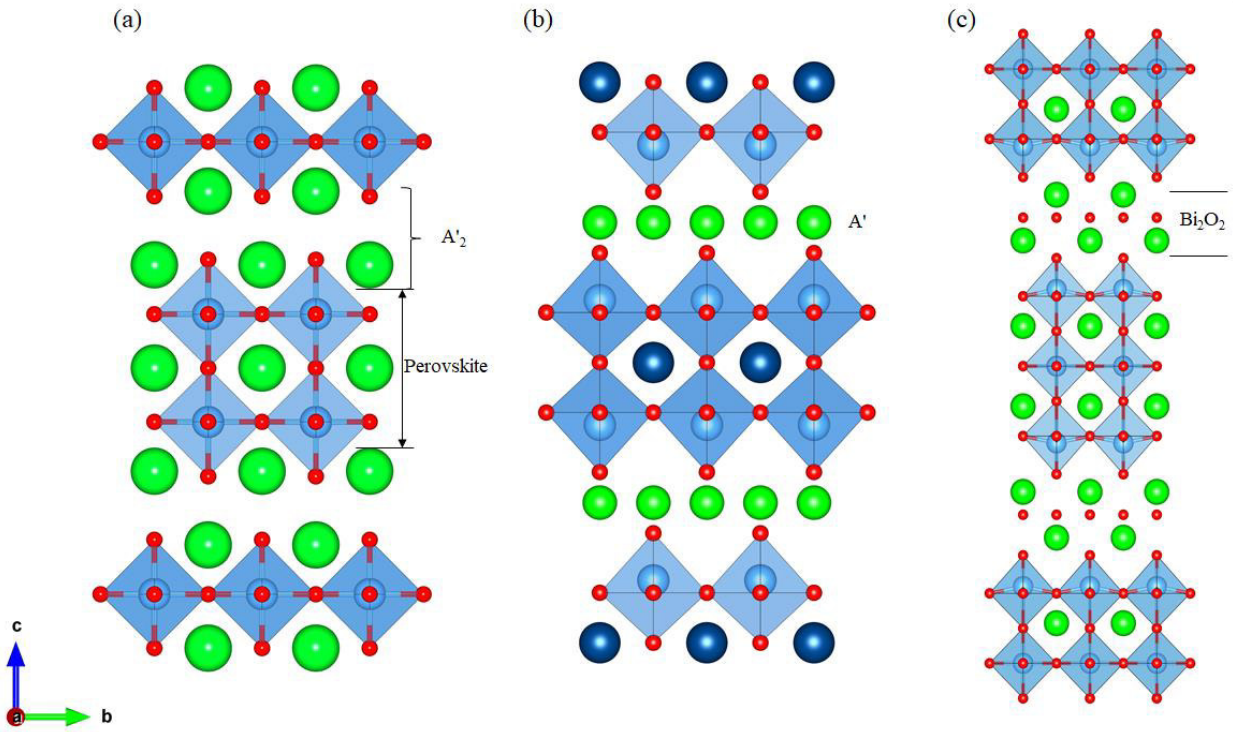

Figure 4: The idealized structures of the (a) Ruddlesden-Popper phase with n = 2 (b) Dion-Jacobson phase with n = 2, and (c) Aurivillius phase with n = 3.

If the pair of A'_2 atoms at the boundaries of the perovskite-like sheets in the Ruddlesden–Popper phases are replaced with just one A′ atom, the series takes the formula $A'(A_{n-1}B_nO_{3n+1})$, and are called Dion–Jacobson phases (Figure 4b). Three different structures accommodate the Dion–Jacobson phases. Type I structures are characterized by having no displacement between the perovskite layers, which are aligned one above the other. Type II structures have a displacement of $\mathbf{a}_p/2$ between the successive perovskite layers, that is, half a unit cell displacement either along the **a**- or **b**-axis. Type III structures have a displacement of $\boldsymbol{a}_p + \boldsymbol{b}_p)/2$ between the successive perovskite layers, which is the same as in the Ruddlesden-Popper phases. In turn, Aurivillius phases contain slabs of perovskite intercalated by a layer of Bi_2O_2. This structure is represented by a series with the general formula $(Bi_2O_2)(A_{n-1}B_nO_{3n+1})$, sometimes written in an ionic form as $(Bi_2O_2)^{2+}(A_{n-1}B_nO_{3n+1})^{2-}$ (Table 1). The displacement between adjacent

slabs is as in the Ruddlesden–Popper series. The index *n* generally runs from 1 to 5. The structure of the Bi_2O_2 layer is similar to the CaF_2 fluorite. Thus, the Ruddlesden–Popper series is also represented as an intergrowth of fluorite and perovskite elements. Bi_2WO_6 represents the *n = 1* member of the series, Bi_3TiNbO_9 the *n = 2*, $Bi_4Ti_3O_{12}$ the *n = 3*, but the best-known members of this series are the ferroelectrics $SrBi_4Ti_4O_{15}$, and $Bi_5Ti_3FeO_{15}$ in which *n = 4*. For a more in-depth discussion about perovskites, readers can check the references [3,44].

After a brief description of perovskites structures, in the next sections, some properties of multiferroic and lead halide perovskites are discussed. Relevance is given to the relationship between pressure-induced structural phase transitions and physical properties.

2.3. Phase Transitions in Multiferroic Perovskites

The increasing interest in multiferroic materials in the last few decades has been driven by their fascinating physical properties and enormous technological potential [9]. This technological potential implies in a range of applications, including data recording, memory devices, magnetic field sensors, microwave devices, and photovoltaic solar cells [45–49]. The combining and control of the simultaneous ferroic orderings are challenging, requiring engineering of new material chemistries and the development of new tools to compute and characterize the novel properties associated with the coupled behaviors [9].

As defined by Schmid in 1994, multiferroics refer to a large class of materials that simultaneously exhibit more than one of the primary ferroic ordering (ferroelectricity, ferromagnetism, ferroelasticity or ferrotoroidicity) in the same phase [12]. The terminology is often extended to include non-primary orderings such as antiferromagnetism, as well as composites of individual ferroics. These composites form heterostructures of ferroelectrics materials interlayered with magnetic materials, which is most often used today to refer specifically to magnetoelectric materials combining ferroelectric and magnetic behaviors [49,50]. Figure 5 generally describes the relationship between the ferroic orderings involved in the identification of multiferroic materials. Figure 5 indicates that when a multiferroic material is subjected to an external field (magnetic, electric, or elastic), stable tensile quantities such as magnetization (**M**), polarization (**P**), deformation (**ε**), and toroidal moments (**T**) associated with external fields appear in the material. The electric field **E**, the magnetic field **H**, and the mechanical stress **σ** control the polarization **P**, the magnetization **M**, and the elastic deformation **ε** respectively. Besides these properties, toroidal moments **T**, which should be switchable by

crossed electric and magnetic fields, have been arisen as a new ferroic ordering [9,51,52]. “O” represents other possibilities, such as spontaneous switchable orbital orderings, vortices, and chiralities, that is likely enriching future research [53].

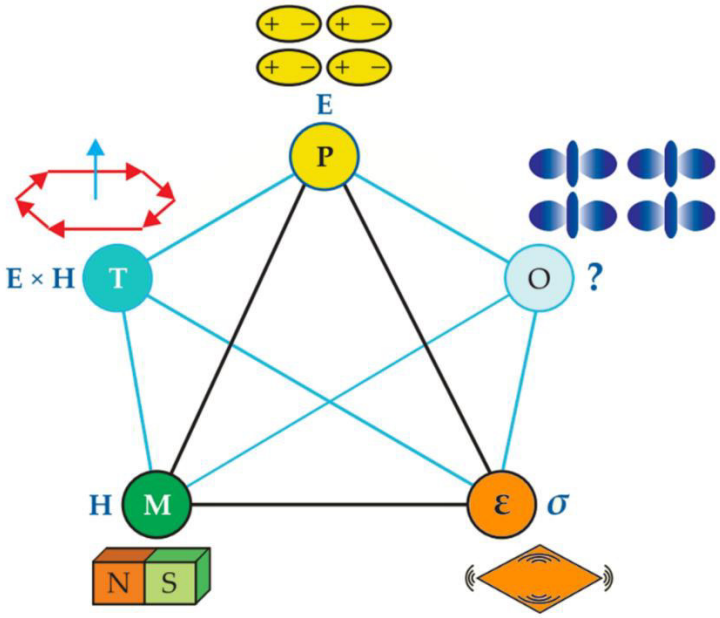

Figure 5: Diagram identifying multiferroic systems through the direct or indirect relationship between the variables involved. Figure adapted from reference [53].

Multiferroic materials become scientific and technologically impressive not only because of their capacity to exhibit several ferroic orders but also due to the possible coupling among these ordering states [9,49]. The coexistence of at least two forms of ferroic ordering leads to interactions that are considered as order parameters in the classification of couplings in multiferroic materials. These interactions are described as magnetoelectric coupling, which describes the influence of a magnetic or (electric) field on the polarization or (magnetization). Piezoelectricity and (Piezomagnetism), which describe a change in voltage as a linear function of the applied electric or (magnetic) field, or a change in polarization / (magnetization) as a linear function of applied stress. Besides, electrostriction and (magnetostriction) are described by changes in deformation as a quadratic function of the applied electric or (magnetic) field [49].

The vast majority of the most important multiferroic compounds have perovskite-related structures [49]. As we know, the octahedra blocks of the perovskite structures are its main

geometrical features and can undergo distortions by the application of external fields. Dramatic changes in the multiferroic behavior can be expected at high-pressure and high-temperature conditions once cations displacements and octahedral distortions are temperature and pressure-sensitive. So, the use of pressure and temperature provides a direct link between the atomic structure and the ferroic orders.

We can summarize the situation of multiferroicity features arising under pressure/temperature-induced phase transitions citing some important multiferroic compounds. For example, in the case of $BaTiO_3$, a pressure-induced structural phase transition from cubic to tetragonal systems induces the Ti^{4+} cations displacements. Such displacements result in a slight change in the octahedron framework giving rise to electric dipoles that are associated with the ferroelectric properties of tetragonal $BaTiO_3$ [54]. Besides the $BaTiO_3$, the $BiFeO_3$ is another multiferroic material having a perovskite structure that shows magnetic and ferroelectric behavior with an intense polarization at ambient conditions of pressure and temperature [55]. $BiFeO_3$ displays a complex response at high-pressures, with several structural phase transitions in the pressure range up to 60 GPa, but the number of phase transitions, the atomic structure, and the symmetry of the high-pressure phases remains controversial [15].

Although the perovskites are very common in the multiferroic field, the search for multiferroics materials has expanded to materials that crystallize in other structures than the perovskite-type. In this line, the $KBiFe_2O_5$ (KBFO) was proposed as a new multiferroic material with low bandgap energy ($E_g \sim 1.6$ eV) [56]. Pressure-induced structural phase transitions on the orthorhombic phase of KBFO were investigated, showing that pressure produces an enhanced in the ferroelectric, electric transport, and photoelectric properties [57]. Besides the orthorhombic phase, KBFO can crystallize in a monoclinic phase (space group P2/c) [58]. Recently, we show that the monoclinic phase of KBFO presents an unusual behavior of pressure-dependence, increasing symmetry from a monoclinic P2/c to a Pmmm structure [59]. The phase transformation was observed to be a reversible reconstructive first-order transition.

2.4. Phase transitions in Photovoltaic Perovskites

In recent years the emergence of organic-inorganic hybrid halides perovskites-like materials has generated enormous interest in the photovoltaic research community [60]. The extraordinary optoelectronic properties, low cost, and simple solution-based fabrication procedures[61–66] led these structures to the state-of-the-art photovoltaic materials. Besides

the optoelectronic features, these compounds attract notable attention due to its high efficiency for photovoltaic cell applications[67]. The groundbreaking discovery of organic-inorganic hybrid perovskite materials for converting solar energy into electrical energy has revolutionized the third-generation photovoltaic devices. In less than half a decade of rigorous research and development in perovskite solar cells, the efficiency is boosted up to 25.2% (certified PCE of PSCs), as can be found in the NREL PV chart (https://www.nrel.gov/pv/assets/pdfs/best-research-cell-efficiencies.20191106.pdf).

In general, in the perovskites photovoltaic solar cells, the *A* cation is an organic or inorganic monovalent cation like methylammonium $[CH_3NH_3]^+$ (MA), formamidinium, $[CH(NH_2)_2]^+$ (FA), and Cs^+. *B* is a divalent metal, usually Pb^{2+} or Sn^{2+}, and *X* is a halide element (F, Cl, Br, or I). The last characteristic led the perovskites solar cells to be known as "halide perovskites." It is interesting to highlight that these photovoltaic materials are associated with the "perovskite" family, but in fact, the majority of them are not actual "perovskites"; however, they are so-called for containing octahedra with the same coordination that the one in ABX_3 perovskites [68–71].

Considering the octahedra connectivity in perovskites, a simple way for understanding the components of the perovskite family for photovoltaic applications is classifying them by the spatial arrangement of the $[BX_6]^{4-}$ octahedra. In a description of this classification based on the A_nBX_{2+n} formula, structures with the empirical formula ABX_3 are referred as 3D perovskite ($n=1$), consisting of a framework of corner-sharing metal halide octahedra (Figure 6a) that extends in all three dimensions, with small organic or inorganic cations fitting into the void spaces between the octahedra (Figure 6b). For $n = 2 – 4$, the structure is often referred to as low-dimensional perovskites. 2D and quasi-2D perovskites structures ($n = 2$) with the layered structure, organized from octahedra connected along the octahedral axes, can be derived from 3D by slicing along specific crystallographic planes (Figure 6d). In the case of quasi-2D perovskites, the formation occurs through the superposition of two or more categories; for instance, a superstructure of 3D and 2D (Figure 6c). If 2D perovskites are further sliced perpendicular to the inorganic sheets, octahedra remain connected only along one axis, which can be categorized as 1D perovskites ($n = 3$) (Figure 6e). The extreme case is 0D perovskites ($n = 0$), derived by further slicing of 1D, to form nonconnected (i.e., isolated) octahedra or octahedra-based clusters (Figure 6f).

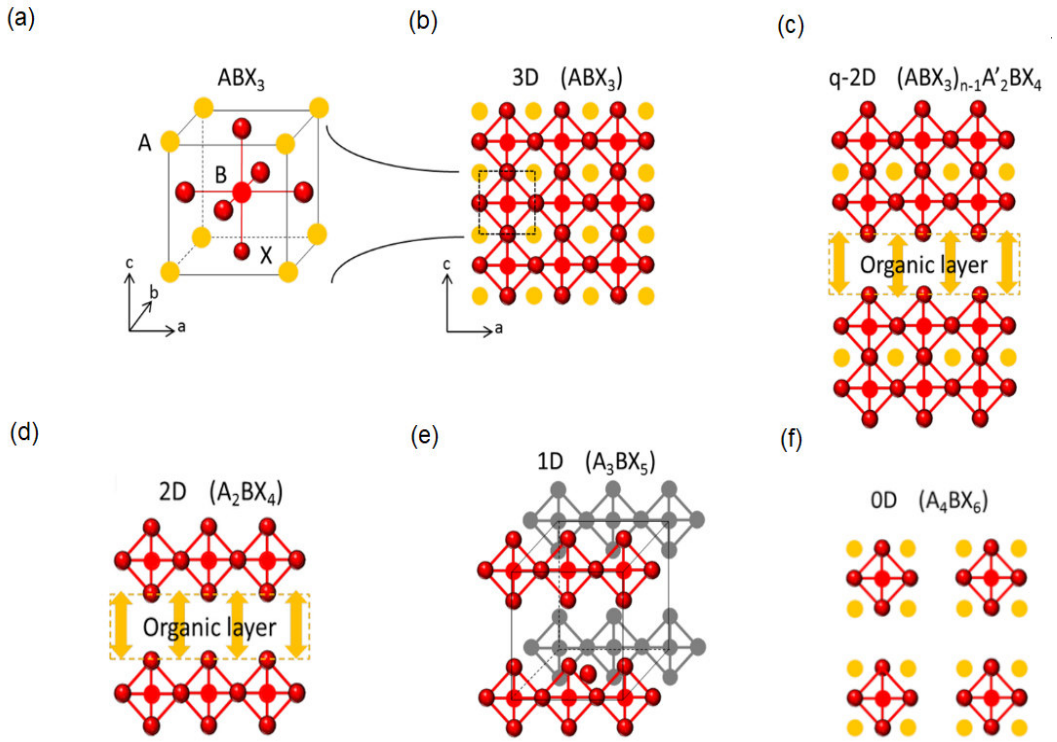

Figure 6: Typical structures of 3D, 2D, 1D, and 0D perovskites. Figure adapted from Ref. [37].

The 3D organic-inorganic and all-inorganic $APbX_3$ (A = Cs, Methylammonium (MA), and Formamidinium (FA); X = Br, Cl, and I) perovskites were the first ones to have their optical properties exhaustively investigated in the last five years [69,72–75]. Those structures have demonstrated a tunable PL emission spectra from ultraviolet (UV) to the near-infrared by tuning their bandgap [76]. Many researchers have attempted to tune the bandgap of perovskites controlling their chemical composition [77] and crystallite size [73]. Progress has been made in changing the halides ions, for example, the bandgap energies of $MAPbX_3$ (X: Cl, Br, or I) change from 3.11 eV → 2.35 eV → 1.55 eV when X is changed from Cl → Br → I [78]. Protesescu *et al.*[72] reported that the bandgap energies of all-inorganic cesium lead halide perovskites $CsPbX_3$ nanocrystals (NCs) could be tuned over the entire visible spectral region by adjusting their composition. Figure 7 shows that the PL spectra can be tuned from 410 to 700 nm with a narrow emission full width at half maximum (FWHM) of 12−42 nm. The PL center emission is 410 nm for $CsPbCl_3$, 525 nm for $CsPbBr_3$, and 700 nm for $CsPbI_3$.

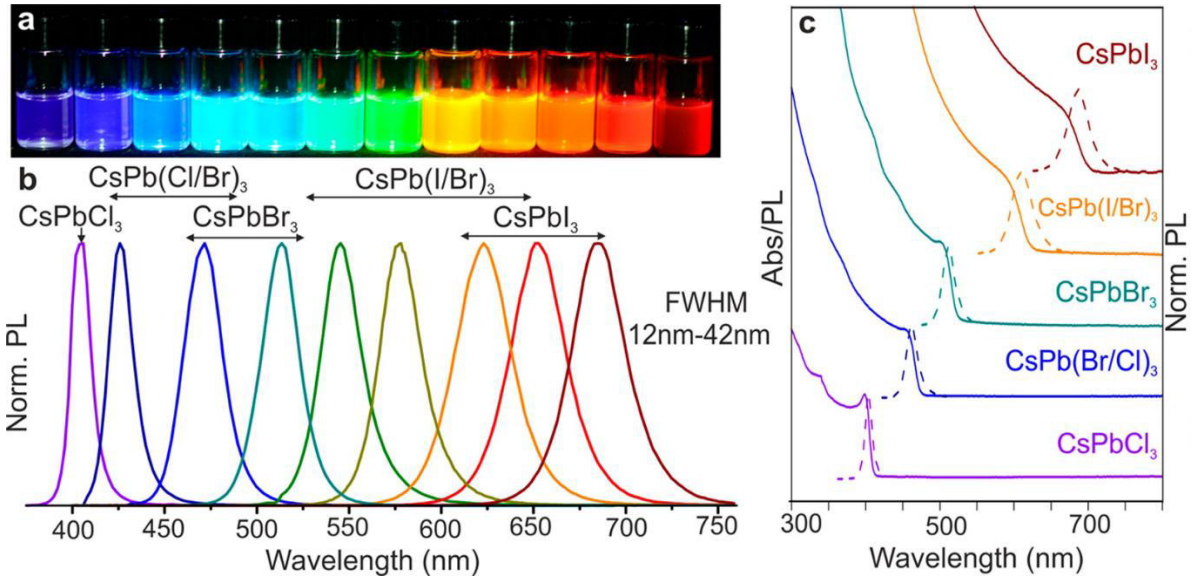

Figure 7: Colloidal perovskite $CsPbX_3$ NCs (X = Cl, Br, I) exhibit size and composition-tunable bandgap energies covering the entire visible spectral region. (a) colloidal solutions under UV lamp, (b) representative PL spectra, (c) typical optical absorption and PL spectra. Figure adapted from Ref. [72].

High-pressure experiments have proven to be a valuable technique to tune the crystal structure and physical properties in perovskites structures. Several investigations were conducted to understand if high-pressure influences the photovoltaic properties of the lead halide perovskites. The 3D perovskites $MAPbX_3$ (X= Br, Cl, and I) [16,79,80] and $CsPbX_3$ (X= Br, Cl, and I) were investigated under high-pressures conditions, as well as low dimensional structures like $Cs_3Bi_2I_9$ [81], Cs_4PbBr_6 [14], Cs_2PbBr5 [17], and $(PEA)_2PbBr_4$[18]. In the next paragraphs, we summarize the effect of pressure on some of these structures.

Zhao *et al.* reported the phase transitions of $MAPbBr_3$ under high pressures conditions of up to 34 GPa [79]. Two pressure-induced structural phase transitions below 2 GPa were observed. Summarizing, the cubic $Pm\bar{3}m$ structure transformed to another cubic structure $Im\bar{3}$ at 0.4 GPa doubling the unit-cell, then to an orthorhombic Pnma structure around 1.8 GPa. The amorphization process starts at above 2 GPa, and almost all of the diffraction peaks disappeared at 12.5 GPa. The phase transitions observed are attributed to the tilting of $PbBr_6$ octahedra and the loosing of the long-range ordering of MA cations, respectively. Upon decompression, the amorphous phase was reversible, exhibiting a memory effect. The sequence of phase transitions is shown in Figure 8a. The photoluminesce emission (PL) of $MAPbBr_3$ at ambient conditions of pressure and temperature exhibits a green emission centered at 525 nm. To accompanied the pressure effect on the photovoltaic related properties, Zhao *et al.* [79] carried out pressure-

dependent PL measurements. With a further increase in pressure, the PL peaks became weaker and finally undetectable due to the enhanced non-radiative processes in the amorphous structure (see Figure 8b). The bandgap, as a function of pressure derived from PL spectra and band structure calculations, were also investigated. The bandgap shows a redshift below 1 GPa, followed by an anomalous blueshift at higher pressures (when compared with first-principles predictions) (Figure 8c). Similar effects under pressure were observed for $MAPbCl_3$ [16], and $MAPbI_3$ [82,83] with structural phase transitions points occurring close to those of $MAPbBr_3$. The pressure-dependence of PL and bandgap demonstrated to follow the same pattern observed in organic-lead bromide perovskites with a redshift in phase I and a subsequent blueshift in phase II. Figure 8(d – i) shows the pressure-dependent lattice parameters, PL spectra, absorbance, and bandgap for $MAPbCl_3$ and $MAPbI_3$.

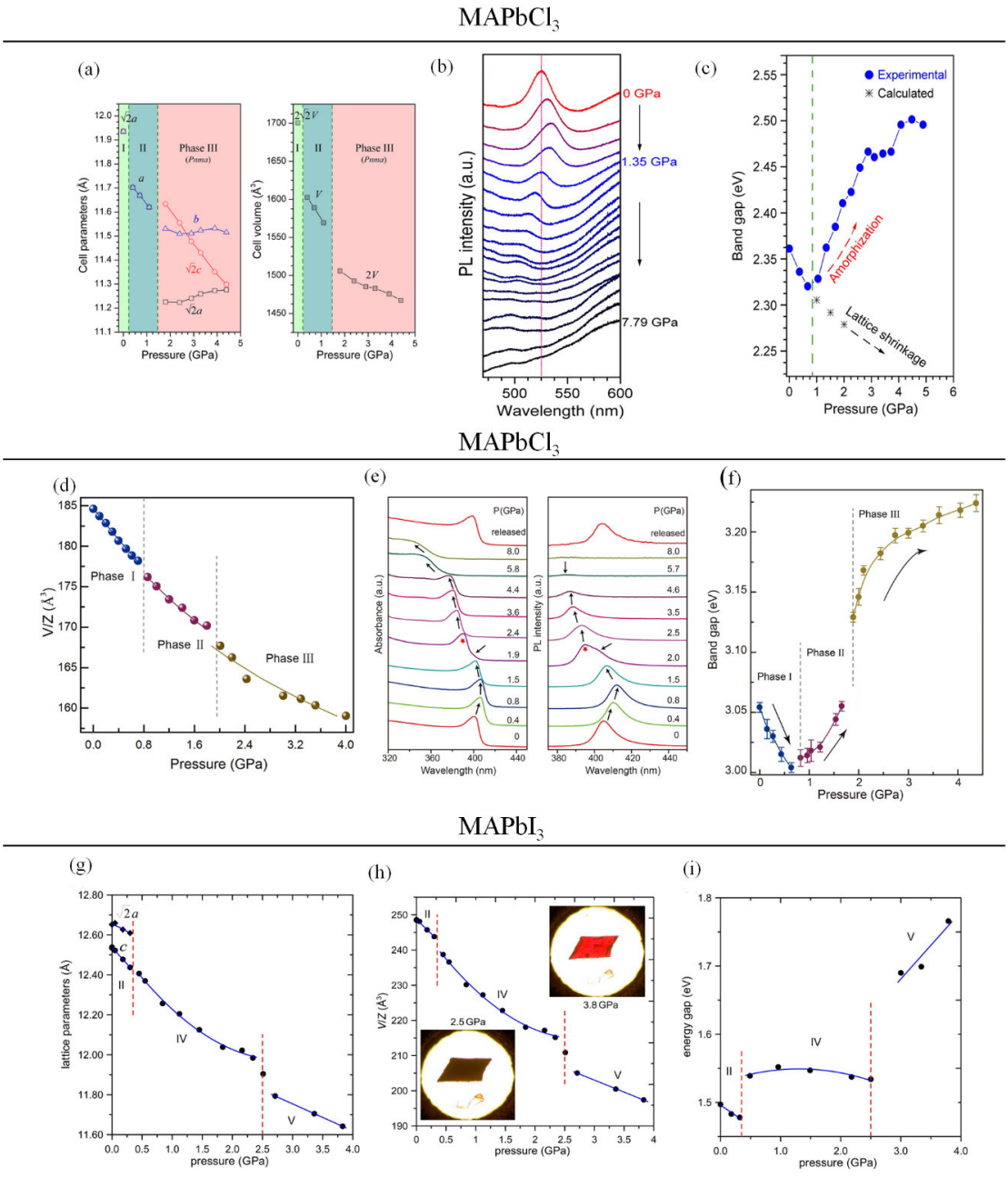

Figure 8: Lattice parameters, PL spectra, and bandgaps at several pressures of (a-c) $MAPbBr_3$. (d-f) $MAPbCl_3$, (g-i) $MAPbI_3$. Figure adapted from Refs [16,79,82].

The 3D all-inorganic halide perovskites investigated under high-pressure conditions demonstrated to have slightly higher structural stability compared to organic-inorganic hybrid perovskites. They present one phase transition instead of two, with the PL and bandgap, following the same behavior as hybrid perovskites with a redshift before phase transition and a blueshift upon the phase transition [84–86]. The pressure-dependence PL spectra, absorbance, and bandgap for $CsPbBr_3$ and $CsPbCl_3$ are shown in Figure 9. The results show that hydrostatic pressure can alter the lattice and electronic of halide perovskites and their photovoltaic related properties.

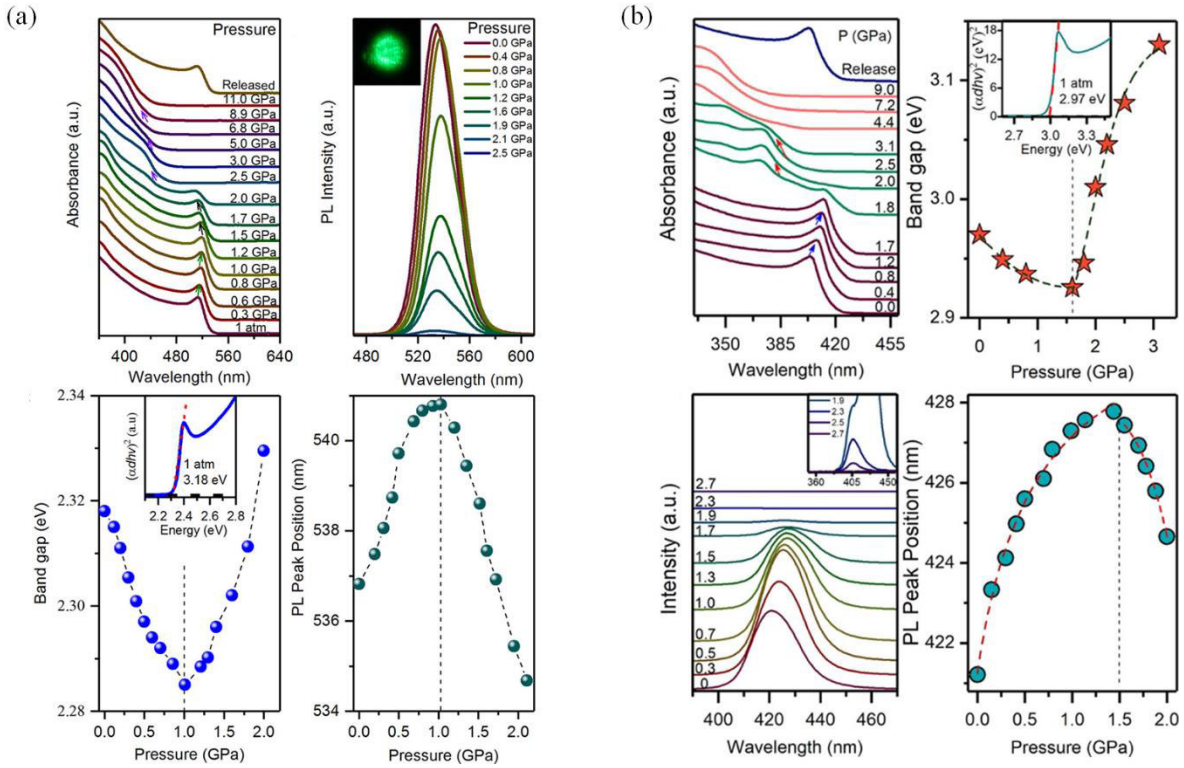

Figure 9: (a) Absorption spectra, PL spectra, bandgap evolution, and PL peak position as a function of pressure for $CsPbBr_3$. (b) Absorption spectra, PL spectra, bandgap evolution, and PL peak position as a function of pressure for $CsPbCl_3$. Figure adapted from Refs [84,85].

2.5. Stability and Toxicity of Lead Halide Perovskites

Despite the success of the lead halide perovskite-based devices in enhancing the efficiency of photovoltaic solar cells and their low fabrication cost, these devices still face several critical challenges that impair practical applications for new technology. Stability and toxicity of Pb stand as formidable obstacles for the commercialization of photovoltaic solar cells [87,88]. In the context of toxicity, there has been growing research interest in developing alternative lead-free perovskites with low toxicity and high stability [89,90]. Considering the photovoltaic properties, and based on ionic size and Goldschmidt tolerance factor, a wide range of cations are predicted to be replacements for Pb. Some elements lead-free perovskites are tin (Sn), germanium (Ge), antimony (Sb), and bismuth (Bi) [60]. They are proposed as potential candidates to address the lead toxicity, but the resulting devices yielded lower power conversion efficiency (PCE) values than those reported with lead halide perovskites [91].

Although organic−inorganic hybrid perovskites like MAPbI3, FAPbI3, and the mixed-cation-based perovskites (FA/MA, MA/Cs, FA/Cs, FA/MA/Cs, etc.) are leading in terms of efficiency, they have been facing a considerable challenge to provide long-term stability. The instability of lead halide perovskites to moisture, light, and heat is another issue that must be addressed [92,93]. To overcome this issue, numerous efforts have been made to enhance the stability of the device [93–95]. One of these efforts is the replacement of organic cation with an inorganic cation. One of inorganic cation that has been found suitable and successful in forming perovskite structures is cesium (Cs^+), although studies also predict some perovskite compounds of Rb [96]. However, the efficiency of these all-inorganic structures is inferior compared to organic−inorganic hybrid perovskites [93]. 2D perovskites are more stable to heat and humidity, but they lag behind the 3D perovskites in terms of performance because of their narrow absorption band in addition to poor electron transport properties [97]. A new strategy that has succeeded in improving intrinsic stability or, essentially, the moisture stability of perovskites is by mixing the 2D structures with 3D structures [98]. The mixing of a small amount of 2D perovskite with 3D perovskite structures has been found to provide higher efficiency and improved long-term stability [93].

3. Experimental Setup

In this chapter, we describe the experimental apparatus used in this thesis. We start discussing the high-pressure/high-temperature Raman spectroscopy and photoluminesce setups and after, the synchrotron X-ray diffraction one. Details of the synthesis of the investigated samples are given in the experimental section of each chapter.

3.1. Raman Spectroscopy

Raman spectroscopy is a non-destructive technique widely used to investigate the vibrational properties of solids, being highly sensitive to variations in local symmetry, changes in the chemical bonds, exciton-phonon coupling, variations in the magnetic structure such as spin modulations and ordering orbital. So, it is an important technique for detecting phase transitions or subtler structural rearrangements under extreme conditions of pressure and temperature.

High-pressure Raman spectroscopy measurements on the Cs_4PbBr_6 sample were performed at the Federal University of Ceara using a Labram HR 800 Horiba spectrometer equipped with a charge-coupled device (CCD) cooled with liquid nitrogen (Figure 10a). For exciting the Raman signal, a He-Ne (633 nm) laser was employed. The spectrometer slits were set for a resolution of 2 cm^{-1}. The high-pressure conditions were achieved using a diamond anvil cell (DAC) with mineral oil nujol as pressure-transmitting media for hydrostatic conditions. Small ruby chips were introduced in a metallic gasket together with the sample to determine the pressure values by measuring its luminescence emission (Figure 10c).

High-pressure Raman measurements on the multiferroic ceramic $Bi_5Ti_3FeO_{15}$ (BFTO) and the low-temperature Raman measurements on the $Cs_2PbI_2Cl_2$ sample were performed at the Federal University of Ceara using a Jobin-Yvon T64000 Triple Spectrometers (see Figure 10b) configured in a backscattering geometry coupled to an Olympus Microscope model BX41 with a 20x long-working distance achromatic objective for BFTO and a 50x objective for $Cs_2PbI_2Cl_2$. The 532 nm line laser was used to excite the Raman signal for BFTO. In both samples, the spectrometer slits were set up to achieve a spectral resolution of 2 cm^{-1}. For $Cs_2PbI_2Cl_2$, a 514.5 nm line laser emission was used to excite the Raman signal and a 401 nm

laser for PL measurements. The pressure measurements for BFTO followed the same setup already described above. Temperature-dependent Raman measurements for $Cs_2PbI_2Cl_2$ from 16 up to 300 K were carried out by using a closed-cycle He cryostat in which the temperature was controlled by a Lakeshore temperature controller model 330 with a precision of 0.1 K.

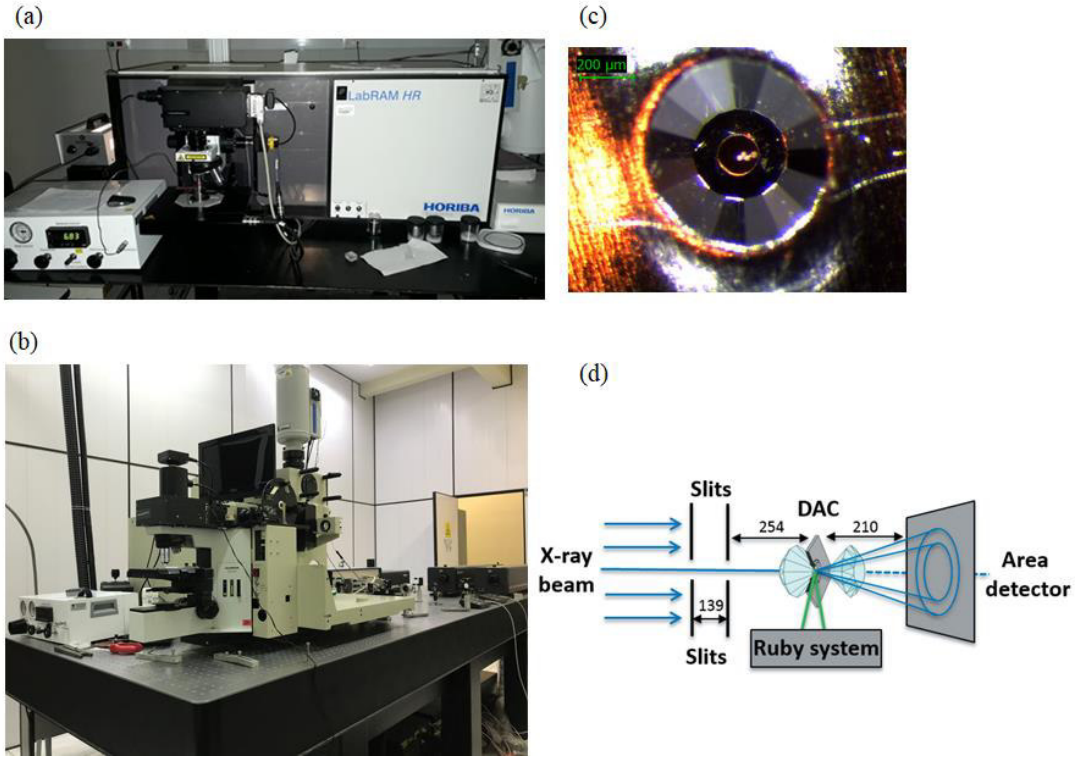

Figure 10: (a) Labram HR 800 Horiba spectrometer; (b) Jobin-Yvon T64000 Triple Spectrometers; (c) Visualization of sample chamber with samples and Ruby.;(d)Schematic drawing of the setup for SXRD experiments under high pressure at the XDS beamline (Figure adapted from Ref. [99]).

3.2. Synchrotron X-ray Diffraction

Synchrotron light is a much more intense source of X-ray radiation than laboratory ones. The synchrotron light (which can be X-rays, ultraviolet, visible, and infrared light) is produced when charged particles, electrons, or protons, traveling at speeds close to the light are deflected by powerful magnetic fields in an accelerator of electrons. As in sealed X-ray tubes, electrons are produced by a heated tungsten filament and then are accelerated in the direction of the booster (first ring in Figure 11b) using a linear accelerator (LINAC). In the booster, the electrons undergo further acceleration until reach high energies. They are then injected into the so-called storage ring (second ring in Figure 11b), and the scattered radiation is collected in several beamlines [100,101].

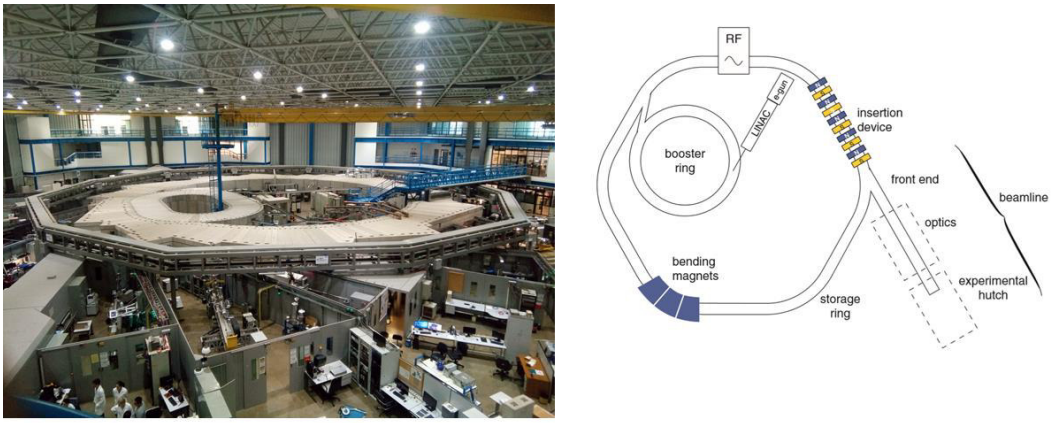

Figure 11: (a) Image of UVX, a second-generation synchrotron light source designed and built-in Brazil, located at the Brazilian Synchrotron Light Laboratory (LNLS), Campinas, SP, Brazil. (b) A schematic of the most important components of a synchrotron source. Figure adapted from [100].

For all samples investigated under pressure conditions Cs_4PbBr_6, $Bi_5Ti_3FeO_{15}$, and $CaMn_7O_{12}$, the structural stability under hydrostatic pressure was investigated by synchrotron X-ray powder diffraction (SXRPD) at the XDS beamline of the Brazilian Synchrotron Laboratory (LNLS). This beamline employs a 4 T superconducting multipolar wiggler (SCW) as a photon source and operates in the energy range between 5 and 30 keV. Summarizing, the beamline optical configuration consists of a collimating mirror (VCM) with bender, a double-crystal monochromator (DCM) with interchangeable sets of crystals, and a focusing mirror (VFM) with a bending mechanism, permitting focus adjustments. More details about this beamline can be found in Ref. [99]. All measurements were performed at room temperature with $\lambda = 0.61999$ for Cs_4PbBr_6 Å, $\lambda = 0.623036$ Å for $Bi_5Ti_3FeO_{15}$, and $\lambda = 0.602495$ Å for $CaMn_7O_{12}$. To apply high-pressure, a diamond anvil cell (DAC) (see Figure 10d) with Ne gas as pressure-transmitting media for hydrostatic conditions was used in the multiferroic samples. For Cs_4PbBr_6, the oil nujol was used as a pressure transmitting media. Once that we intended to achieve lower pressures for Cs_4PbBr_6. Coupled to synchrotron facility, a Raman spectrometer was used for the photoluminescence measurements, using a 405 nm solid-state laser. Small ruby chips were introduced in a metallic gasket together with the sample to determine the pressure values by measuring its luminescence emission. In this configuration, the X-rays are transmitted through the diamonds and sample and collected in an area detector MarCCD MX225 (Rayonix, LLC). Figure 10d illustrates the setup for SXRPD experiments under high pressure at the XDS beamline. The two-dimensional powder patterns were integrated using the software FIT2D [102].

4. Pressure-Induced Structural Phase Transitions in the Multiferroic Four-Layers Aurivillius Ceramic $Bi_5FeTi_3O_{15}$

In this chapter, we present a pressure-dependent study of $Bi_5FeTi_3O_{15}$ through synchrotron X-ray powder diffraction (SXRPD) and Raman spectroscopy to monitor its structural behavior up to 15 GPa. Our results show that BTFO undergoes two pressure-induced structural phase transitions in the investigated range. A detailed analysis of the Raman spectra and SXRPD patterns also suggest the existence of a third transition.

4.1. Introduction

Multiferroic materials, which simultaneously exhibit more than one coupled primary ferroic order (ferromagnetism, ferroelectricity, ferroelasticity, or ferrotoroidicity) in the same phase, have been intensively studied over the past decade due to their fascinating physical properties and the enormous potential for technological applications [45,48,49,103]. In recent years, Aurivillius compounds with the general formula $(Bi_2O_2)^{2+}(A_{n-1}B_nO_{3n+1})^{2-}$ were also subject to intense research because of their high-temperature ferroelectric properties. [104,105] Among the Aurivillius family, $Bi_5FeTi_3O_{15}$ (BFTO), which have a structure consisting of four-layers of perovskite units of $(Bi_3FeTi_3O_{13})^{2-}$ intercalated between two $(Bi_2O_2)^{2+}$ layers along the c-axis [106,107], is a promising compound to show magnetoelectric effect [108,109], and interesting electric and optical properties such as, dielectric/ferroelectric transition at high temperatures [106,110], micro-piezoelectric coefficient of $\sim$ 35.28 pm/V [111], narrow bandgap of $\sim$ 2.39 eV [112], and photovoltaic properties with large photocurrent J_{sc} $\sim$ 10μA/cm^2 and a smaller photovoltage $V_{oc} \sim$ 0.14 V [113,114]. BFTO is usually described as a combination of a ferroelectric ($Bi_4Ti_3O_{12}$), and a long-range magnetic ($BiFeO_3$) ordered phases, having atoms with a half-filled *d*-shell (Fe^{+3}) and lone-pair of electrons (Bi^{+3}). Considering these structural characteristics, BFTO is a potential candidate to present multiferroic properties, but the low Néel temperature and the weak magnetoelectric coupling limit its applications. However, several authors reported the enhancement of multiferroicity by doping BFTO with other magnetic atoms [112,115,116].

The sequence of temperature-induced phase transitions on Aurivillius compounds exhibit different ferroic features depending on the number of perovskite layers. Usually, odd-layered compounds display a single structural transition, while many even-layered compounds exhibit two phase transitions [117–119]. The expected phase transition sequence of even-layered Aurivillius compounds starts with a ferroelectric orthorhombic phase ($A2_1am$) transforming into a paraelectric orthorhombic one, whose space group depends on the number of layers. The last transition leads the compound to the archetypal paraelectric tetragonal phase ($I4/mmm$). Kubel and Schmid suggested that BFTO (n=4) undergoes the typical two-step transition (at 833 K and 1023 K) from a ferroelectric-orthorhombic to a paraelectric-tetragonal phase, with an intermediate paraelectric-orthorhombic structure [107,120]. However, high-temperature neutron powder diffraction studies show that BFTO exhibits a single-step structural phase transition, from the ferroelectric-orthorhombic phase directly into the paraelectric-tetragonal one ($A2_1am \rightarrow I4/mmm$) [118,121]. A similar result was obtained in $ABi_4Ti_4O_{15}$ (A = Ca, Sr, Ba, Pb) compounds [122], which also transform in one step into the archetypal phase. Thus, if four-layers Aurivillius compounds exhibit a continuous transformation from the ferroelectric orthorhombic to the paraelectric tetragonal phase, and intermediary paraelectric orthorhombic phase is necessary, but, in this case, the temperature range of stability of the later phase should be narrow.

Despite the fact that there is a large number of studies in layered Aurivillius compounds, the structural stability under hydrostatic-pressure has been scarcely investigated. Raman scattering measurements have been employed to observe structural phase transitions under hydrostatic pressure conditions in some cation-deficient Aurivillius phases (Bi_2MoO_6 [123], Bi_2WO_6 [124], $Bi_2W_2O_9$ [125]), and they have shown to provide very useful information on the origin of lattice instabilities in this family of compounds [126]. Also, high-pressure synchrotron X-ray diffraction has been reported only for the one-layer cation deficient Bi_2MoO_6 compound [127]. These investigations showed Aurivillius compounds generally undergo two-phase transitions under pressure around 3 and 7 GPa.

4.2. Experimental

The synthesis of BFTO was take in collaboration with the Group of Chemistry of Advanced Materials (GQMat) coordinated by professor Pierre Fechine. In this synthesis, a conventional solid-state reaction route was used. Analytically pure Bi_2O_3 (Aldrich, 99.9 %),

Fe_2O_3 (Aldrich, 99 %) and TiO_2 (Dynamic, 99.9%) were weighed carefully and mixed thoroughly in stoichiometric proportions. The mixtures were ball milled in a planetary Fritsch Pulverisette mill 6 at 370 rpm for 1 h in stainless steel vials and balls at room temperature with a weight ratio 1:10. After that, the mixed powder was heated (heating rate of 5 ºC/min) until 900ºC, where it was calcined for 1 h. Then, the calcined powder was manually homogenized with 5 wt. % of polyvinyl alcohol, which was used as a binder to reduce the sample brittleness. Finally, this mixture was pressed into small pellets and sintered at the same thermal conditions applied during the calcination step.

Room-pressure purity and crystalline structure of the samples were determined by X-ray Powder Diffraction (XRPD) measurements using Cu-K_α (λ = 1.5405 Å) radiation on X'PertPro MPD-Panalytical diffractometer operating at 40kV under a current of 30 mA. XRPD data were collected with a step of 0.02º between 10º and 90º. A Rietveld profile analysis was performed using the software X'Pert High Score Plus and DBWS (see Figure 12). The analysis confirmed that BFTO crystallizes in an orthorhombic structure belonging to the *A2₁am* space group in accordance with the previous studies [121].

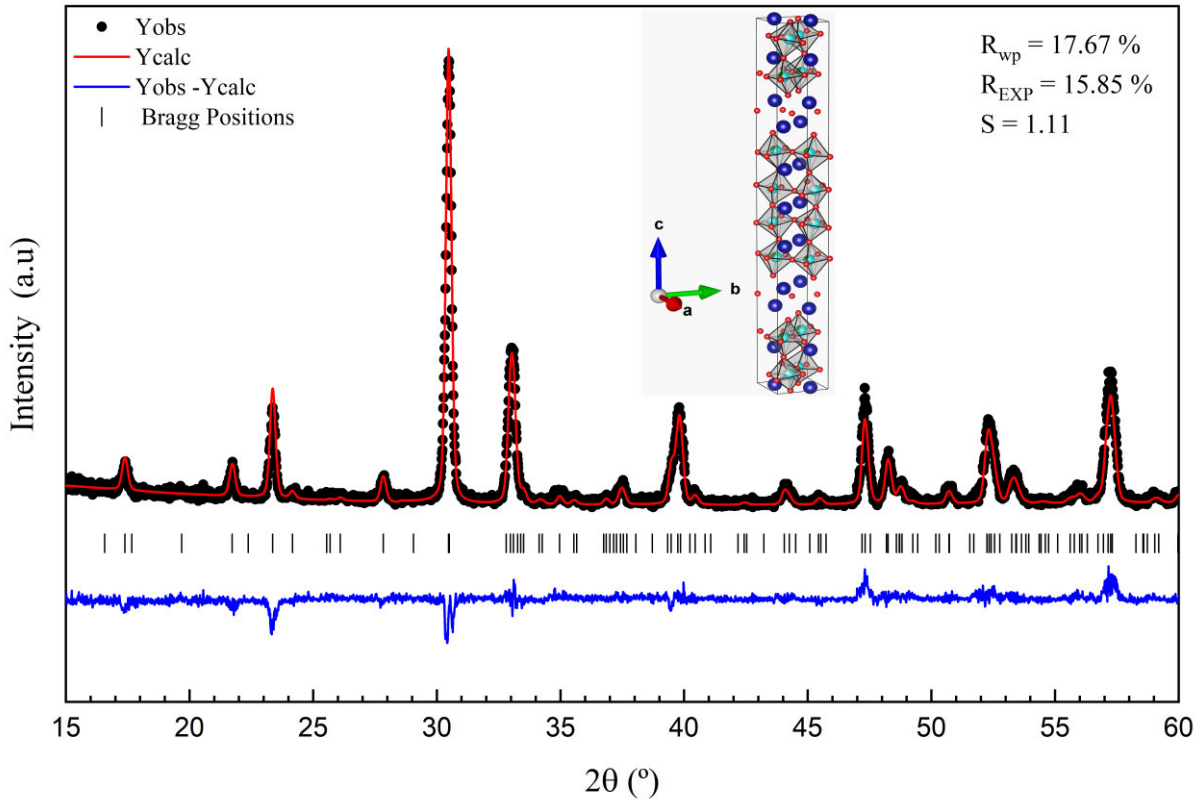

Figure 12: X-ray powder diffraction Rietveld analyses of the BFTO.

4.3. Results and Discussion

Like other members of the four-layers Aurivillius family, BFTO crystallizes in an orthorhombic lattice at room temperature, being the $A2_1am$ the most common space group. Considering those with titanium at the B site, a relevant difference lies in the site occupation as $ABi_4Ti_4O_{15}$ have partially disordered A cations in the Bi_2O_2-layers [122], whereas in BFTO, iron substitute randomly titanium at the center of the oxygen octahedra[117]. In any case, the structure of ambient conditions derives from the tetragonal archetypal one by the tilting and distortion of the $(Ti/Fe)O_6$ octahedra combined with the displacement of the A cation along the polar axis. The low-symmetry lattice parameters are along the diagonals of the tetragonal cell base, having a dimension of $\sim\sqrt{2}\,a_T$ and doubling the number of molecules per unit cell ($Z_T = 2 \rightarrow Z_O = 4$).

Figure 13a presents the BFTO powder patterns recorded at pressures up to 13.68 GPa. By direct inspection of these results, no clear evidence of structural phase transitions was noticed. However, there is a consistent shift in the peak position towards higher angles, which suggests a pressure-induced volume reduction. The low-pressure patterns were successfully indexed with an orthorhombic structure, but due to the limited angular range imposed by the diamond anvil cell, it was not possible to perform a complete structural resolution. Instead, the Le Bail method, implemented in the FullProf package [128], was applied to determine the pressure dependence of the lattice parameters using a pseudo-Voigt function as a peak profile.

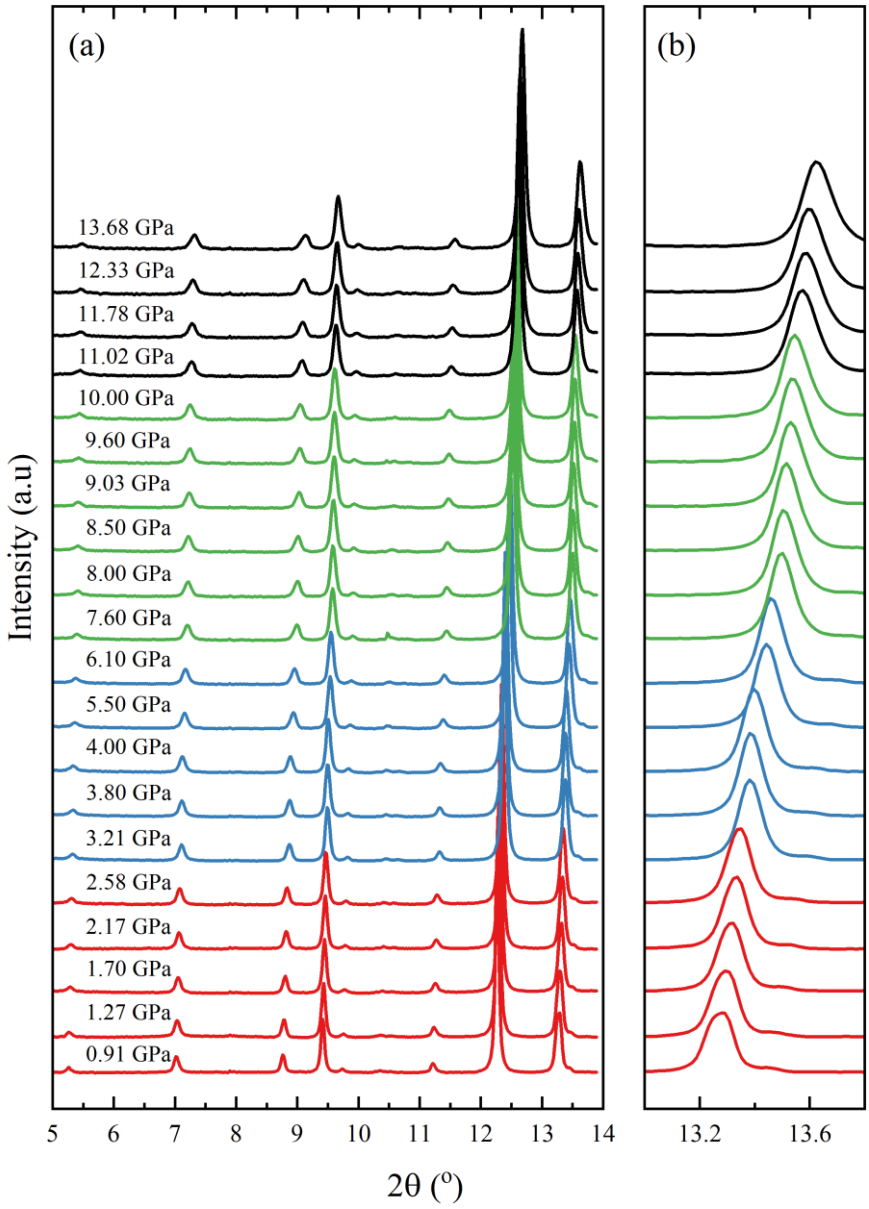

Figure 13: Synchrotron X-ray diffraction patterns of BFTO at different pressures.

Figure 13 shows the pressure dependence of the lattice parameters, which were kept as independent fitting variables. Increasing the pressure, a and b decrease following the expected volume lowering, but it is interesting to notice that above 3 GPa, these parameters converge to the same value within the uncertainty, suggesting an orthorhombic (OL) to tetragonal (TI) structural phase transition. This effect is evidenced by the (020)OL and (200)OL peaks observed around 13.27o in the orthorhombic phase, which becomes a single peak (200)TI above 3 GPa, as it is shown in Figure 13b. To test this hypothesis, two tetragonal phases were used in new refinements. The apparent first proposal was the archetypal tetragonal body-centered lattice with $a_{OL} \cong \sqrt{2}a_{TI}$, but this structure did not provide reliable results. Instead, stable

values were obtained with a primitive lattice with $a_{OL} \cong a_{TI}$. The lattice parameters in the stability region of the tetragonal phase are included in Figure 14. Above 7.5 GPa, the crystal lattice can no longer be described as tetragonal, and a new phase transition transforms BFTO into an orthorhombic structure different from the one at ambient conditions. This transition is marked by a significant split between a and b, but just a small slope change in the c dependence on the applied pressure was observed. Thus, none of the described transitions seems to change the lattice periodicity along the [001] direction, suggesting that the driven mechanism should be related to an orthorhombic distortion in the ab plane. Finally, around 10.5 GPa, a subtle change in the behavior of b suggests the existence of a new event, which is evidenced by a discontinuity in the pressure dependence of the W parameter of the Caglioti's relationship for the FWHM peak profile. Notice that this parameter also exhibits a discontinuity around 3 GPa showing sensitivity to the structural phase transitions. However, this evidence is not enough to confirm the existence of a new phase above 10.5 GPa. Summarizing, SXRPD experiments suggest the following sequence of phase transition for BFTO:

$$\underset{\mathrm{A2_1am}}{Orthorhombic} \xrightarrow{3.2\ GPa} Tetragonal \xrightarrow{7.5\ GPa} Orthorhombic \xrightarrow{10.5\ GPa} New\ phase$$

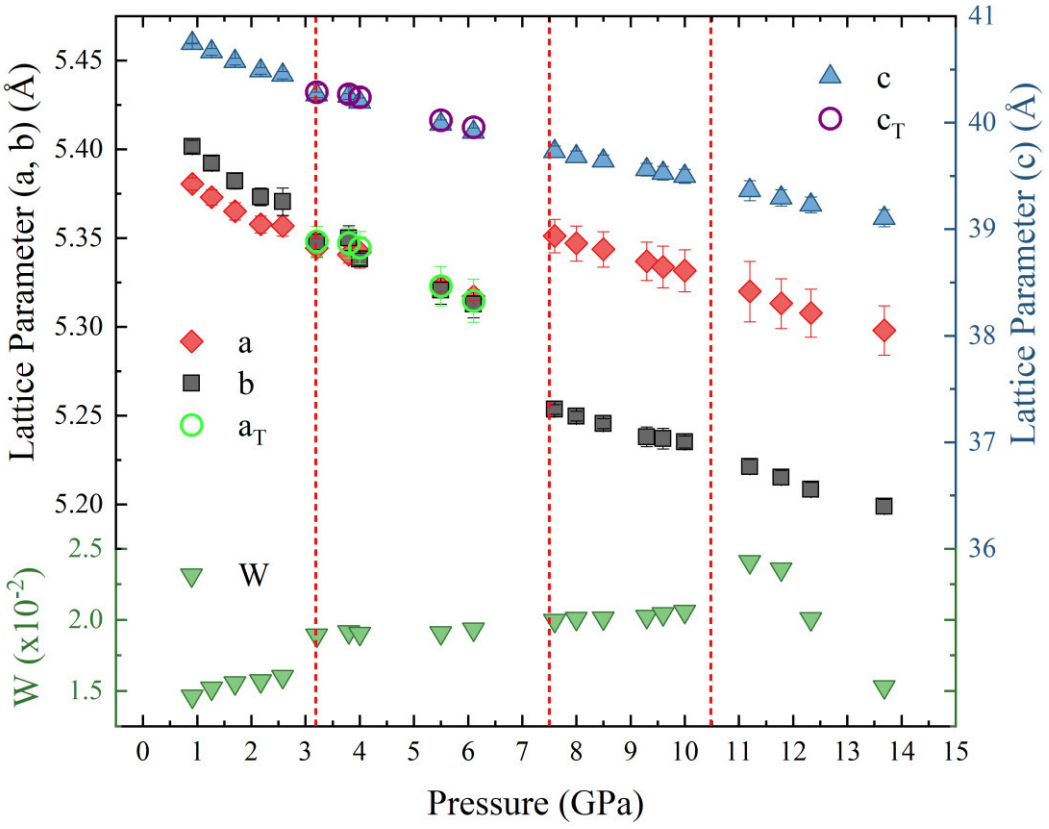

Figure 14: Pressure dependence of the orthorhombic lattice parameters (a,b,c) and FWHM (W) of $Bi_5FeTi_3O_{15}$. a_T and c_T are the results of the refinement with a tetragonal structure. Red dashed lines indicate the proposed structural phase transitions.

Raman spectroscopy is a reliable technique to detect structural phase transitions since it is highly dependent on local symmetries, mainly in compounds where the structural phase transitions are due to small atomic displacements, as it is usual in perovskites and Aurivillius phases. Thus, Raman spectroscopy measurements under hydrostatic-pressure were employed to corroborate the SXPRD results.

Figure 15 shows the pressure-dependence Raman spectra of the BFTO from ambient pressure up to 15.2 GPa. The ambient pressure Raman spectrum was modeled using 19 Lorentzian bands. Furthermore, Table 2 lists the Wyckoff sites and their contribution to the Raman active irreducible representations of orthorhombic ($A2_1am$, C_{2v}^{12}) and archetypal tetragonal Aurivillius phase ($I4/mmm$, D_{4h}^{17}). Since there is a group-subgroup relationship between these structures, the site symmetry reduction was easily calculated with the help of the tools available in the Bilbao Crystallographic Server [129], showing the Wyckoff sites correlation between these phases.

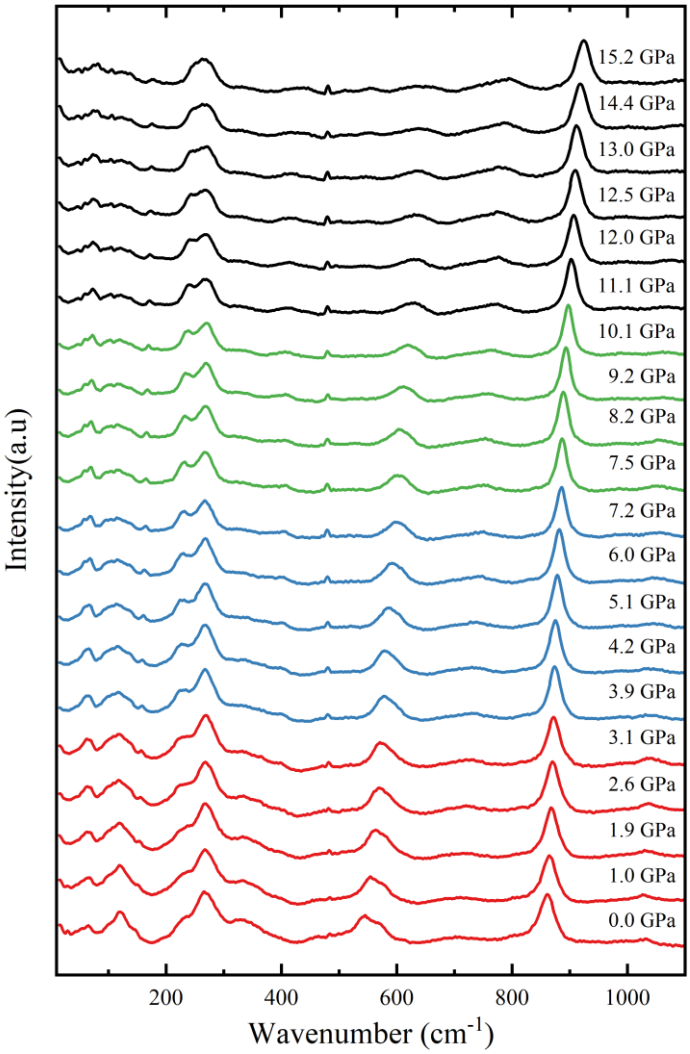

Figure 15: Pressure dependence of the Raman spectra of $Bi_5FeTi_3O_{15}$. The colors represent the structural phase transitions proposed by SXRPD.

The first inspection of the group theory results evidences a significant difference between the predicted (141) and observed (19) number of modes. The discrepancy can be attributed to the very low distortion of the orthorhombic structure compared to the tetragonal one. As discussed before, the orthorhombic phase of BFTO derives from the ideal archetypal four-layer member of the Aurivillius series by the tilting of the $(Ti/Fe)O_6$ octahedra and the displacement of the Fe/Ti cations in the perovskite layers, which leads to the loss of the inversion center.[117] As a non-centrosymmetric lattice, active infrared modes from 2a and 2b sites of the tetragonal structure become Raman active in the orthorhombic phase, but the corresponding Raman activity could be expected to be low due to the small orthorhombic distortion. Another effect that needs to be considered is the increase of the molecules per unit cell, which, combined with the symmetry lowering, increases the number of Raman active

modes originated by each lattice site. Considering these facts, it is not surprising that the number of observed modes resembles the one from the tetragonal phase (22) since the orthorhombic distortion could not be enough to clearly split the new modes, giving rise to broad bands [130]. The proposed model is also supported by Raman spectra recorded as a function of temperature by Jian et al. [120], showing that, as temperature decreases, the main bands are preserved, but split, at the phase transition between the paraelectric and ferroelectric to orthorhombic phases.

The Raman spectrum of compounds with layered Aurivillius structure is usually discussed in terms of the low and high-wavenumber modes, which are observed, respectively, below and above 200 cm^{-1} [131–133]. The low-wavenumber modes are classified as external modes and related to large atomic masses. Thus, the modes observed below 70 cm^{-1} originate in rigid displacements of the Bi^{3+} atoms in the Bi_2O_2 layers (Figure 15). The modes associated with the A cations in the pseudo-perovskite slabs are in the range between 100 and 150 cm^{-1}. The $(Ti/Fe)O_6$ octahedra internal vibrations occur above 200 cm^{-1} since the intragroup binding energy within this octahedra is much larger than the intergroup or crystal binding energy [24]. Three distinct groups of bands are associated with bending (~265 cm^{-1}), bending/stretching combinations (~350 cm^{-1}), and stretching (~550 cm^{-1}) of the TiO_6 octahedra [120,132,134]. Vibrational bands around 700 cm^{-1} have not been observed in bismuth layered oxides with titanium-based octahedra, such as $Bi_4Ti_3O_{12}$, $SrBi_4Ti_4O_{15}$, $CaBi_4Ti_4O_{15}$, $PbBi_4Ti_4O_{15}$ [132], but they are present in structures containing iron, e.g., $LaBi_4FeTi_3O_{15}$, $YBi_4FeTi_3O_{15}$ and $LaFeO_3$[135]. Thus, this band can be attributed to the stretching of the FeO_6 octahedron. The presence of these octahedra also leads to the band splitting into the other internal mode regions. A mode around 860 cm^{-1} is commonly observed in the Bi-layered Aurivillius structures but not in simple perovskites containing the same oxygen octahedra. However, there are some controversies in the assignment of this band since some authors related it to the A-O stretching due to its dependence on the A cation substitution [132], whereas most of the reports include it among the oxygen octahedra internal modes [133,136–138]. Finally, weak bands around ~1000 cm^{-1}, which are not always reported, could be associated with overtones and/or combinations of fundamental vibrational modes.

Table 2: Raman active modes and site symmetry in the archetypal tetragonal and ambient conditions orthorhombic phases of BFTO.

Atom	$I4/mmm$	$\Gamma^{R}_{D_{4h}}$	$A2_1am$	$\Gamma^{R}_{C_{2v}}$
Bi	2a		4a	$2A_1 \oplus A_2 \oplus B_1 \oplus 2B_2$
2x Bi	4e	$A_{1g} \oplus E_g$	8b	$3A_1 \oplus 3A_2 \oplus 3B_1 \oplus 3B_2$
2xTi/Fe	4e	$A_{1g} \oplus E_g$	8b	$3A_1 \oplus 3A_2 \oplus 3B_1 \oplus 3B_2$
O	2b		4a	$2A_1 \oplus A_2 \oplus B_1 \oplus 2B_2$
O	4d	$B_{1g} \oplus E_g$	8b	$3A_1 \oplus 3A_2 \oplus 3B_1 \oplus 3B_2$
2x O	4e	$A_{1g} \oplus E_g$	8b	$3A_1 \oplus 3A_2 \oplus 3B_1 \oplus 3B_2$
2x O	8g	$A_{1g} \oplus B_{1g} \oplus 2E_g$	2x 8b	$3A_1 \oplus 3A_2 \oplus 3B_1 \oplus 3B_2$
Total		$8A_{1g} \oplus 3B_{1g} \oplus 11E_g$		$36A_1 \oplus 35A_2 \oplus 34B_1 \oplus 36B_2$

The evolution of the phonon modes under increasing hydrostatic pressure is shown in Figure 16, where dashed vertical lines indicate the proposed phase transitions. The deconvolution of the Raman spectra at selected pressures is shown in Figure 17, where arrows indicate the vibrational bands fingerprinting the phase transitions. Before discussing in detail these results, it is essential to point out that the pressure dependence of the vibrational modes of BFTO is fully reversible. Many spectra were recorded releasing the pressure, being processed using the same methodology without showing significate differences with the data presented in Figure 16. Due to that, for simplicity, the results obtained releasing the pressure were not included in this figure.

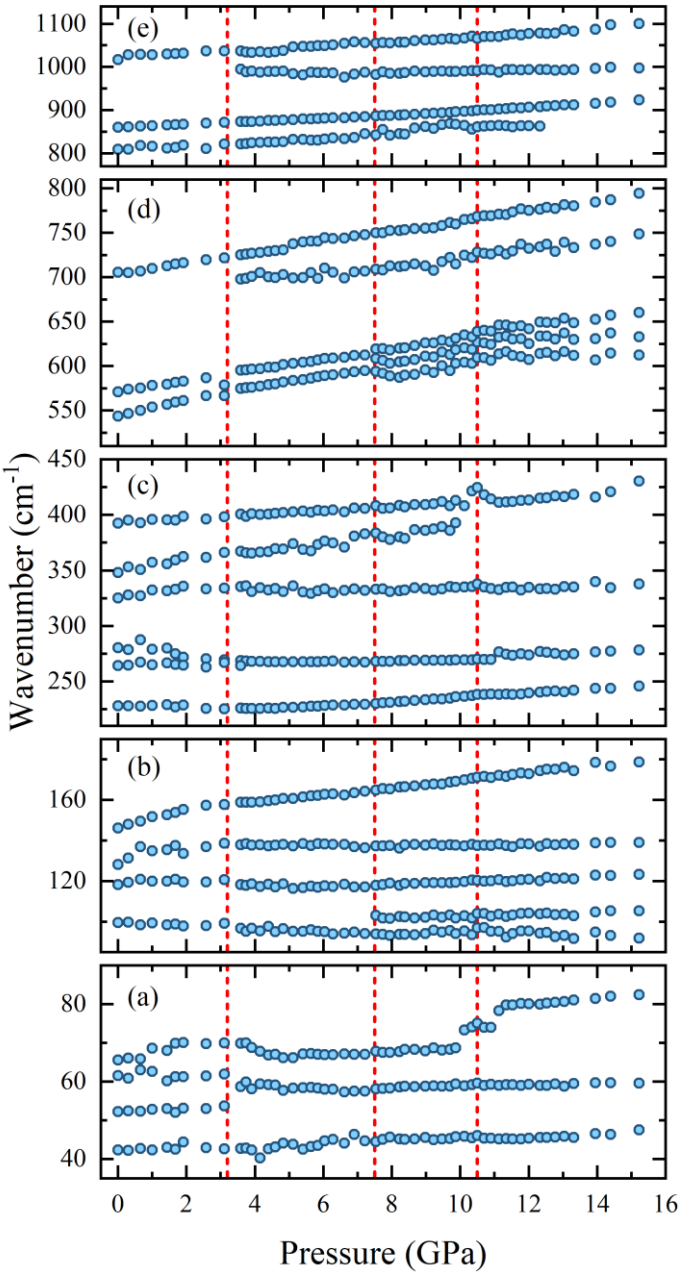

Figure 16: Pressure dependence of the energy of the Raman-active modes of $Bi_5FeTi_3O_{15}$. Red dashed lines indicate the proposed structural phase transitions.

The first structural phase transition is evidenced in all the previously described spectral regions. Thus, the Bi_2O_2-layer external modes at 52 and 61 cm^{-1} [23] and the octahedra bending modes at 265 and 280 cm^{-1} merge into single modes above 3.2 GPa. Furthermore, the raising of new bands (697 and 995 cm^{-1}) and slope changes (65, 146, 228, and 543 cm^{-1}) are also noticed at the same pressure. As stated, the unconstrained Le Bail fit suggests a tetragonal structure due to the overlap of the a and b lattice parameter. From the group theory point of view, degenerated irreducible representations are characteristic of tetragonal space groups.

Thus, in any orthorhombic-tetragonal phase transition, it is expected that two unidimensional representations should merge into a degenerated one, for example, in the case listed in Table 2: $B_1 \oplus B_2 \rightarrow E_g$. In our results, this effect was observed in both external and internal modes under hydrostatic pressure, several authors were reported similar signatures of an orthorhombic-tetragonal at high temperatures, where Aurivillius structures transform into the archetypal phase [138,139]. These features not only confirm the structural phase transition observed in SXRPD measurements but also provide information about the symmetry changes.

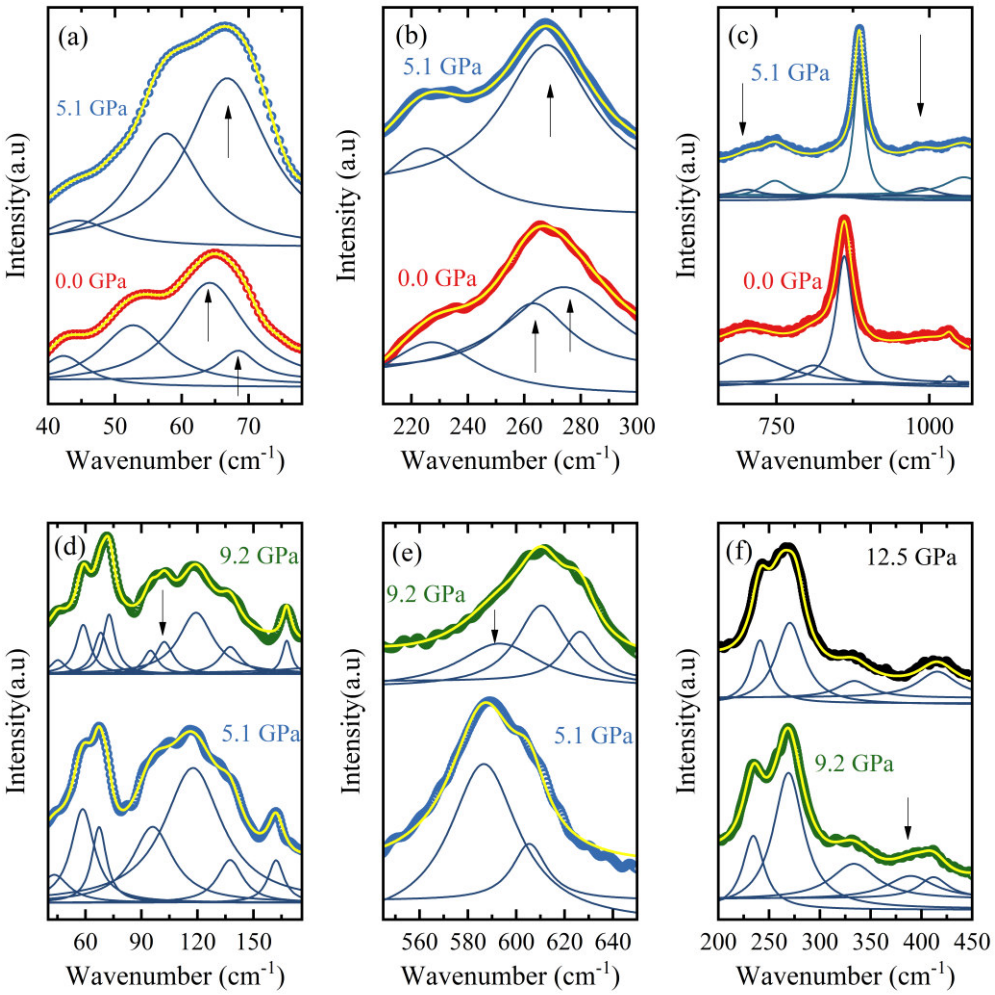

Figure 17: Deconvolution of Raman spectra at selected pressures. Arrows indicate changes in the vibrational modes.

The high-pressure transition around 10.5 GPa is fingerprinted by the oxygen octahedra internal modes through the vanishing of a mixed bending/stretching mode of the octahedra around 390 cm^{-1} and a small discontinuity in the bending around 270 cm^{-1}. A larger anomaly is also observed in the Bi_2O_2-layer external mode (~75 cm^{-1}). Even considering these results,

the nature of the third event cannot be depicted entirely. It could be argued that the high-pressure phase is related to an amorphization process, but this phenomenon is usually continuous, and sudden changes are observed in the parameters of the Raman spectra and powder patterns. Furthermore, an amorphization should broaden the SXRPD peaks, but the Le Bail fit shows the Caglioti's parameter lowers above 10.5 GPa. No amorphization effects were noticed in other Aurivillius structures under pressure, being all the observed transitions reversible [126]. The closer member to BFTO investigated at high-pressures, $Bi_4Ti_3O_{12}$, also exhibit structural phase transitions at 3 and 11 GPa[140]. Thus, the combined results of the Raman and SXRPD experiments support the existence of a new crystalline phase above 10.5 GPa, but its symmetry remains unknown.

Spontaneous lattice distortions are one of the most significant physical effects that accompanies a structural phase transition when symmetry lowers. They can be described adequately through the spontaneous strain tensor [141]. In these cases, the spontaneous strain might induce the phase transition or could be coupled with another driving mechanism. Therefore, we investigated the pressure dependence of the spontaneous strain, which was calculated based on the observed lattice parameters, to get insights about the nature of the structural phase transition of BFTO. Here, the non-zero components of the spontaneous strain, calculated based on tetragonal-orthorhombic change, are defined as: $e_1 = (a - a_0)/a_0$, $e_2 = (b - a_0)/a_0$, and $e_3 = (c - c_0)/c_0$, where a, b and c are the lattice parameters of the orthorhombic phase and a_0 and c_0 are the lattice parameters of the tetragonal phase extrapolated into the stability field of the orthorhombic phase [142]. The pressure dependence of the square of the spontaneous strain is shown in Figure 18. Based on Landau free energy expansion, for an orthorhombic-tetragonal phase transition, a linear coupling in the form of $Q^2 \propto P$ is predicted for a second-order phase transition, where Q is the driving order parameter [141,143]. The adapted symmetry-breaking strain $e_1 - e_2 = (a - b)/a_0$ has a linear dependence with Q and, usually, it has been used as an order parameter to describe proper-ferroelastic phase transitions[143–146]. The square of the symmetry-breaking strain as a function of pressure shows that $e_1 - e_2$ is zero in the tetragonal phase, whereas over the entire pressure interval of the first orthorhombic phase is proportional to Q. The best fit of the $(e_1 - e_2)^2$ data present a linear behavior with increase of pressure, which is consistent with the character of a second-order proper ferroelastic phase transition [141,143]. The linear extrapolation of the order parameter to zero strain gives a transition pressure point of 3.8 Gpa in good agreement with both SXRPD and Raman analysis, and leaving at 3.21 GPa below

within the stability field of the tetragonal phase [147]. Similar results of second-order phase transitions induced by temperature were already reported for BFTO and for other compounds of the Aurivillius family [107,121,148,149]. Finally, the inset in Figure 18 shows a discontinuity in the order parameter for pressures higher than 7.5 GPa. This discontinuity in the order parameter strongly suggests a first-order phase transition [150] from a tetragonal to a new orthorhombic phase. The strain values remain constant up to the limit of the investigated pressure range, not evidencing the third phase transition.

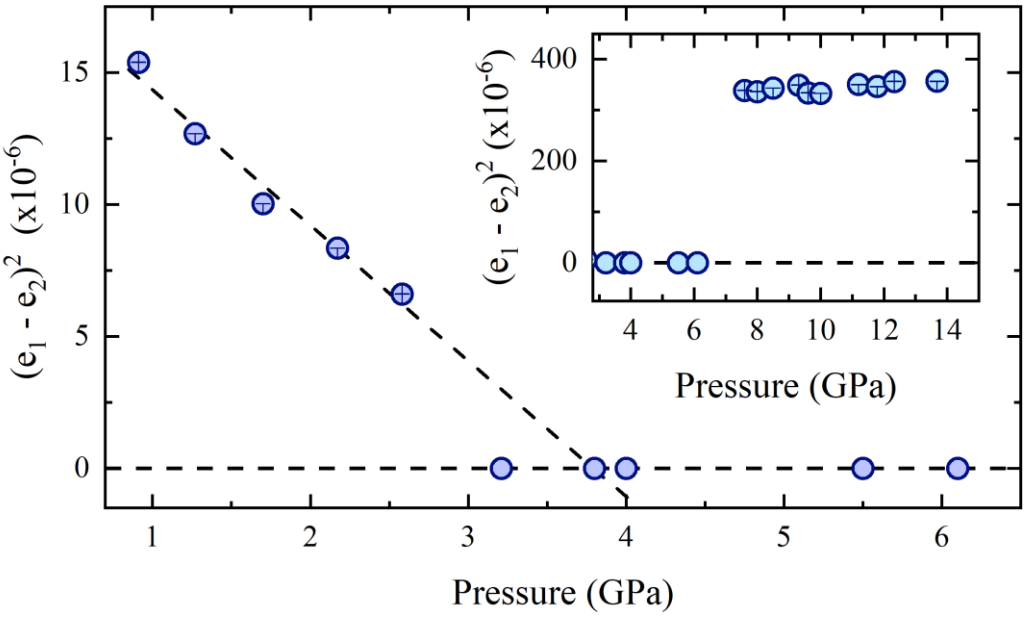

Figure 18: Square of the symmetry-breaking strain as a function of pressure. The dashed line represents the best fit curve of the data below to the transition point.

4.4. Conclusions

In summary, the effect of high-pressure on the crystalline structure of the multiferroic ceramic $Bi_5Ti_3FeO_{15}$ was investigated. Combining the results from synchrotron x-ray powder diffraction and Raman spectroscopy, three structural phase transitions were identified. Around 3.2 GPa, BFTO undergoes an orthorhombic-tetragonal transformation, which exhibits a second-order character based on the analysis of the symmetry-breaking strain. Above 7.5 GPa, a phase transition from tetragonal to a new orthorhombic phase is observed. The discontinuity in the strain suggests this transformation the evidence of a first-order phase transition. Also, subtle changes in the Caglioti's function parameters and Raman spectra above 10.5 GPa indicate the onset of another phase, whose symmetry was still unknown.

5. Pressure-Induced Structural Phase Transition on the Multiferroic Ceramic $CaMn_7O_{12}$

In this chapter, we investigate the $CaMn_7O_{12}$ (CMO) compound, which has recently emerged as a unique multiferroic material exhibiting large induced electric polarization. CMO crystallizes in a rhombohedral structure at room temperature and undergoes a structural phase transition (SPT) at high temperatures. In this chapter, we show that CMO exhibits at least two SPT induced by hydrostatic pressure. CMO transforms into a monoclinic structure around 9.9 GPa and undergoes a shear of monoclinic phase for pressures higher than 13.3 GPa. For pressures above 17.0 GPa subtle changes in the lattice parameters are observed, suggesting a new phase transformation of CMO.

5.1. Introduction

A-site-ordered quadruple perovskites (AMn_7O_{12}) have been attracting a lot of attention since $CaMn_7O_{12}$ (CMO) has emerged as a singular multiferroic material exhibiting the largest recorded magnetically-induced electric polarization [151–154]. The origin of the electric polarization in this compound is due to two effects contributing equally: the exchange striction interaction, which determines the polarization magnitude, and the Dzyaloshinskii-Moriya (DM) interaction, driving the polarization direction [154–156]. This model is also applied to explain the magnetically-induced ferroelectricity in other quadruple perovskites, such as $SrMn_7O_{12}$, $PbMn_7O_{12,}$ and $CdMn_7O_{12}$ [157]. However, Tereda *et al.* suggested, based on the pyroelectric and bias electric field measurement, that such a high electric polarization in quadruple perovskites is not intrinsic but due to thermally stimulated currents (TSC) [158]. Also, no ferroelectric transitions were observed in RMn_7O_{12} with R = Sm, Eu, Gd, and Tb quadruple perovskites [159]. At low temperatures, CMO undergoes an unusual phase transition, exhibiting an unconventional incommensurate orbital ordering at 250 K. Such orbital ordering stabilizes the CMO chiral magnetic structure [151,156,160,161]. Two antiferromagnetic (AFM) transitions were recorded at T_{N1} = 90 K, where ferroelectricity appears, and T_{N2} = 45 K, associated with multiple propagation vectors [162–164], but no additional structural phase transitions were observed below 250 K.

Despite the thorough discussion on the CMO ferroelectric and magnetic properties [151,154–156,158], few investigations were focused on the structural phase transitions (SPT) undergone by this compound. At high temperatures, CMO crystallizes in a cubic structure belonging to the $Im\bar{3}$ space group. Around 440 K, it undergoes a simultaneous charge-ordering and SPT transforming into a rhombohedral structure with $R\bar{3}$ symmetry [165–168]. In fact, there is a cubic-rhombohedral phase coexistence temperature range down to 400 K.

Recently, a high-pressure investigation showed that the isostructural quadruple perovskite $NaMn_7O_{12}$ exhibits an insulator-to-semimetal transition around 18 GPa. Such transition is due to Mn charge transfer, which leads to a metallic behavior [164], but high pressure does not affect the $NaMn_7O_{12}$ crystalline structure. Regarding CMO, there are neither reports on pressure-induced SPTs nor on changes in its electronic properties. However, the effect of the Sr-substitution on CMO, which generates a ”negative” chemical pressure in the structure since Sr ion is bigger than Ca, was investigated [169]. In this case, the authors observed a decreasing in the $R\bar{3} \rightarrow Im\bar{3}$ SPT temperature, but any change in the electric properties was observed. These results suggested that high-pressures could induce structural changes in CMO. Thus, the aim of this study is to investigate the structural behavior of CMO under high hydrostatic pressures.

5.2. Experimental

Polycrystalline CMO powder was prepared at room temperature by Pechini method as described elsewhere [160]. For this purpose, stoichiometric amounts of $CaCO_3$ (Panreac, >98%) and $Mn(NO_3)2H_2O$ (Aldrich, >98%) were dissolved in a 1M citric acid aqueous solution and then added the same volume of ethylene 45 glycol. After, we diluted the obtained solution in 100 ml of water. The resulting solution was then heated at 200 ^{o}C until a highly viscous resin was formed, whose organic matter was decomposed at 400 ^{o}C obtaining the precursor powder. The precursor powder was placed in an agate mortar and ground carefully for about 20 minutes with a pestle until to get a homogenous black powder. The powder was heated in air at 800 ^{o}C/60 h, 900 ^{o}C/24 h (two times), and 950 ^{o}C/24 h (two times), respectively, with intermediate grinding and pelletizing.

5.3. Results and Discussions

Synchrotron X-ray Powder Diffraction (SXRPD) experiments were performed at the XDS beamline of the Brazilian Synchrotron Laboratory (LNLS) under high-pressure 54 conditions using monochromatic synchrotron radiation with λ = 0.602495 $^{\circ}A$. More details about this beamline can be found in Ref. [99]. High pressure was applied by using a diamond anvil cell (DAC) with Ne gas as pressure-transmitting media for hydrostatic conditions [99]. The patterns were collected at pressures up to 18.9 GPa. After closing the DAC, the initial pressure was 3.0 GPa. Therefore, the experiments were performed on the range from 3.0 GPa up to 18.9 GPa. The two-dimensional SXRPD patterns were integrated to provide intensity as a function of 2θ using the software FIT2D [102]. Le Bail method [170] was employed to obtain structural information using FullProf software [128] with initial lattice parameters obtained from the room pressure phase data [160]. The peak of Mn_3O_4 hausmannite secondary phase, which is common in CMO synthesis [160] was not taken into account in the fit. For high-pressure diffractograms, as a useful complementary tool to Le Bail method, the Dicvol06 [171] algorithm, available in the software WinPLOTR [172], was used to indexing the new phases. The higher figure of merit (*FoM*) [173] was used to check the reliability of the solutions, and the lattice parameters obtained from Dicvol06 were used to perform the Le Bail method.

Figure 19 shows the pressure-dependent SXRPD patterns obtained for CMO. The broad diffraction peak marked with $*$ around $2\theta = 17.2°$ is due to the stell gasket [27]. At the initial pressure, the known $R\bar{3}$ rhombohedral phase fits well the SXRPD pattern. Such a structure describes the CMO powder patterns up to 9.1 GPa, as it is shown in Figure 19(b). However, we can clearly observe a remarkable change in the crystalline structure at pressures higher than 9.9 GPa, when a peak splitting occurs approximately at 19.2^{o} (see Figure 19(b)), and a new peak can be observed around $2\theta = 17.0°$ at 13.3 GPa. The occurrence of new peaks indicates CMO would undergo a symmetry reduction.

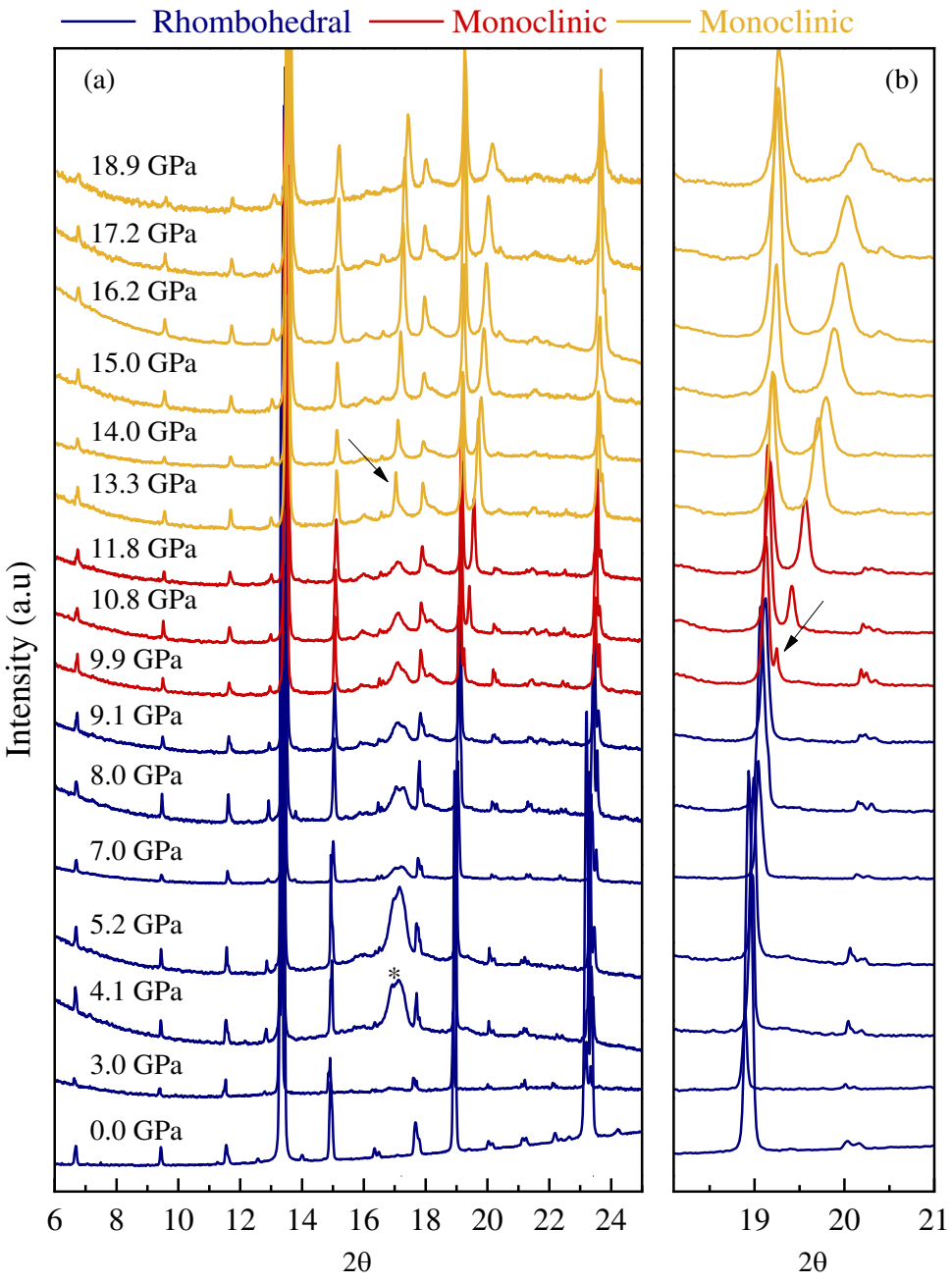

Figure 19: Pressure-dependent SXRPD diffractograms obtained for CMO. The asterisk symbol * mark the Bragg peak from the steel gasket. The arrows indicate the rise of new peaks at 9.9 and 13.3 GPa.

First, we checked if these transformations could be a decomposition since CMO can be decomposed into $CaMn_3O_6$ and Mn_2O_3 under thermodynamic changes. At high pressures, cubic Mn_2O_3 transforms into an orthorhombic structure [28]. However, for all investigated pressures by Hong *et al.* [28], its diffraction patterns exhibit a strong diffraction peak $2\theta = 9^o$, which is not observed in our diffraction patterns. Unfortunately, it was not reported investigations on $CaMn_3O_6$ under pressure. At room pressure, Hadermann *et al.* [29] reported that $CaMn_3O_6$

crystallizes into a monoclinic structure belonging to the $P2_1/a$ space group. Comparing CMO and $CaMn_3O_6$ diffraction patterns for pressure up to 18.9 GPa, we can see that no diffraction peaks exhibited by CMO coincide with $CaMn_3O_6$; while at 18.9 GPa, only two peaks around $2\theta = 15.25^o$ coincide. If we suppose that $CaMn_3O_6$ do not undergo any phase transformations at high pressure, due to the volume contraction should have a diffraction peak shifts. However, even with this shift, the diffraction patterns do not coincide. So, we can assume the transformation observed into CMO under pressure is not a decomposition into $CaMn_3O_6$ and Mn_2O_3, rather a structural phase transition (SPT).

The high-pressure patterns above 9.1 GPa were indexed with the best FoM using the Dicvol06 program [24] as a monoclinic system. Due to the limited angular range imposed by the diamond anvil cell, it was not possible to perform a complete structural resolution. Instead, a detailed investigation using the Le Bail method was applied to check the adequate symmetry of high-pressure patterns. The low-pressure patterns were successfully indexed with a rhombohedral structure (Figure 20a). Above 9.1 GPa, the new diffraction peaks belong to *hkl* family planes are prohibited in the rhombohedral structure, and the crystal lattice can no longer be described as a rhombohedral phase. In this structure, the extinction rules force the condition $-h + k + l = 3n$, in which n is an integer.

The splitting of the rhombohedral $(40\bar{2})$ peak at $2\theta \cong 19.2°$ is the onset of the first pressure-induced structural phase transition from a rhombohedral to a monoclinic system undergone by CMO for pressures above 9.9 GPa. Hence, the rhombohedral lattice parameters converter to a monoclinic one with $a_m \cong \sqrt{3}a_R$, $b_m \cong a_R$, $c_m \cong 1/2\, c_R$, and the monoclinic angle $\beta = 94.3°$. The pressure-dependence of lattice parameters is shown in Figure 21. The change in lattice parameters shows a reduction in the stacking along of [001] direction. Above 13.3 GPa, the high overlap of the broad peaks and a significant jump in the monoclinic angle followed by a change in the volume strongly suggest CMO undergo a new monoclinic phase transition (see Figure 21b,c). Besides, a new peak arising at $2\theta \cong 17.0°$ for pressures above 13.3 GPa has been observed in the SXRPD pattern. This peak became apparent, which was not evident in the range of 9.9 – 11.8 GPa, maybe to be overlapped with the steel gasket peak. Finally, subtle changes in the volume were observed for pressures higher than 17.0 GPa, which can be associated with low intensity and broadness of the peaks. Those changes suggest a new phase transformation of CMO; however, the pressure data are not sufficient to confirm the character of this transformation. A shear distortion model of the rhombohedral unit cell based

on monoclinic lattice parameters $1 + 3c_m \cos\beta / a_m$ [174] (Figure 21b) was performed and agreed with the phase transitions discussed here.

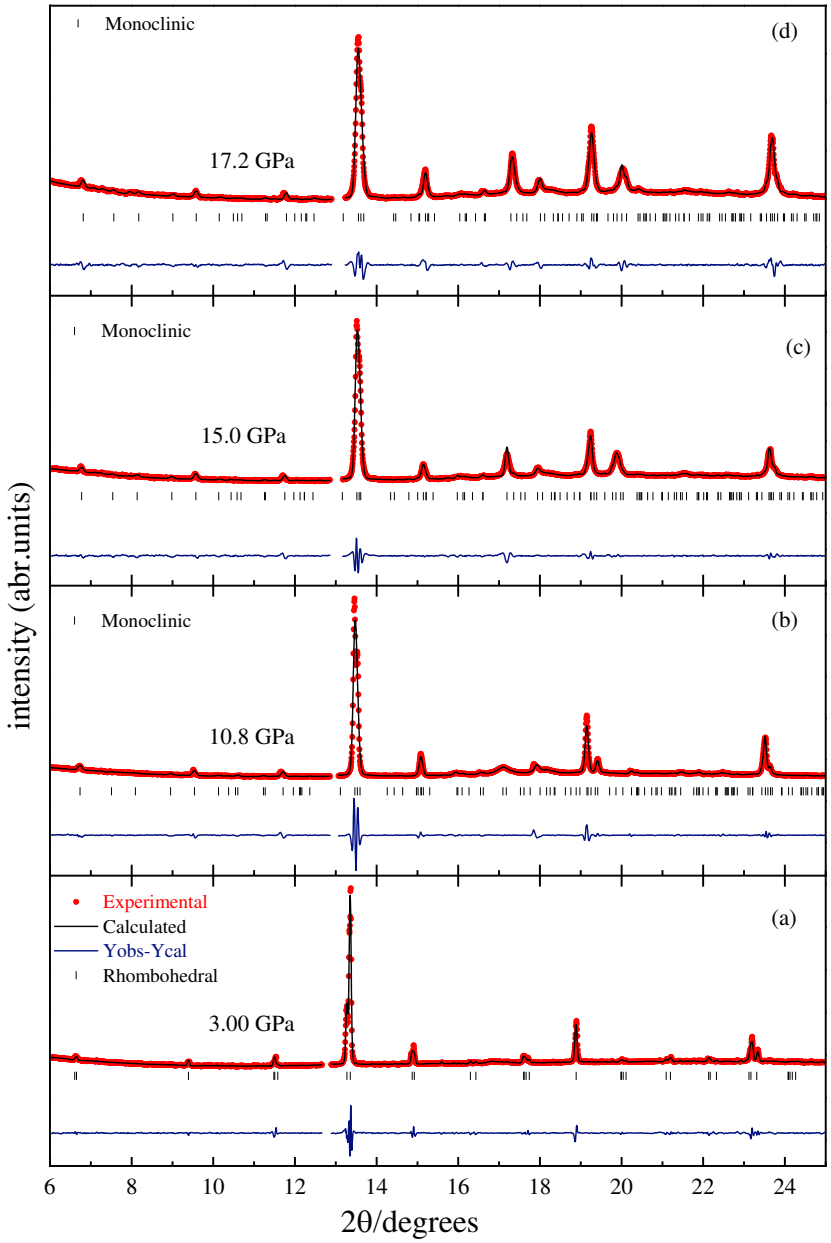

Figure 20: Le Bail fitting of SXRPD pattern of CMO at (a) 3.0 GPa, (b) 10.80 Gpa, (c) 15.0 GPa and (d) 17.2 GPa. The bars show Bragg reflection positions. The jump around 2θ ≅ 13.0° corresponds to the Mn3O4 hausmannite secondary phase peak exclude from the fits.

An orthorhombic model with lattice parameters close to monoclinic one was also proposed for high-pressures. The lattice parameters with $a_m \cong a_R$, $b_m \cong \sqrt{3}a_R$ agreed with a decrease in the symmetry of a rhombohedral to a C-centered orthorhombic symmetry [175]. This model adjusts the patterns up to 11.3 GPa, but above this pressure value, the Le Baill fit

did not provide reliable results, and a satisfactory orthorhombic model was not achieved. However, a search for a pseudosymmetry of the monoclinic lattice in the range of 9.9 -11.3 GPa (using the program implemented in the Bilbao Crystallographic Server platform) suggests a C-centered orthorhombic system with a high tolerance factor. In comparison, a pseudosymmetry search for pressures high than 13.3 GPa indicates that the monoclinic system is the most probable. Therefore, despite the robustness of the Le Bail fit for the orthorhombic model, the monoclinic system proved to be more reliable. For clarity, the lattice parameters of the orthorhombic model are included in Figure 21a,c.

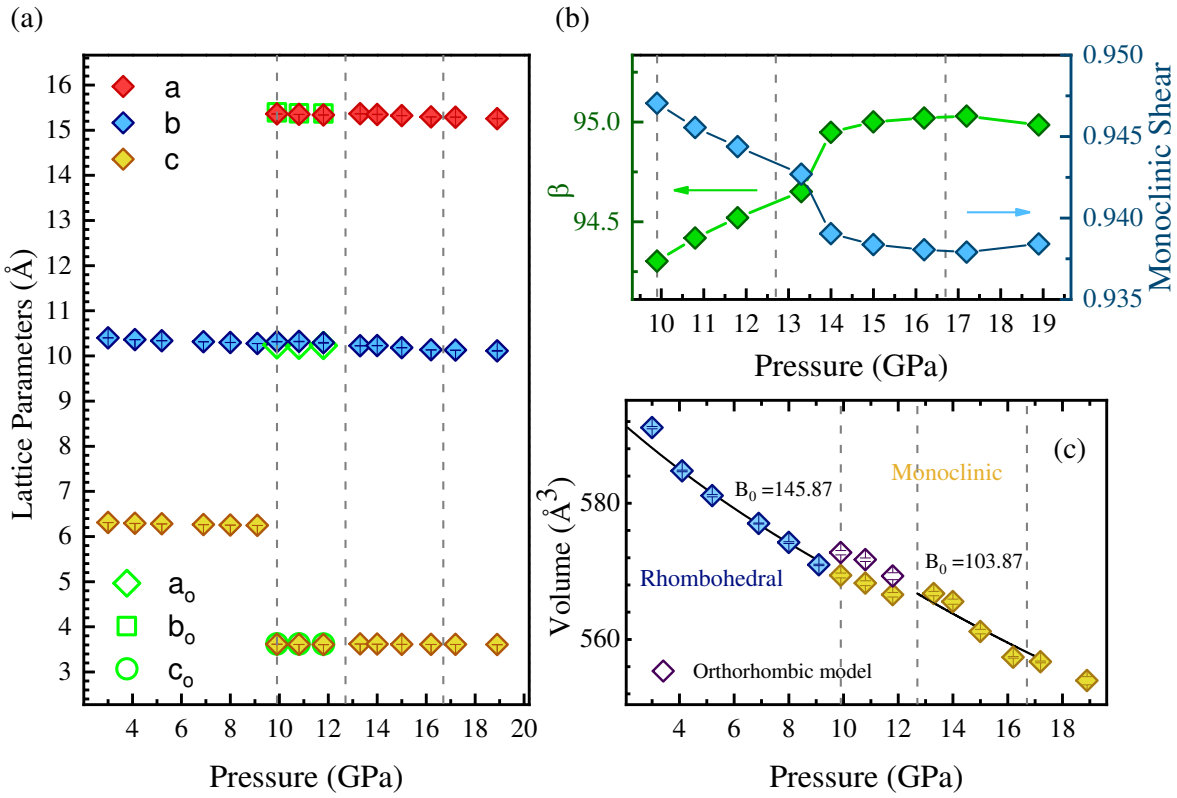

Figure 21: Pressure-dependent crystalline structural data for CMO. (a) Lattice parameters - green dots correspond to the lattice parameter of the orthorhombic model. (b) The monoclinic angle β (green line) and the monoclinic shear (blue line). (c) Volume - black lines indicate the pressure-dependent volume fit by the Birch-Murnaghan equation. Red dots correspond to the orthorhombic model.

Unfortunately, the number of diffraction peaks hindered the determination of the crystalline structure, just the crystalline system in each phase was identified. However, we can investigate the bulk modulus from the volume curves. The Bulk modulus can be obtained from Birch–Murnaghan equation of state [176,177].

$$P(V) = \left[\left(\frac{V_0}{V}\right)^{7/3} - \left(\frac{V_0}{V}\right)^{5/3}\right]\left\{1 + \frac{3}{4}(B_0' - 4)\left[\left(\frac{V_0}{V}\right)^{2/3} - 1\right]\right\} \quad (2)$$

where P is the pressure, V_o is the reference volume, V is the deformed volume, B_o is the bulk modulus, and B_0' is the bulk modulus derivative with relation to the pressure. The Birch–Murnaghan (BM) fit is shown in Figure 21c for both rhombohedral and monoclinic phases. The black line in Figure 21c shows the best BM fit for the pressure-dependent volume of CMO. We can see the volume decreasing due to the pressure increase is almost linear (linear fits with $R^2 > 0.97$), which suggests an elastic constant (derivative of the Bulk modulus) approximately equal 4. Assuming this value in both phases, which is a usual procedure in linear behaviors in similar materials (see Ref. [178]), the best fit in the rhombohedral phase shows that the bulk modulus is 146 ± 4 GPa and in the monoclinic phase is 103 ± 3 GPa. These values are compatible with those observed in $LaCu_3Fe_4O_{12}$ by Long *et al.* [178]. The values of the first monoclinic phase were not fitted to the BM due to the limited pressure-volume data.

As discussed before, $NaMn_7O_{12}$ was submitted to high hydrostatic pressure up to 40 GPa, but any SPT was observed. The crystalline structure of this compound was investigated using single-crystal X-ray diffraction, whereas electrical resistance measurements carried out on powdered samples showed an insulator-to-semimetal transformation in the electric behavior. Also, $LaCu_3Fe_4O_{12}$ exhibits an isostructural phase transition at 3.5 GPa [178], in which a first-order charge-transfer transition from a $LaCu_3\,Fe_4\,O_{12}$ low-pressure phase to a high-pressure $LaCu_3^{2+}Fe_4^{3.75+}O_{12}$ was observed. In both cases, $NaMn_7O_{12}$ and $LaCu_3Fe_4O_{12}$, a volume reduction was found at the electric transitions. Finally, $CaCu_3Ti_4O_{12}$ was investigated up to 46 GPa by synchrotron X-ray powder diffraction, and any SPT was observed [179]. Therefore, CMO is one of the first quadruple perovskites in which it is seen as a pressure-induced non-isostructural phase transition.

5.4. Conclusions

In conclusion, we showed that CMO undergoes two structural phase transitions under hydrostatic pressure. The first one around 9.9 GPa and the second one above 13.3 GPa. In the first transition, the rhombohedral structure transforms into a monoclinic structure, while in the second phase transition, CMO has undergone a shear distortion of the first monoclinic phase, which is accompanied by a jump in the monoclinic angle β. For pressures high 17.0 GPa subtle changes in the volume suggest CMO can undergo a new phase transition.

8. General Conclusions

The main structural characteristic of the layered related-perovskites structures is the octahedra framework, which can be modified varying the temperature or applying hydrostatic pressure. Once the cations displacements and octahedral distortions are pressure/temperature-sensitive, changes in the multiferroic, optical, and electronic properties can be expected at extreme conditions [15,54]. Therefore, the *in situ* high-pressure/temperature experiments are a straightforward and robust way to explore the structural and ferroic properties of these materials [16,59,222,225,227]. In this thesis, the physical properties of several perovskites-based structures were investigated at extreme conditions and correlated with structural phase transitions.

The crystalline structure of the multiferroic compounds $Bi_5Ti_3FeO_{15}$ (BFTO) and $CaMn_7O_{12}$ (CMO) was investigated under high-pressure conditions. For BFTO, using synchrotron X-ray powder diffraction and Raman spectroscopy, three structural phase transitions were identified. Around 3.2 GPa, BFTO undergoes an orthorhombic-tetragonal transformation, which exhibits a second-order character based on the analysis of the symmetry-breaking strain. Above 7.5 GPa, a phase transition from tetragonal to a new orthorhombic phase is observed. The discontinuity in the strain suggests this transformation the evidence of a first-order phase transition. Also, subtle changes in the Caglioti's function parameters and Raman spectra above 10.5 GPa indicate the onset of another phase, whose symmetry was still unknown. The CMO undergoes two structural phase transitions under hydrostatic pressure. The first one happens around 9.9 GPa and the second one above 13.3 GPa. In the first transition, the rhombohedral structure transforms into a monoclinic structure, while in the second phase transition, CMO has undergone a shear distortion of the first monoclinic phase, which is accompanied by a jump in the monoclinic angle β. For pressures high 17.0 GPa subtle changes in the volume suggest CMO can undergo a new phase transition.

The all-inorganic $Cs_2PbI_2Cl_2$ Ruddlesden-Popper phase was investigated at low temperatures employing Stokes and Anti-Stokes Raman measurements and photoluminesce in the range of (300 – 16 K). The Raman spectra revealed no significant changes as temperature decrease, indicating that no structural phase transitions are expected at low temperatures. However, at ambient conditions, the Raman spectra of $Cs_2PbI_2Cl_2$ is marked by the presence of

nonresonant overtones, which can be associated with the intrinsic structure of natural quantum wells. The linewidth temperature dependence analyses of the photoluminesce spectra revealed a strong electron-phonon coupling. The most intense infrared active LO phonons were observed to couple with the second photoluminesce, whereas the new photoluminescence band rising around 60 K is observed to couple with the first overtone $\omega_{01} = 115 \pm 19$ cm^{-1}. The results suggest that the second-order Raman scattering is mediated by bound excitons within the $Cs_2PbI_2Cl_2$ Ruddlesden-Popper structure.

The structure evolution of luminescent Cs_4PbBr_6 single crystals under high-pressure conditions by synchrotron X-ray diffraction and Raman spectroscopy was investigated. The structural analysis demonstrated that its structure undergoes two phase transitions around 3.2 and 4.5 GPa. The first phase transition was also observed in nanocrystals, but the second seems to be characteristic of bulk crystals. In our Cs_4PbBr_6 bulk SCs, the PL emission is completely suppressed at 3.5 GPa, indicating that in this structure, the monoclinic phase does not produce a favorable condition for PL phenomena. In line with the other 0D perovskites systems studies under high-pressure conditions, the PL of our system is very similar to the one reported for $Cs_3Bi_2I_9$. Our findings provide valuable insight into the luminescence mechanism making significant inroads into green photoluminescence origin understanding and shedding light on the structural characteristics and PL properties of luminescent Cs_4PbBr_6 single crystals under extremes conditions.

9. Publications

Publications related to this thesis

1. **Ferreira, W.C**.; Rodrigues, C.L.C.; Araújo, B.S.; Aguiar, F.A.A.; Nonato, A.; Fechine, P.B.A.; Paschoal, C.W.A.; Ayala, A.P. Pressure-induced structural phase transitions in the multiferroic four-layers Aurivillius ceramic $Bi_5FeTi_3O_{15}$. *Accepted – Ceramics International*, 2020.

2. **Ferreira, W.C**.; Nonato, A.; Yañez-Vilar, S.; Mira, J.; Sánchez-Andujar, M.; Señarís-Rodríguez, M.A.; Ayala, A.P.; Paschoal, C.W.A. Pressure-induced structural phase transitions on multiferroic $CaMn_7O_{12}$. *Submitted – Journal of Alloys and Compounds*,2020.

3. **Ferreira, W.C**.; Dieric S. de Abreu.; Bruno S. Araújo.; Fabio E. O. Medeiros.; Carlos W. A. Pachoal.; Alejandro P. Ayala. Strong Electron-Phonon Coupling in 2d Ruddlesden−Popper Halide Perovskite $Cs_2PbI_2Cl_2$, *Under final revisions,* 2020.

4. **Ferreira, W.C**.; Araújo, B.S.; Gomez, M.A.P.; Oliveira, F.M.; Silva, C.B.; Freire, P.T.C.; Souza-Neto, N.M.; Paschoal, C.W.A.; Ayala, A.P. Pressure-Induced Structural phase transition and anomalous photoluminescence behavior in luminescent Cs_4PbBr_6 single crystal. *Under final revisions, 2020.*

Other Publications

1. Dantas, Natália C.F.M.; Duarte, Oscar S.; **Ferreira, Wellington C.**; Ayala, Alejandro P.; Rezende, Carla F.; Feitosa, Caroline V. Plastic Intake Does Not Depend on Fish Eating Habits: Identification of Microplastics in the Stomach Contents of Fish on An Urban Beach in Brazil. *Marine Pollution Bulletin*, v. 153, p. 110959, 2020. https://doi.org/10.1016/j.marpolbul.2020.110959.

2. Nonato, A.; Lima, P.H.M.; **Ferreira, W.C**.; Silva, R.X.; Costa, N.L.M.; Paschoal, A.R.; Ayala, A.P.; Paschoal, C.W.A. Pressure-Induced Structural Phase Transition in Multiferroic $KBiFe_2O_5$. *Journal of Alloys and Compounds.,* v.787, p.1195 - 1203, 2019. https://doi.org/10.1016/j.jallcom.2019.02.064.

3. Santana, M.S.A.; Oliveira, Y.S.; Fonseca, J.C.; **Ferreira, W.C**.; Neto, V.S.; Ayala, A.P. Stability of Ceftazidime Pentahydrate investigated by Thermal Analysis Techniques. *Journal of Pharmaceutical Sciences,* v. 109, p. 1324-1329, 2019. https://doi.org/10.1016/j.xphs.2019.11.018.

4. Araújo, B.S.; **Ferreira, W.C**.; Gomes, M.A.P.; Oliveira, F.M.; Freire, P.T.C.; Paschoal, C.W.A.; Ayala, A.P. Structural Phase Transition and Luminescence Properties of the Halide $CsPb_2(Br_{1-x}I_x)_5$ Under High-Pressure Conditions. *Under final revisions*, 2020.

5. M. A. P. Gómez.; B. S. Araújo.; **W. C. Ferreira**.; F.E.O Medeiros.; Neto, V. S.; W. A. Paschoal.; A. P. Ayala. Temperature Behavior of 2D Halide Perovskite $CsPb_2Br_5$ Doped with Iodide Single Crystals. *Under final revisions*, 2020.

6. Araújo, B.S.; **Ferreira, W.C**.; Paschoal, A.R.; Paschoal, C.W.A.; J. P. Attfield.; Ayala, A.P. High-Pressure Behavior of Multiferroic $BiCrO_3$. *Under final revisions*, 2020.

10. References

[1] C. Ball, B. Begg, D. Cookson, G. Thorogood, E. Vance, Structures in the System $CaTiO_3/SrTiO_3$, **J. Solid State Chem. 139 (1998)** 238–247. https://doi.org/10.1006/jssc.1998.7836.

[2] B. J. Kennedy, C. J. Howard, Y. Kubota, K. Kato, Phase transition behaviour in the A-site deficient perovskite oxide $La_{1/3}NbO_3$, **J. Solid State Chem. 177 (2004)** 4552–4556. https://doi.org/10.1016/j.jssc.2004.08.047.

[3] R. J. D. Tilley, Perovskites, **John Wiley & Sons, Ltd, Chichester, UK, 2016**. https://doi.org/10.1002/9781118935651.

[4] V. Gonzalez-Pedro, E. J. Juarez-Perez, W. S. Arsyad, E.M. Barea, F. Fabregat-Santiago, I. Mora-Sero, J. Bisquert, General Working Principles of $CH_3NH_3PbX_3$ Perovskite Solar Cells, **Nano Lett. 14 (2014)** 888–893. https://doi.org/10.1021/nl404252e.

[5] M. Telychko, J. Lu, Recent advances in atomic imaging of organic-inorganic hybrid perovskites, **Nano Mater. Sci. 1 (2019)** 260–267. https://doi.org/10.1016/j.nanoms.2019.10.005.

[6] B. Saparov, D. B. Mitzi, Organic-Inorganic Perovskites: Structural Versatility for Functional Materials Design, **Chem. Rev. 116 (2016)** 4558–4596. https://doi.org/10.1021/acs.chemrev.5b00715.

[7] Q. Tu, I. Spanopoulos, S. Hao, C. Wolverton, M. G. Kanatzidis, G. S. Shekhawat, V. P. Dravid, Probing Strain-Induced Band Gap Modulation in 2D Hybrid Organic-Inorganic Perovskites, **ACS Energy Lett. 4 (2019)** 796–802. https://doi.org/10.1021/acsenergylett.9b00120.

[8] V. M. Goldschmidt, Die Gesetze der Krystallochemie, **Naturwissenschaften. 14 (1926)** 477–485. https://doi.org/10.1007/BF01507527.

[9] N. A. Spaldin, R. Ramesh, Advances in magnetoelectric multiferroics, **Nat. Mater. 18 (2019)** 203–212. https://doi.org/10.1038/s41563-018-0275-2.

[10] H. J. Snaith, Present status and future prospects of perovskite photovoltaics, **Nat. Mater. 17 (2018)** 372–376. https://doi.org/10.1038/s41563-018-0071-z.

[11] P. K. Nayak, S. Mahesh, H. J. Snaith, D. Cahen, Photovoltaic solar cell technologies: analysing the state of the art, **Nat. Rev. Mater. 4 (2019)** 269–285. https://doi.org/10.1038/s41578-019-0097-0.

[12] H. Schmid, Multi-ferroic magnetoelectrics, **Ferroelectrics. 162 (1994)** 317–338. https://doi.org/10.1080/00150199408245120.

[13] M. Fiebig, T. Lottermoser, D. Meier, M. Trassin, The evolution of multiferroics, **Nat.**

Rev. Mater. 1 (2016). https://doi.org/10.1038/natrevmats.2016.46.

[14] Z. Ma, Z. Liu, S. Lu, L. Wang, X. Feng, D. Yang, K. Wang, G. Xiao, L. Zhang, S.A.T. Redfern, B. Zou, Pressure-induced emission of cesium lead halide perovskite nanocrystals, **Nat. Commun. 9 (2018)** 4506. https://doi.org/10.1038/s41467-018-06840-8.

[15] E. Gilioli, L. Ehm, High pressure and multiferroics materials: a happy marriage, **IUCrJ. 1 (2014)** 590–603. https://doi.org/10.1107/S2052252514020569.

[16] L. Wang, K. Wang, G. Xiao, Q. Zeng, B. Zou, Pressure-Induced Structural Evolution and Band Gap Shifts of Organometal Halide Perovskite-Based Methylammonium Lead Chloride, **J. Phys. Chem. Lett. 7 (2016)** 5273–5279. https://doi.org/10.1021/acs.jpclett.6b02420.

[17] Z. Ma, F. Li, G. Qi, L. Wang, C. Liu, K. Wang, G. Xiao, B. Zou, Structural stability and optical properties of two-dimensional perovskite-like $CsPb_2Br_5$ microplates in response to pressure, **Nanoscale. 11 (2019)** 820–825. https://doi.org/10.1039/C8NR05684F.

[18] L. Zhang, L. Wu, K. Wang, B. Zou, Pressure-Induced Broadband Emission of 2D Organic-Inorganic Hybrid Perovskite $(C_6H_5C_2H_4NH_3)_2PbBr_4$, **Adv. Sci. 6 (2019)** 1801628. https://doi.org/10.1002/advs.201801628.

[19] X. Lü, W. Yang, Q. Jia, H. Xu, Pressure-induced dramatic changes in organic-inorganic halide perovskites, **Chem. Sci. 8 (2017)** 6764–6776. https://doi.org/10.1039/c7sc01845b.

[20] A. M. Glazer, The classification of tilted octahedra in perovskites, **Acta Crystallogr. Sect. B Struct. Crystallogr. Cryst. Chem. 28 (1972)** 3384–3392. https://doi.org/10.1107/s0567740872007976.

[21] A. M. Glazer, Simple ways of determining perovskite structures, **Acta Crystallogr. Sect. A. 31 (1975)** 756–762. https://doi.org/10.1107/S0567739475001635.

[22] A. K. Kundu, Magnetic Perovskites: Synthesis, Structure and Physical Properties, **Springer India, New Delhi, 2016.** https://doi.org/10.1007/978-81-322-2761-8.

[23] G. King, P.M. Woodward, Cation ordering in perovskites, **J. Mater. Chem. 20 (2010)** 5785–5796. https://doi.org/10.1039/b926757c.

[24] W. Zhou, H. Deng, L. Yu, P. Yang, J. Chu, Optical band-gap narrowing in perovskite ferroelectric ABO_3 ceramics (A=Pb, Ba; B=Ti) by ion substitution technique, **Ceram. Int. 41 (2015)** 13389–13392. https://doi.org/10.1016/j.ceramint.2015.07.127.

[25] A. Swarnkar, W.J. Mir, A. Nag, Can B-Site Doping or Alloying Improve Thermal- and Phase-Stability of All-Inorganic $CsPbX_3$ (X = Cl, Br, I) Perovskites?, **ACS Energy Lett. 3 (2018)** 286–289. https://doi.org/10.1021/acsenergylett.7b01197.

[26] A. Hossain, P. Bandyopadhyay, S. Roy, An overview of double perovskites $A_2B'B''O_6$ with small ions at A site: Synthesis, structure and magnetic properties, **J. Alloys Compd.**

740 (2018) 414–427. https://doi.org/10.1016/j.jallcom.2017.12.282.

[27] T. Maiti, M. Saxena, P. Roy, Double perovskite ($Sr_2B'B''O_6$) oxides for high-temperature thermoelectric power generation—A review, **J. Mater. Res. 34 (2019)** 107–125. https://doi.org/10.1557/jmr.2018.376.

[28] A. K. Azad, S. A. Ivanov, S. G. Eriksson, J. Eriksen, H. Rundlöf, R. Mathieu, P. Svedlindh, Synthesis, crystal structure, and magnetic characterization of the double perovskite Ba_2MnWO_6, **Mater. Res. Bull. 36 (2001)** 2215–2228. https://doi.org/10.1016/S0025-5408(01)00707-3.

[29] M. T. Anderson, K. R. Poeppelmeier, Lanthanum copper tin oxide (La_2CuSnO_6): a new perovskite-related compound with an unusual arrangement of B cations, **Chem. Mater. 3 (1991)** 476–482. https://doi.org/10.1021/cm00015a022.

[30] Z. Song, J. Zhao, Q. Liu, Luminescent perovskites: recent advances in theory and experiments, Inorg. **Chem. Front. 6 (2019)** 2969–3011. https://doi.org/10.1039/C9QI00777F.

[31] R. Mani, N. S. P. Bhuvanesh, K. V. Ramanujachary, W. Green, S.E. Lofland, J. Gopalakrishnan, A novel one-pot metathesis route for the synthesis of double perovskites, $Ba_3MM'_2O_9$ (M = Mg, Ni, Zn; M′ = Nb, Ta) with 1:2 ordering of M and M′ atoms, **J. Mater. Chem. 17 (2007)** 1589–1592. https://doi.org/10.1039/B616238J.

[32] M.W. Lufaso, Crystal Structures, Modeling, and Dielectric Property Relationships of 2:1 Ordered $Ba_3MM'_2O_9$ (M = Mg, Ni, Zn; M‘ = Nb, Ta) Perovskites, **Chem. Mater. 16 (2004)** 2148–2156. https://doi.org/10.1021/cm049831k.

[33] T. Sivakumar, K. Ramesha, S. E. Lofland, K. V. Ramanujachary, G. N. Subbanna, J. Gopalakrishnan, 2D−3D Transformation of Layered Perovskites through Metathesis: Synthesis of New Quadruple Perovskites $A_2La_2CuTi_3O_{12}$ (A = Sr, Ca), **Inorg. Chem. 43 (2004)** 1857–1864. https://doi.org/10.1021/ic035358l.

[34] W. Sławiński, R. Przeniosło, I. Sosnowska, M. Bieringer, Structural and magnetic modulations in $CaCu_xMn_{7-x}O_{12}$, **J. Phys. Condens. Matter. 22 (2010)** 186001. https://doi.org/10.1088/0953-8984/22/18/186001.

[35] S. Vasala, M. Karppinen, $A_2B'B''O_6$ perovskites: A review, **Prog. Solid State Chem. 43 (2015)** 1–36. https://doi.org/10.1016/j.progsolidstchem.2014.08.001.

[36] A. A. Belik, Rise of A-site columnar-ordered $A_2A'A''B_4O_{12}$ quadruple perovskites with intrinsic triple order, **Dalt. Trans. 47 (2018)** 3209–3217. https://doi.org/10.1039/c7dt04490a.

[37] F. Mezzadri, G. Calestani, M. Calicchio, E. Gilioli, F. Bolzoni, R. Cabassi, M. Marezio, A. Migliori, Synthesis and characterization of multiferroic $BiMn_7O_{12}$, **Phys. Rev. B Condens. Matter Mater. Phys. 79 (2009)** 1–4. https://doi.org/10.1103/PhysRevB.79.100106.

[38] A. A. Belik, Y. S. Glazkova, Y. Katsuya, M. Tanaka, A. V. Sobolev, I. A. Presniakov,

Low-Temperature Structural Modulations in $CdMn_7O_{12}$, $CaMn_7O_{12}$, $SrMn_7O_{12}$, and $PbMn_7O_{12}$ Perovskites Studied by Synchrotron X-ray Powder Diffraction and Mössbauer Spectroscopy, **J. Phys. Chem. C. 120 (2016)** 8278–8288. https://doi.org/10.1021/acs.jpcc.6b01649.

[39] K. Zheng, T. Pullerits, Two Dimensions Are Better for Perovskites, **J. Phys. Chem. Lett. 10 (2019)** 5881–5885. https://doi.org/10.1021/acs.jpclett.9b01568.

[40] Y. Chen, Y. Sun, J. Peng, J. Tang, K. Zheng, Z. Liang, 2D Ruddlesden-Popper Perovskites for Optoelectronics, **Adv. Mater. 30 (2018)** 1703487. https://doi.org/10.1002/adma.201703487.

[41] H. Ren, S. Yu, L. Chao, Y. Xia, Y. Sun, S. Zuo, F. Li, T. Niu, Y. Yang, H. Ju, B. Li, H. Du, X. Gao, J. Zhang, J. Wang, L. Zhang, Y. Chen, W. Huang, Efficient and stable Ruddlesden–Popper perovskite solar cell with tailored interlayer molecular interaction, **Nat. Photonics. 14 (2020)** 154–163. https://doi.org/10.1038/s41566-019-0572-6.

[42] S. N. Ruddlesden, P. Popper, New compounds of the K_2NiF_4 type, **Acta Crystallogr. 10 (1957)** 538–539. https://doi.org/10.1107/s0365110x57001929.

[43] S. N. Ruddlesden, P. Popper, The compound $Sr_3Ti_2O_7$ and its structure, **Acta Crystallogr. 11 (1958)** 54–55. https://doi.org/10.1107/s0365110x58000128.

[44] W. K. Chong, D. Giovanni, T. C. Sum, Halide Perovskites, **Wiley VCH Verlag GmbH & Co. KGaA, Weinheim, Germany, 2018**. https://doi.org/10.1002/9783527800766.

[45] M. Mostovoy, Multiferroics: A whirlwind of opportunities., **Nat. Mater. 9 (2010)** 188–190. https://doi.org/10.1038/nmat2700.

[46] K. Dorr, A. Herklotz, Materials science: Two steps for a magnetoelectric switch, **Nature. 516 (2014)** 337–338. https://doi.org/10.1038/516337a.

[47] J. F. Scott, Searching for new ferroelectrics and multiferroics: A user's point of view, **Npj Comput. Mater. 1 (2015)** 15006. https://doi.org/10.1038/npjcompumats.2015.6.

[48] M. M. Vopson, Fundamentals of Multiferroic Materials and Their Possible Applications, **Crit. Rev. Solid State Mater. Sci. 40 (2015)** 223–250. https://doi.org/10.1080/10408436.2014.992584.

[49] S. Dong, J.-M. Liu, S. W. Cheong, Z. Ren, Multiferroic materials and magnetoelectric physics: symmetry, entanglement, excitation, and topology, **Adv. Phys. 64 (2015)** 519–626. https://doi.org/10.1080/00018732.2015.1114338.

[50] J. T. Heron, D. G. Schlom, R. Ramesh, Electric field control of magnetism using $BiFeO_3$ based heterostructures, **Appl. Phys. Rev. 1 (2014)** 021303. https://doi.org/10.1063/1.4870957.

[51] M. Fiebig, Revival of the magnetoelectric effect, **J. Phys. D. Appl. Phys. 38 (2005)** R123–R152. https://doi.org/10.1088/0022-3727/38/8/R01.

[52] N. A. Spaldin, M. Fiebig, M. Mostovoy, The toroidal moment in condensed-matter physics and its relation to the magnetoelectric effect, **J. Phys. Condens. Matter. 20 (2008)**. https://doi.org/10.1088/0953-8984/20/43/434203.

[53] N. A. Spaldin, S.W. Cheong, R. Ramesh, Multiferroics: Past, present, and future, **Phys. Today. 63 (2010)** 38–43. https://doi.org/10.1063/1.3502547.

[54] G. A. Samara, Pressure and temperature dependence of the dielectric properties and phase transitions of the ferroelectric perovskites: $PbTiO_3$ and $BaTiO_3$, **Ferroelectrics. 2 (1971)** 277–289. https://doi.org/10.1080/00150197108234102.

[55] J. R. Teague, R. Gerson, W. J. James, Dielectric hysteresis in single crystal $BiFeO_3$, **Solid State Commun. 8 (1970)** 1073–1074. https://doi.org/10.1016/0038-1098(70)90262-0.

[56] G. Zhang, H. Wu, G. Li, Q. Huang, C. Yang, F. Huang, F. Liao, J. Lin, New high Tc multiferroics $KBiFe_2O_5$ with narrow band gap and promising photovoltaic effect, **Sci. Rep. 3 (2013)** 1265. https://doi.org/10.1038/srep01265.

[57] G. Zhang, F. Liu, T. Gu, Y. Zhao, N. Li, W. Yang, S. Feng, Enhanced Ferroelectric and Visible-Light Photoelectric Properties in Multiferroic $KBiFe_2O_5$ via Pressure-Induced Phase Transition, **Adv. Electron. Mater. 3 (2017)** 1600498. https://doi.org/10.1002/aelm.201600498.

[58] M. Zhang, Z. Wang, S. Lin, Y. Wang, Y. Pan, Investigation on a new multiferroic compound $KBiFe_2O_5$: Structural, optical, electrical and magnetic properties, **J. Alloys Compd. 699 (2017)** 561–566. https://doi.org/10.1016/j.jallcom.2017.01.041.

[59] A. Nonato, P. H. M. Lima, W. C. Ferreira, R. X. Silva, N. L. M. Costa, A. R. Paschoal, A.P. Ayala, C.W.A. Paschoal, Pressure-induced structural phase transition in multiferroic $KBiFe_2O_5$, **J. Alloys Compd. 787 (2019)** 1195–1203. https://doi.org/10.1016/j.jallcom.2019.02.064.

[60] A. Kumar Jena, A. Kulkarni, T. Miyasaka, Halide Perovskite Photovoltaics: Background, Status, and Future Prospects, **Chem. Rev. (2018)**. https://doi.org/10.1021/acs.chemrev.8b00539.

[61] E. Mosconi, C. Quarti, T. Ivanovska, G. Ruani, F. De Angelis, Structural and electronic properties of organo-halide lead perovskites: A combined IR-spectroscopy and ab initio molecular dynamics investigation, **Phys. Chem. Chem. Phys. 16 (2014)** 16137–16144. https://doi.org/10.1039/c4cp00569d.

[62] S. De Wolf, J. Holovsky, S. J. Moon, P. Löper, B. Niesen, M. Ledinsky, F. J. Haug, J. H. Yum, C. Ballif, Organometallic halide perovskites: Sharp optical absorption edge and its relation to photovoltaic performance, **J. Phys. Chem. Lett. 5 (2014)** 1035–1039. https://doi.org/10.1021/jz500279b.

[63] Q. Zhang, Y. Yin, All-Inorganic Metal Halide Perovskite Nanocrystals: Opportunities and Challenges, **ACS Cent. Sci. 4 (2018)** 668–679. https://doi.org/10.1021/acscentsci.8b00201.

[64] D. P. Nenon, J.A. Christians, L. M. Wheeler, J. L. Blackburn, E. M. Sanehira, B. Dou, M. L. Olsen, K. Zhu, J. J. Berry, J. M. Luther, Structural and chemical evolution of methylammonium lead halide perovskites during thermal processing from solution, **Energy Environ. Sci. 9 (2016)** 2072–2082. https://doi.org/10.1039/C6EE01047D.

[65] P. Ramasamy, D. H. Lim, B. Kim, S. H. Lee, M. S. Lee, J. S. Lee, All-inorganic cesium lead halide perovskite nanocrystals for photodetector applications, **Chem. Commun. 52 (2016)** 2067–2070. https://doi.org/10.1039/C5CC08643D.

[66] J. Song, J. Li, X. Li, L. Xu, Y. Dong, H. Zeng, Quantum Dot Light-Emitting Diodes Based on Inorganic Perovskite Cesium Lead Halides ($CsPbX_3$), **Adv. Mater. 27 (2015)** 7162–7167. https://doi.org/10.1002/adma.201502567.

[67] M. Li, X. Zhang, Y. Du, P. Yang, Colloidal $CsPbX_3$(X = Br, I, Cl) NCs: Morphology controlling, composition evolution, and photoluminescence shift, **J. Lumin. 190 (2017)** 397–402. https://doi.org/10.1016/j.jlumin.2017.05.080.

[68] M. A. Green, A. Ho-Baillie, H. J. Snaith, The emergence of perovskite solar cells, **Nat. Photonics. 8 (2014)** 506–514. https://doi.org/10.1038/nphoton.2014.134.

[69] S. D. Stranks, H.J. Snaith, Metal-halide perovskites for photovoltaic and light-emitting devices, **Nat. Nanotechnol. 10 (2015)** 391–402. https://doi.org/10.1038/nnano.2015.90.

[70] X. Qi, Y. Zhang, Q. Ou, S. T. Ha, C.W. Qiu, H. Zhang, Y.B. Cheng, Q. Xiong, Q. Bao, Photonics and Optoelectronics of 2D Metal-Halide Perovskites, **Small. 14 (2018)** 1–16. https://doi.org/10.1002/smll.201800682.

[71] A. Jodlowski, D. Rodríguez-Padrón, R. Luque, G. de Miguel, Alternative Perovskites for Photovoltaics, **Adv. Energy Mater. 8 (2018)** 1703120. https://doi.org/10.1002/aenm.201703120.

[72] L. Protesescu, S. Yakunin, M.I. Bodnarchuk, F. Krieg, R. Caputo, C.H. Hendon, R.X. Yang, A. Walsh, M. V. Kovalenko, Nanocrystals of Cesium Lead Halide Perovskites ($CsPbX_3$, X = Cl, Br, and I): Novel Optoelectronic Materials Showing Bright Emission with Wide Color Gamut, **Nano Lett. 15 (2015)** 3692–3696. https://doi.org/10.1021/nl5048779.

[73] F. Zhang, H. Zhong, C. Chen, X. Wu, X. Hu, H. Huang, J. Han, B. Zou, Y. Dong, Brightly Luminescent and Color-Tunable Colloidal $CH_3NH_3PbX_3$ (X = Br, I, Cl) Quantum Dots: Potential Alternatives for Display Technology, **ACS Nano. 9 (2015)** 4533–4542. https://doi.org/10.1021/acsnano.5b01154.

[74] M. Grätzel, The light and shade of perovskite solar cells, **Nat. Mater. 13 (2014)** 838–842. https://doi.org/10.1038/nmat4065.

[75] H. J. Snaith, Perovskites: The emergence of a new era for low-cost, high-efficiency solar cells, **J. Phys. Chem. Lett. 4 (2013)** 3623–3630. https://doi.org/10.1021/jz4020162.

[76] R. J. Sutton, G.E. Eperon, L. Miranda, E.S. Parrott, B.A. Kamino, J. B. Patel, M.T. Hörantner, M.B. Johnston, A. A. Haghighirad, D. T. Moore, H. J. Snaith, Bandgap-

Tunable Cesium Lead Halide Perovskites with High Thermal Stability for Efficient Solar Cells, **Adv. Energy Mater. 6 (2016)** 1502458. https://doi.org/10.1002/aenm.201502458.

[77] Q. Van Le, K. Hong, H.W. Jang, S.Y. Kim, Halide Perovskite Quantum Dots for Light-Emitting Diodes: Properties, Synthesis, Applications, and Outlooks, **Adv. Electron. Mater. 1800335 (2018)** 1800335. https://doi.org/10.1002/aelm.201800335.

[78] N. Kitazawa, Y. Watanabe, Y. Nakamura, Optical properties of $CH_3NH_3PbX_3$ (X = halogen) and their mixed-halide crystals, **Journal of Materials Science 37 (2002)** 3585–3587. https://doi.org/10.1023/A:1016584519829.

[79] Y. Wang, X. Lü, W. Yang, T. Wen, L. Yang, X. Ren, L. Wang, Z. Lin, Y. Zhao, Pressure-Induced Phase Transformation, Reversible Amorphization, and Anomalous Visible Light Response in Organolead Bromide Perovskite, **J. Am. Chem. Soc. 137 (2015)** 11144–11149. https://doi.org/10.1021/jacs.5b06346.

[80] A. Francisco-López, B. Charles, O. J. Weber, M. I. Alonso, M. Garriga, M. Campoy-Quiles, M. T. Weller, A.R. Goñi, Pressure-Induced Locking of Methylammonium Cations versus Amorphization in Hybrid Lead Iodide Perovskites, J**. Phys. Chem. C. 122 (2018)** 22073–22082. https://doi.org/10.1021/acs.jpcc.8b05188.

[81] L. Zhang, C. Liu, L. Wang, C. Liu, K. Wang, B. Zou, Pressure-Induced Emission Enhancement, Band-Gap Narrowing, and Metallization of Halide Perovskite $Cs_3Bi_2I_9$, **Angew. Chemie Int. Ed. 57 (2018)** 11213–11217. https://doi.org/10.1002/anie.201804310.

[82] M. Szafrański, A. Katrusiak, Mechanism of Pressure-Induced Phase Transitions, Amorphization, and Absorption-Edge Shift in Photovoltaic Methylammonium Lead Iodide, **J. Phys. Chem. Lett. 7 (2016)** 3458–3466. https://doi.org/10.1021/acs.jpclett.6b01648.

[83] L. Kong, G. Liu, J. Gong, Q. Hu, R.D. Schaller, P. Dera, D. Zhang, Z. Liu, W. Yang, K. Zhu, Y. Tang, C. Wang, S.-H. Wei, T. Xu, H. Mao, Simultaneous band-gap narrowing and carrier-lifetime prolongation of organic–inorganic trihalide perovskites, **Proc. Natl. Acad. Sci. 113 (2016)** 8910–8915. https://doi.org/10.1073/pnas.1609030113.

[84] L. Zhang, Q. Zeng, K. Wang, Pressure-Induced Structural and Optical Properties of Inorganic Halide Perovskite $CsPbBr_3$, **J. Phys. Chem. Lett. 8 (2017)** 3752–3758. https://doi.org/10.1021/acs.jpclett.7b01577.

[85] L. Zhang, L. Wang, K. Wang, B. Zou, Pressure-Induced Structural Evolution and Optical Properties of Metal-Halide Perovskite $CsPbCl_3$, **J. Phys. Chem. C. 122 (2018)** 15220–15225. https://doi.org/10.1021/acs.jpcc.8b05397.

[86] G. Yuan, S. Qin, X. Wu, H. Ding, A. Lu, Pressure-induced phase transformation of $CsPbI_3$ by X-ray diffraction and Raman spectroscopy, **Phase Transitions. 91 (2018)** 38–47. https://doi.org/10.1080/01411594.2017.1357180.

[87] Z. Zhao, F. Gu, H. Rao, S. Ye, Z. Liu, Z. Bian, C. Huang, Metal Halide Perovskite

Materials for Solar Cells with Long-Term Stability, **Adv. Energy Mater. 9 (2019)** 1802671. https://doi.org/10.1002/aenm.201802671.

[88] A. Mahapatra, D. Prochowicz, M.M. Tavakoli, S. Trivedi, P. Kumar, P. Yadav, A review of aspects of additive engineering in perovskite solar cells, **J. Mater. Chem. A. 8 (2019)** 27–54. https://doi.org/10.1039/c9ta07657c.

[89] L. Liang, P. Gao, Lead-Free Hybrid Perovskite Absorbers for Viable Application: Can We Eat the Cake and Have It too?, **Adv. Sci. 5 (2018)**. https://doi.org/10.1002/advs.201700331.

[90] X. Wang, T. Zhang, Y. Lou, Y. Zhao, All inorganic lead-free perovskite for optoelectronic applications, **Mater. Chem. Front. (2019)**. https://doi.org/10.1039/c8qm00611c.

[91] Z. Xiao, Z. Song, Y. Yan, From Lead Halide Perovskites to Lead-Free Metal Halide Perovskites and Perovskite Derivatives, **Adv. Mater. 31 (2019)** 1–22. https://doi.org/10.1002/adma.201803792.

[92] L. Meng, J. You, Y. Yang, Addressing the stability issue of perovskite solar cells for commercial applications, **Nat. Commun. 9 (2018)** 5265. https://doi.org/10.1038/s41467-018-07255-1.

[93] G. Grancini, M.K. Nazeeruddin, Dimensional tailoring of hybrid perovskites for photovoltaics, **Nat. Rev. Mater. 4 (2019)** 4–22. https://doi.org/10.1038/s41578-018-0065-0.

[94] M. Liu, A. Matuhina, H. Zhang, P. Vivo, Advances in the stability of halide perovskite nanocrystals, **Materials. 12 (2019)**. https://doi.org/10.3390/ma12223733.

[95] F. Li, M. Liu, Recent efficient strategies for improving the moisture stability of perovskite solar cells, **J. Mater. Chem. A. 5 (2017)** 15447–15459. https://doi.org/10.1039/c7ta01325f.

[96] J. Li, C. C. Stoumpos, G.G. Trimarchi, I. Chung, L. Mao, M. Chen, M.R. Wasielewski, L. Wang, M.G. Kanatzidis, Air-Stable Direct Bandgap Perovskite Semiconductors: All-Inorganic Tin-Based Heteroleptic Halides $A_xSnCl_yI_z$ (A = Cs, Rb), **Chem. Mater. 30 (2018)** 4847–4856. https://doi.org/10.1021/acs.chemmater.8b02232.

[97] D. H. Cao, C.C. Stoumpos, O.K. Farha, J.T. Hupp, M.G. Kanatzidis, 2D Homologous Perovskites as Light-Absorbing Materials for Solar Cell Applications, **J. Am. Chem. Soc. 137 (2015)** 7843–7850. https://doi.org/10.1021/jacs.5b03796.

[98] C. Liu, J. Sun, W.L. Tan, J. Lu, T.R. Gengenbach, C.R. McNeill, Z. Ge, Y.-B. Cheng, U. Bach, Alkali Cation Doping for Improving the Structural Stability of 2D Perovskite in 3D/2D PSCs, **Nano Lett. 20 (2020)** 1240–1251. https://doi.org/10.1021/acs.nanolett.9b04661.

[99] F. A. Lima, M.E. Saleta, R. J. S. Pagliuca, M.A. Eleotério, R.D. Reis, J.F. Júnior, B. Meyer, E. M. Bittar, N. M. Souza-Neto, E. Granado, XDS: A flexible beamline for X-

ray diffraction and spectroscopy at the Brazilian synchrotron, **J. Synchrotron Radiat. 23 (2016)** 1538–1549. https://doi.org/10.1107/S160057751601403X.

[100] P. Willmott, Synchrotron Physics, in: An Introd. to Synchrotron Radiat., **John Wiley & Sons, Ltd, Chichester, UK, 2011**: pp. 39–86. https://doi.org/10.1002/9781119970958.ch3.

[101] Y. Hasegawa, S. Higaki, S. Takahashi, M. Morohashi, Fundamentals of Powder Diffraction and Structural Characterization of Materials, **Springer US, Boston, MA, 2009**. https://doi.org/10.1007/978-0-387-09579-0.

[102] A.P. Hammersley, S.O. Svensson, M. Hanfland, A.N. Fitch, D. Hausermann, Two-dimensional detector software: From real detector to idealised image or two-theta scan, **High Press. Res. 14 (1996)** 235–248. https://doi.org/10.1080/08957959608201408.

[103] S. W. Cheong, M. Mostovoy, Multiferroics: a magnetic twist for ferroelectricity, **Nat. Mater. 6 (2007)** 13–20. https://doi.org/10.1038/nmat1804.

[104] Y. Shi, Y. Pu, Q. Zhang, J. Li, L. Guo, Dielectric and multiferroic properties of two-layered SrBi 2 $Nb_{2x}Fe_xO_9$ Aurivillius compounds, **Ceramics International 44 (2018)** 61–64. https://doi.org/10.1016/j.ceramint.2018.08.251.

[105] Y. Shi, Y. Pu, J. Li, R. Shi, W. Wang, Q. Zhang, L. Guo, Structure , dielectric and multiferroic properties of three-layered aurivillius, **Ceram. Int. 45 (2019)** 9283–9287. https://doi.org/10.1016/j.ceramint.2019.01.129.

[106] X. Zuo, M. Zhang, E. He, B. Guan, Y. Qin, J. Yang, X. Zhu, J. Dai, Structural, magnetic, and dielectric properties of W/Cr co-substituted Aurivillius $Bi_5FeTi_3O_{15}$, **J. Alloys Compd. 726 (2017)** 1040–1046. https://doi.org/10.1016/j.jallcom.2017.08.077.

[107] H. Schmid, X-ray room temperature structure from single crystal data, powder diffraction measurements and optical studies of the aurivillius phase $Bi_5(Ti_3Fe)O_{15}$, **Ferroelectrics. 129 (1992)** 101–112. https://doi.org/10.1080/00150199208016980.

[108] T. Pikula, J. Dzik, P. Guzdek, V.I. Mitsiuk, Z. Surowiec, R. Panek, E. Jartych, Magnetic properties and magnetoelectric coupling enhancement in $Bi_5Ti_3FeO_{15}$ ceramics, **Ceram. Int. 43 (2017)** 11442–11449. https://doi.org/10.1016/j.ceramint.2017.06.008.

[109] H. Zhao, H. Kimura, Z. Cheng, M. Osada, J. Wang, X. Wang, S. Dou, Y. Liu, J. Yu, T. Matsumoto, T. Tohei, N. Shibata, Y. Ikuhara, Large magnetoelectric coupling in magnetically short-range ordered $Bi_5Ti_3FeO_{15}$ film, **Sci. Rep. 4 (2015)** 5255. https://doi.org/10.1038/srep05255.

[110] R.S. Singh, T. Bhimasankaram, G.S. Kumar, S.V. Suryanarayana, Dielectric and magnetoelectric properties of $Bi_5FeTi_3O_{15}$, **Solid State Commun. 91 (1994)** 567–569. https://doi.org/10.1016/0038-1098(94)90376-X.

[111] Y. Zhao, H. Fan, G. Liu, Z. Liu, X. Ren, Ferroelectric, piezoelectric properties and magnetoelectric coupling behavior in aurivillius $Bi_5Ti_3FeO_{15}$ multiferroic nanofibers by electrospinning, **J. Alloys Compd. 675 (2016)** 441–447.

https://doi.org/10.1016/j.jallcom.2016.03.017.

[112] X. Zuo, S. Zhu, J. Bai, E. He, Z. Hui, P. Zhang, D. Song, W. Song, J. Yang, X. Zhu, J. Dai, Enhanced multiferroicity and narrow band gap in B-site Co-doped Aurivillius $Bi_5FeTi_3O_{15}$, **Ceram. Int. 45 (2019)** 137–143. https://doi.org/10.1016/j.ceramint.2018.09.144.

[113] L. Cao, Z. Ding, X. Liu, J. Ren, Y. Chen, M. Ouyang, X. Chen, F. Yang, Photovoltaic properties of Aurivillius $Bi_4NdTi_3FeO_{15}$ ceramics with different orientations, **J. Alloys Compd. 800 (2019)** 134–139. https://doi.org/10.1016/j.jallcom.2019.05.307.

[114] S. Kooriyattil, R.K. Katiyar, S.P. Pavunny, G. Morell, R.S. Katiyar, Photovoltaic properties of Aurivillius phase $Bi_5FeTi_3O_{15}$ thin films grown by pulsed laser deposition, **Appl. Phys. Lett. 105 (2014)** 072908. https://doi.org/10.1063/1.4893784.

[115] Y. Li, M. Bian, N. Zhang, W. Bai, J. Yang, Y. Zhang, X. Tang, J. Chu, Mn-doping composition dependence of the structures, electrical and magnetic properties, and domain structure/switching of Aurivillius $Bi_5Ti_3FeO_{15}$ films, **Ceram. Int. 45 (2019)** 8634–8639. https://doi.org/10.1016/j.ceramint.2019.01.183.

[116] D. Prajapat, A. Sagdeo, V.R. Reddy, Structural , magnetic and dielectric properties of vanadium substituted four layered Aurivillius $Bi_5FeTi_3O_{15}$ ceramics, **Ceram. Int. 45 (2019)** 19093–19097. https://doi.org/10.1016/j.ceramint.2019.06.154.

[117] C. H. Hervoches, A. Snedden, R. Riggs, S. H. Kilcoyne, P. Manuel, P. Lightfoot, Structural Behavior of the Four-Layer Aurivillius-Phase Ferroelectrics $SrBi_4Ti_4O_{15}$ and $Bi_5Ti_3FeO_{15}$, **J. Solid State Chem. 164 (2002)** 280–291. https://doi.org/10.1006/jssc.2001.9473.

[118] J. B. Li, Y.P. Huang, G.H. Rao, G.Y. Liu, J. Luo, J.R. Chen, J.K. Liang, Ferroelectric transition of Aurivillius compounds $Bi_5Ti_3FeO_{15}$ and $Bi_6Ti_3Fe_2O_{18}$, **Appl. Phys. Lett. 96 (2010)** 222903. https://doi.org/10.1063/1.3447372.

[119] C. H. Hervoches, P. Lightfoot, A Variable-Temperature Powder Neutron Diffraction Study of Ferroelectric $Bi_4Ti_3O_{12}$, **Chem. Mater. 11 (1999)** 3359–3364. https://doi.org/10.1021/cm991090d.

[120] P. P. Jiang, Z. H. Duan, L. P. Xu, X. L. Zhang, Y.W. Li, Z. G. Hu, J. H. Chu, Phase transformation in multiferroic $Bi_5Ti_3FeO_{15}$ ceramics by temperature-dependent ellipsometric and Raman spectra: An interband electronic transition evidence, **J. Appl. Phys. 115 (2014)** 0–6. https://doi.org/10.1063/1.4866421.

[121] A. Snedden, C. H. Hervoches, P. Lightfoot, Ferroelectric phase transitions in $SrBi_2Nb_2O_9$ and $Bi_5Ti_3FeO_{15}$: A powder neutron diffraction study, **Phys. Rev. B. 67 (2003)** 092102. https://doi.org/10.1103/PhysRevB.67.092102.

[122] B. J. Kennedy, Q. Zhou, Ismunandar, Y. Kubota, K. Kato, Cation disorder and phase transitions in the four-layer ferroelectric Aurivillius phases $ABi_4Ti_4O_{15}$ (A=Ca, Sr, Ba, Pb), **J. Solid State Chem. 181 (2008)** 1377–1386. https://doi.org/10.1016/j.jssc.2008.02.015.

[123] M. Mączka, W. Paraguassu, L. Macalik, P.T.C. Freire, J. Hanuza, J. Mendes Filho, A Raman scattering study of pressure-induced phase transitions in nanocrystalline Bi_2MoO_6, **J. Phys. Condens. Matter. 23 (2011)** 045401. https://doi.org/10.1088/0953-8984/23/4/045401.

[124] M. Maczka, W. Paraguassu, A. G. S. Filho, P.T.C. Freire, J.M. Filho, J. Hanuza, Phonon-instability-driven phase transitions in ferroelectric Bi_2WO_6: Eu^{3+}: High-pressure Raman and photoluminescence studies, **Phys. Rev. B Condens. Matter Mater. Phys. 77 (2008)** 1–9. https://doi.org/10.1103/PhysRevB.77.094137.

[125] M. Maczka, W. Paraguassu, P.T.C. Freire, a. G. Souza Filho, J. Mendes Filho, J. Hanuza, Lattice dynamics and pressure-induced phase transitions in $Bi_2W_2O_9$: High-pressure Raman study, **Phys. Rev. B. 81 (2010)** 104301. https://doi.org/10.1103/PhysRevB.81.104301.

[126] M. Maczka, A.G. Souza Filho, W. Paraguassu, P.T.C. Freire, J. Mendes Filho, J. Hanuza, Pressure-induced structural phase transitions and amorphization in selected molybdates and tungstates, **Prog. Mater. Sci. 57 (2012)** 1335–1381. https://doi.org/10.1016/j.pmatsci.2012.01.001.

[127] P. R. Scott, J.A. Crow, M. MacZka, M.B. Kruger, An X-ray diffraction study of pressure-induced phase transitions in Bi_2MoO_6, **J. Solid State Chem. 194 (2012)** 15–18. https://doi.org/10.1016/j.jssc.2012.07.044.

[128] J. Rodriguez-Carvajal, "Fullprof: A Program for Rietveld Refinement and Pattern Matching Analysis.," **Abstr. Satell. Meet. Powder Diffr. XV Congr. IUCr. (1990)** 127.

[129] E. Kroumova, M.L. Aroyo, J.M. Perez-Mato, A. Kirov, C. Capillas, S. Ivantchev, H. Wondratschek, Bilbao Crystallographic Server: Useful databases and tools for phase-transition studies, **Phase Transitions. 76 (2003)** 155–170. https://doi.org/10.1080/0141159031000076110.

[130] A. Nonato, C.W.A. Paschoal, E.N. Silva, A.P. Ayala, R.L. Moreira, M.W. Lufaso, Optical phonon features in ferroelectric $Bi_3Fe_{1/2}Nb_{3/2}O_9$, **Vib. Spectrosc. 63 (2012)** 409–417. https://doi.org/10.1016/j.vibspec.2012.09.013.

[131] X. Mao, H. Sun, W. Wang, Y. Lu, X. Chen, Effects of Co-substitutes on multiferroic properties of $Bi_5FeTi_3O_{15}$ ceramics, **Solid State Commun. 152 (2012)** 483–487. https://doi.org/10.1016/j.ssc.2012.01.001.

[132] S. Kojima, R. Imaizumi, S. Hamazaki, M. Takashige, Raman scattering study of bismuth layer-structure ferroelectrics, **Jpn. J. Appl. Phys. 33 (1994)** 5559–5564. https://doi.org/10.1143/JJAP.33.5559.

[133] P.P. Jiang, X.L. Zhang, P. Chang, Z.G. Hu, W. Bai, Y.W. Li, Spin-phonon interactions of multiferroic $Bi_4Ti_3O_{12}$ -$BiFeO_3$ ceramics: Low-temperature Raman scattering and infrared reflectance spectra investigations, **J. Appl. Phys. 115 (2014)** 144101. https://doi.org/10.1063/1.4870054.

[134] S. Kooriyattil, S.P. Pavunny, D. Barrionuevo, R.S. Katiyar, Optical, ferroelectric, and

piezoresponse force microscopy studies of pulsed laser deposited Aurivillius $Bi_5FeTi_3O_{15}$ thin films, **J. Appl. Phys. 116 (2014)**. https://doi.org/10.1063/1.4897556.

[135] W. Wang, J. Sun, X. Mao, X. Chen, Structural and electrical characterization of chemical-solution-derived $Bi_5FeTi_3O_{15}$ thin films, **J. Phys. D. Appl. Phys. 41 (2008)** 155418. https://doi.org/10.1088/0022-3727/41/15/155418.

[136] W. Bai, W.F. Xu, J. Wu, J.Y. Zhu, G. Chen, J. Yang, T. Lin, X.J. Meng, X.D. Tang, J.H. Chu, Investigations on electrical, magnetic and optical behaviors of five-layered Aurivillius $Bi_6Ti_3Fe_2O_{18}$ polycrystalline films, **Thin Solid Films. 525 (2012)** 195–199. https://doi.org/10.1016/j.tsf.2012.10.058.

[137] S. Sun, Y. Ling, R. Peng, M. Liu, X. Mao, X. Chen, R.J. Knize, Y. Lu, Synthesis of Ni-substituted $Bi_7Fe_3Ti_3O_{21}$ ceramics and their superior room temperature multiferroic properties, **RSC Adv. 3 (2013)** 18567. https://doi.org/10.1039/c3ra42589d.

[138] P. R. Graves, G. Hua, S. Myhra, J. G. Thompson, The Raman Modes of the Aurivillius Phases: Temperature and Polarization Dependence, **J. Solid State Chem. 114 (1995)** 112–122. https://doi.org/10.1006/jssc.1995.1017.

[139] R. E. Alonso, A.P. Ayala, A. Castro, J. J. L. Silva, A. López-García, A.R. Paschoal, The orthorhombic to tetragonal phase transition in $Bi_{1.75}Te_{0.25}SrNb_{1.75}Hf_{0.25}O_9$, **J. Phys. Condens. Matter. 16 (2004)** 4139–4148. https://doi.org/10.1088/0953-8984/16/23/028.

[140] G.A. Kourouklis, A. Jayaraman, L.G. Van Uitert, Pressure dependence of the Raman-active modes in $Bi_4Ti_3O_{12}$, **Mater. Lett. 5 (1987)** 116–119. https://doi.org/10.1016/0167-577X(87)90087-5.

[141] M.A. Carpenter, E.K.H. Salje, A. Graeme-Barber, Spontaneous strain as a determinant of thermodynamic properties for phase transitions in minerals, **Eur. J. Mineral. 10 (1998)** 621–691. https://doi.org/10.1127/ejm/10/4/0621.

[142] J. L. Schlenker, G. V. Gibbs, M.B. Boisen, Strain-tensor components expressed in terms of lattice parameters, **Acta Crystallogr. Sect. A. 34 (1978)** 52–54. https://doi.org/10.1107/S0567739478000108.

[143] M.A. Carpenter, R.J. Hemley, H. Mao, High-pressure elasticity of stishovite and the P 4 2 / mnm ⇌ Pnnm phase transition, **J. Geophys. Res. Solid Earth. 105 (2000)** 10807–10816. https://doi.org/10.1029/1999JB900419.

[144] R. J. Hemley, J. Shu, M.A. Carpenter, J. Hu, H.K. Mao, K.J. Kingma, Strain/order parameter coupling in the ferroelastic transition in dense SiO_2, **Solid State Commun. 114 (2000)** 527–532. https://doi.org/10.1016/S0038-1098(00)00099-5.

[145] M. A. Carpenter, C.J. Howard, B.J. Kennedy, K.S. Knight, Strain mechanism for order-parameter coupling through successive phase transitions in $PrAlO_3$, **Phys. Rev. B - Condens. Matter Mater. Phys. 72 (2005)** 1–15. https://doi.org/10.1103/PhysRevB.72.024118.

[146] D. Errandonea, A.B. Garg, J. Pellicer-Porres, D. Martinez-Garcia, C. Popescu,

Monoclinic-tetragonal-monoclinic phase transitions in $Eu_{0.1}Bi_{0.9}VO_4$ under pressure, **J. Phys. Condens. Matter. 31 (2019)** 485401. https://doi.org/10.1088/1361-648x/ab3c31.

[147] D. Andrault, Pressure-Induced Landau-Type Transition in Stishovite, **Science (80) 282 (1998)** 720–724. https://doi.org/10.1126/science.282.5389.720.

[148] Q. Zhou, B. J. Kennedy, C. J. Howard, Structural Studies of the Ferroelectric Phase Transition in $Bi_4Ti_3O_{12}$, **Chem. Mater. 15 (2003)** 5025–5028. https://doi.org/10.1021/cm034580l.

[149] C. H. Hervoches, J. T. S. Irvine, P. Lightfoot, Two high-temperature paraelectric phases in $Sr_{0.85}Bi_{2.1}Ta_2O_9$, **Phys. Rev. B. 64 (2001)** 100102. https://doi.org/10.1103/PhysRevB.64.100102.

[150] J. C. Tolédano, P. Tolédano, Landau Theory Of Phase Transitions: The Application To Structural, Incommensurate, Magnetic And Liquid Crystal Systems, **World Scientific Publishing Co Pte Ltd, 1987**.

[151] J. T. Zhang, X. M. Lu, J. Zhou, H. Sun, F.Z. Huang, J. S. Zhu, Magnetic properties and origins of ferroelectric polarization in multiferroic $CaMn_7O_{12}$, **Phys. Rev. B Condens. Matter Mater. Phys. 87 (2013)** 1–6. https://doi.org/10.1103/PhysRevB.87.075127.

[152] A. Castro-Couceiro, S. Yẫez-Vilar, B. Rivas-Murias, A. Fondado, J. Mira, J. Rivas, M. A. Sẽarís-Rodríguez, Dielectric properties of the charge-ordered mixed oxide $CaMn_7O_{12}$, **J. Phys. Condens. Matter. 18 (2006)** 3803–3815. https://doi.org/10.1088/0953-8984/18/15/023.

[153] S. Yáñez Vilar, A. Castro-Couceiro, B. Rivas-Murias, A. Fondado, J. Mira, J. Rivas, M.A. Senaris-Rodriguez, High dielectric constant in the charge-ordered manganese oxide $CaMn_7O_{12}$, **Zeitschrift Fur Anorg. Und Allg. Chemie. 631 (2005)** 2192–2196. https://doi.org/10.1002/zaac.200570040.

[154] X. Z. Lu, M. H. Whangbo, S. Dong, X. G. Gong, H. J. Xiang, Giant ferroelectric polarization of $CaMn_7O_{12}$ induced by a combined effect of Dzyaloshinskii-Moriya interaction and exchange striction, **Phys. Rev. Lett. 108 (2012)** 1–5. https://doi.org/10.1103/PhysRevLett.108.187204.

[155] K. Cao, R.D. Johnson, N. Perks, F. Giustino, P.G. Radaelli, First-principles study of structurally modulated multiferroic $CaMn_7O_{12}$, **Phys. Rev. B - Condens. Matter Mater. Phys. 91 (2015)** 1–6. https://doi.org/10.1103/PhysRevB.91.064422.

[156] N. J. Perks, R.D. Johnson, C. Martin, L.C. Chapon, P.G. Radaelli, Magneto-orbital helices as a route to coupling magnetism and ferroelectricity in multiferroic $CaMn_7O_{12}$, **Nat. Commun. 3 (2012)** 1276–1277. https://doi.org/10.1038/ncomms2294.

[157] Y.S. Glazkova, N. Terada, Y. Matsushita, Y. Katsuya, M. Tanaka, A. V. Sobolev, I.A. Presniakov, A.A. Belik, High-Pressure Synthesis, Crystal Structures, and Properties of $CdMn_7O_{12}$ and $SrMn_7O_{12}$ Perovskites, **Inorg. Chem. 54 (2015)** 9081–9091. https://doi.org/10.1021/acs.inorgchem.5b01472.

[158] N. Terada, Y.S. Glazkova, A.A. Belik, Differentiation between ferroelectricity and thermally stimulated current in pyrocurrent measurements of multiferroic MMn_7O_{12} (M= Ca, Sr, Cd, Pb), **Phys. Rev. B. 93 (2016)** 12–17. https://doi.org/10.1103/PhysRevB.93.155127.

[159] L. Zhang, N. Terada, R.D. Johnson, D. D. Khalyavin, P. Manuel, Y. Katsuya, M. Tanaka, Y. Matsushita, K. Yamaura, A.A. Belik, High-Pressure Synthesis , Structures , and Properties of Trivalent A - Site-Ordered Quadruple Perovskites RMn_7O_{12} (R = Sm , Eu , Gd , and Tb), **Inorganic Chemistry 57 (2018)**. https://doi.org/10.1021/acs.inorgchem.8b00479.

[160] A. Nonato, B.S. Araujo, A.P. Ayala, A.P. Maciel, S. Yanez-Vilar, M. Sanchez-Andujar, M.A. Senaris-Rodriguez, C.W.A. Paschoal, Spin-phonon and magnetostriction phenomena in $CaMn_7O_{12}$ helimagnet probed by Raman spectroscopy, **Appl. Phys. Lett. 105 (2014)** 1–5. https://doi.org/10.1063/1.4902234.

[161] S. M. Souliou, Y. Li, X. Du, M. Le Tacon, A. Bosak, Soft-phonon-driven orbital order in $CaMn_7O_{12}$, **Phys. Rev. B. 94 (2016)** 1–6. https://doi.org/10.1103/PhysRevB.94.184309.

[162] G. Zhang, S. Dong, Z. Yan, Y. Guo, Q. Zhang, S. Yunoki, Multiferroic properties of $CaMn_7O_{12}$, **Physical Review B 84 (2011)** 6–10. https://doi.org/10.1103/PhysRevB.84.174413.

[163] R. D. Johnson, L.C. Chapon, D. D. Khalyavin, P. Manuel, P. G. Radaelli, C. Martin, Giant improper ferroelectricity in the ferroaxial magnet $CaMn_7O_{12}$, **Phys. Rev. Lett. 108 (2012)** 2–5. https://doi.org/10.1103/PhysRevLett.108.067201.

[164] X. Du, R. Yuan, L. Duan, C. Wang, Y. Hu, Y. Li, Soft vibrational mode associated with incommensurate orbital order in multiferroic $CaMn_7O_{12}$, **Phys. Rev. B - Condens. Matter Mater. Phys. 90 (2014)** 1–7. https://doi.org/10.1103/PhysRevB.90.104414.

[165] R. Przenioslo, I. Sosnowska, E. Suard, A. Hewat, A.N. Fitch, Phase coexistence in the charge ordering transition in $CaMn_7O_{12}$, **J. Phys. Condens. Matter. 14 (2002)** 5747–5753. https://doi.org/10.1088/0953-8984/14/23/308.

[166] A. N. Vasil'ev, O. S. Volkova, New functional materials $AC_3B_4O_{12}$ (Review), **Low Temp. Phys. 33 (2007)** 895–914. https://doi.org/10.1063/1.2747047.

[167] M. N. Iliev, V.G. Hadjiev, M. M. Gospodinov, R. P. Nikolova, M. V. Abrashev, Raman study of phonons in $CaMn_7O_{12}$: Effects of structural modulation and structural transition, **Phys. Rev. B - Condens. Matter Mater. Phys. 89 (2014)** 1–6. https://doi.org/10.1103/PhysRevB.89.214302.

[168] I.. Troyanchuk, A.N. Chobot, Phase transition in $CaMn_3(Mn^{33+}Mn^{4+})O_{12}$ with the perovskite structure, **Crystallogr. Reports. 42 (1997)** 983–989. https://doi.org/10.1134/1.170718.

[169] A. Huon, D. Lee, A. Herklotz, M.R. Fitzsimmons, H. N. Lee, S. J. May, Effect of chemical pressure on the electronic phase transition in $Ca_{1-x}Sr_xMn_7O_{12}$ films, **APL**

Mater. 5 (2017). https://doi.org/10.1063/1.4994089.

[170] A. Le Bail, H. Duroy, J. L. Fourquet, Ab-initio structure determination of $LiSbWO_6$ by X-ray powder diffraction, **Mater. Res. Bull. 23 (1988)** 447–452. https://doi.org/10.1016/0025-5408(88)90019-0.

[171] A. Boultif, D. Louër, Powder pattern indexing with the dichotomy method, **J. Appl. Crystallogr. 37 (2004)** 724–731. https://doi.org/10.1107/S0021889804014876.

[172] T. Roisnel, J. Rodríguez-Carvajal, Win PLOTR: A windows tool for powder diffraction pattern analysis, **Mater. Sci. Forum. 378–381 (2001)** 118–123. https://doi.org/10.4028/www.scientific.net/msf.378-381.118.

[173] P. M. de Wolff, A simplified criterion for the reliability of a powder pattern indexing, **J. Appl. Crystallogr. 1 (1968)** 108–113. https://doi.org/10.1107/S002188986800508X.

[174] A. G. Jolley, D.D. Taylor, N. J. Schreiber, E. D. Wachsman, Structural Investigation of Monoclinic-Rhombohedral Phase Transition in $Na_3Zr_2Si_2PO_{12}$ and Doped NASICON, **J. Am. Ceram. Soc. 98 (2015)** 2902–2907. https://doi.org/10.1111/jace.13692.

[175] T. Hahn, International Tables for Crystallography. Volume A, Space-Group Symmetry, **The International Union Of Crystallography, 2005.**

[176] F. Birch, Finite Elastic Strain of Cubic Crystals, **Phys. Rev. 71 (1947)** 809–824. https://doi.org/10.1103/PhysRev.71.809.

[177] F. D. Murnaghan, The Compressibility Of Media Under Extreme Pressures, **Proc. Natl. Acad. Sci. 30 (1944)** 244–247. https://doi.org/10.1073/pnas.9.11.370.

[178] Y. W. Long, T. Kawakami, W. T. Chen, T. Saito, T. Watanuki, Y. Nakakura, Q.Q. Liu, C.Q. Jin, Y. Shimakawa, Pressure effect on intersite charge transfer in A-site-ordered double-perovskite-structure oxide, **Chem. Mater. 24 (2012)** 2235–2239. https://doi.org/10.1021/cm301267e.

[179] D. Valim, A.G. Souza Filho, P.T.C. Freire, S.B. Fagan, A.P. Ayala, J. Mendes Filho, A. F. L. Almeida, P. B. A. Fechine, A.S.B. Sombra, J. Staun Olsen, L. Gerward, Raman scattering and x-ray diffraction studies of polycrystalline $CaCu_3Ti_4O_{12}$ under high-pressure, **Phys. Rev. B. 70 (2004)** 132103. https://doi.org/10.1103/PhysRevB.70.132103.

[180] T. Leijtens, K.A. Bush, R. Prasanna, M.D. McGehee, Opportunities and challenges for tandem solar cells using metal halide perovskite semiconductors, **Nat. Energy. 3 (2018)** 828–838. https://doi.org/10.1038/s41560-018-0190-4.

[181] W. Yang, F. Igbari, Y. Lou, Z. Wang, L. Liao, Tin Halide Perovskites : Progress and Challenges, **Advanced Energy Materials (2019)** 1–30. https://doi.org/10.1002/aenm.201902584.

[182] M. I. Saidaminov, O. F. Mohammed, O. M. Bakr, Low-Dimensional-Networked Metal Halide Perovskites: The Next Big Thing, **ACS Energy Lett. 2 (2017)** 889–896.

https://doi.org/10.1021/acsenergylett.6b00705.

[183] M. D. Smith, B. A. Connor, H. I. Karunadasa, Tuning the Luminescence of Layered Halide Perovskites, **Chem. Rev. 119 (2019)** 3104–3139. https://doi.org/10.1021/acs.chemrev.8b00477.

[184] M. I. Saidaminov, J. Almutlaq, S. Sarmah, I. Dursun, A.A. Zhumekenov, R. Begum, J. Pan, N. Cho, O. F. Mohammed, O. M. Bakr, Pure Cs_4PbBr_6: Highly Luminescent Zero-Dimensional Perovskite Solids, **ACS Energy Lett. 1 (2016)** 840–845. https://doi.org/10.1021/acsenergylett.6b00396.

[185] Y. Zhang, M. I. Saidaminov, I. Dursun, H. Yang, B. Murali, E. Alarousu, E. Yengel, B. A. Alshankiti, O. M. Bakr, O. F. Mohammed, Zero-Dimensional Cs_4PbBr_6 Perovskite Nanocrystals, **J. Phys. Chem. Lett. 8 (2017)** 961–965. https://doi.org/10.1021/acs.jpclett.7b00105.

[186] H. Tsai, W. Nie, J. C. Blancon, C.C. Stoumpos, R. Asadpour, B. Harutyunyan, A. J. Neukirch, R. Verduzco, J.J. Crochet, S. Tretiak, L. Pedesseau, J. Even, M.A. Alam, G. Gupta, J. Lou, P. M. Ajayan, M. J. Bedzyk, M. G. Kanatzidis, A. D. Mohite, High-efficiency two-dimensional ruddlesden-popper perovskite solar cells, **Nature. 536 (2016)** 312–317. https://doi.org/10.1038/nature18306.

[187] Q. A. Akkerman, E. Bladt, U. Petralanda, Z. Dang, E. Sartori, D. Baranov, A. L. Abdelhady, I. Infante, S. Bals, L. Manna, Fully Inorganic Ruddlesden–Popper Double Cl–I and Triple Cl–Br–I Lead Halide Perovskite Nanocrystals, **Chem. Mater. 31 (2019)** 2182–2190. https://doi.org/10.1021/acs.chemmater.9b00489.

[188] J. Li, Q. Yu, Y. He, C.C. Stoumpos, G. Niu, G.G. Trimarchi, H. Guo, G. Dong, D. Wang, L. Wang, M.G. Kanatzidis, $Cs_2PbI_2Cl_2$, All-Inorganic Two-Dimensional Ruddlesden–Popper Mixed Halide Perovskite with Optoelectronic Response, **J. Am. Chem. Soc. 140 (2018)** 11085–11090. https://doi.org/10.1021/jacs.8b06046.

[189] X. Hong, T. Ishihara, A. V. Nurmikko, Dielectric confinement eff'ect on excitons in PbI_4-based layered semiconductors, **Phys. Rev. B. 45 (1992)** 6961–6964. https://doi.org/10.1103/PhysRevB.45.6961.

[190] D.B. Straus, S. Hurtado Parra, N. Iotov, J. Gebhardt, A.M. Rappe, J.E. Subotnik, J.M. Kikkawa, C.R. Kagan, Direct Observation of Electron-Phonon Coupling and Slow Vibrational Relaxation in Organic-Inorganic Hybrid Perovskites, **J. Am. Chem. Soc. 138 (2016)** 13798–13801. https://doi.org/10.1021/jacs.6b08175.

[191] X. Gong, O. Voznyy, A. Jain, W. Liu, R. Sabatini, Z. Piontkowski, G. Walters, G. Bappi, S. Nokhrin, O. Bushuyev, M. Yuan, R. Comin, D. McCamant, S.O. Kelley, E.H. Sargent, Electron-phonon interaction in efficient perovskite blue emitters, **Nat. Mater. 17 (2018)** 550–556. https://doi.org/10.1038/s41563-018-0081-x.

[192] J. A. Steele, P. Puech, B. Monserrat, B. Wu, R.X. Yang, T. Kirchartz, H. Yuan, G. Fleury, D. Giovanni, E. Fron, M. Keshavarz, E. Debroye, G. Zhou, T.C. Sum, A. Walsh, J. Hofkens, M.B.J. Roeffaers, Role of Electron-Phonon Coupling in the Thermal Evolution of Bulk Rashba-Like Spin-Split Lead Halide Perovskites Exhibiting Dual-Band

Photoluminescence, **ACS Energy Lett. 4 (2019)** 2205–2212. https://doi.org/10.1021/acsenergylett.9b01427.

[193] J. Yin, H. Li, D. Cortecchia, C. Soci, J. L. Brédas, Excitonic and polaronic properties of 2D hybrid organic-inorganic perovskites, **ACS Energy Lett. 2 (2017)** 417–423. https://doi.org/10.1021/acsenergylett.6b00659.

[194] D. B. Straus, C. R. Kagan, Electrons, Excitons, and Phonons in Two-Dimensional Hybrid Perovskites: Connecting Structural, Optical, and Electronic Properties, **J. Phys. Chem. Lett. 9 (2018)** 1434–1447. https://doi.org/10.1021/acs.jpclett.8b00201.

[195] E. Shi, S. Deng, B. Yuan, Y. Gao, Akriti, L. Yuan, C. S. Davis, D. Zemlyanov, Y. Yu, L. Huang, L. Dou, Extrinsic and Dynamic Edge States of Two-Dimensional Lead Halide Perovskites, **ACS Nano. (2019)** acsnano.8b07631. https://doi.org/10.1021/acsnano.8b07631.

[196] M. Baranowski, P. Plochocka, Excitons in Metal-Halide Perovskites, **Adv. Energy Mater. 1903659 (2020)** 1903659. https://doi.org/10.1002/aenm.201903659.

[197] P. Acharyya, K. Maji, K. Kundu, K. Biswas, 2D Nanoplates and Scaled-Up Bulk Polycrystals of Ruddlesden–Popper $Cs_2PbI_2Cl_2$ for Optoelectronic Applications, **ACS Appl. Nano Mater. 3 (2020)** 877–886. https://doi.org/10.1021/acsanm.9b02439.

[198] A. D. Wright, C. Verdi, R. L. Milot, G. E. Eperon, M. A. Pérez-Osorio, H. J. Snaith, F. Giustino, M.B. Johnston, L. M. Herz, Electron-phonon coupling in hybrid lead halide perovskites, **Nat. Commun. 7 (2016)**. https://doi.org/10.1038/ncomms11755.

[199] W. A. Saidi, A. Kachmar, Effects of Electron-Phonon Coupling on Electronic Properties of Methylammonium Lead Iodide Perovskites, **J. Phys. Chem. Lett. 9 (2018)** 7090–7097. https://doi.org/10.1021/acs.jpclett.8b03164.

[200] L. Ni, U. Huynh, A. Cheminal, T.H. Thomas, R. Shivanna, T.F. Hinrichsen, S. Ahmad, A. Sadhanala, A. Rao, Real-Time Observation of Exciton–Phonon Coupling Dynamics in Self-Assembled Hybrid Perovskite Quantum Wells, **ACS Nano. 11 (2017)** 10834–10843. https://doi.org/10.1021/acsnano.7b03984.

[201] S. Baroni, S. de Gironcoli, A. Dal Corso, P. Giannozzi, Phonons and related crystal properties from density-functional perturbation theory, **Rev. Mod. Phys. 73 (2001)** 515–562. https://doi.org/10.1103/RevModPhys.73.515.

[202] A. Togo, I. Tanaka, First principles phonon calculations in materials science, **Scr. Mater. 108 (2015)** 1–5. https://doi.org/10.1016/j.scriptamat.2015.07.021.

[203] M. Lazzeri, M. Calandra, F. Mauri, Anharmonic phonon frequency shift in MgB_2, **Phys. Rev. B - Condens. Matter Mater. Phys. 68 (2003)** 2–5. https://doi.org/10.1103/PhysRevB.68.220509.

[204] T. Hart, R. Aggarwal, B. Lax, Temperature Dependence of Raman Scattering in Silicon, **Phys. Rev. B. 1 (1970)** 638–642. https://doi.org/10.1103/PhysRevB.1.638.

[205] M. Balkanski, R.F. Wallis, E. Haro, Anharmonic effects in light scattering due to optical phonons in silicon, **Phys. Rev. B. 28 (1983)** 1928–1934. https://doi.org/10.1103/PhysRevB.28.1928.

[206] H.M. Eiter, P. Jaschke, R. Hackl, A. Bauer, M. Gangl, C. Pfleiderer, Raman study of the temperature and magnetic-field dependence of the electronic and lattice properties of MnSi, **Phys. Rev. B - Condens. Matter Mater. Phys. 90 (2014)** 1–18. https://doi.org/10.1103/PhysRevB.90.024411.

[207] Y. Guo, O. Yaffe, T.D. Hull, J.S. Owen, D.R. Reichman, L.E. Brus, Dynamic emission Stokes shift and liquid-like dielectric solvation of band edge carriers in lead-halide perovskites, **Nat. Commun. 10 (2019)** 1–8. https://doi.org/10.1038/s41467-019-09057-5.

[208] C. C. Stoumpos, C.M.M. Soe, H. Tsai, W. Nie, J.-C. Blancon, D.H. Cao, F. Liu, B. Traoré, C. Katan, J. Even, A.D. Mohite, M.G. Kanatzidis, High Members of the 2D Ruddlesden-Popper Halide Perovskites: Synthesis, Optical Properties, and Solar Cells of $(CH_3(CH_2)_3NH_3)_2(CH_3NH_3)_4Pb_5I_{16}$, **Chem. 2 (2017)** 427–440. https://doi.org/10.1016/j.chempr.2017.02.004.

[209] A. Dutta, R.K. Behera, S. Deb, S. Baitalik, N. Pradhan, Doping Mn(II) in All-Inorganic Ruddlesden–Popper Phase of Tetragonal $Cs_2PbCl_2I_2$ Perovskite Nanoplatelets, **J. Phys. Chem. Lett. 10 (2019)** 1954–1959. https://doi.org/10.1021/acs.jpclett.9b00738.

[210] Y. P. Varshni, Temperature dependence of the energy gap in semiconductors, **Physica. 34 (1967)** 149–154. https://doi.org/10.1016/0031-8914(67)90062-6.

[211] L. Malikova, W. Krystek, F.H. Pollak, N. Dai, A. Cavus, M. Tamargo, Temperature dependence of the direct gaps of ZnSe AnSe, **Phys. Rev. B - Condens. Matter Mater. Phys. 54 (1996)** 1819–1824. https://doi.org/10.1103/PhysRevB.54.1819.

[212] S. Rudin, T.L. Reinecke, B. Segall, Temperature-dependent exciton linewidths in semiconductors, **Phys. Rev. B. 42 (1990)** 11218–11231. https://doi.org/10.1103/PhysRevB.42.11218.

[213] S. Rudin, T.L. Reinecke, Temperature-dependent exciton linewidths in semiconductor quantum wells, **Phys. Rev. B. 41 (1990)** 3017–3027. https://doi.org/10.1103/PhysRevB.41.3017.

[214] J.A. Steele, P. Puech, M. Keshavarz, R. Yang, S. Banerjee, E. Debroye, C.W. Kim, H. Yuan, N.H. Heo, J. Vanacken, A. Walsh, J. Hofkens, M.B.J. Roeffaers, Giant Electron–Phonon Coupling and Deep Conduction Band Resonance in Metal Halide Double Perovskite, **ACS Nano. 12 (2018)** 8081–8090. https://doi.org/10.1021/acsnano.8b02936.

[215] K.M. McCall, C.C. Stoumpos, S.S. Kostina, M.G. Kanatzidis, B.W. Wessels, Strong Electron–Phonon Coupling and Self-Trapped Excitons in the Defect Halide Perovskites $A_3M_2I_9$ (A = Cs, Rb; M = Bi, Sb), **Chem. Mater. 29 (2017)** 4129–4145. https://doi.org/10.1021/acs.chemmater.7b01184.

[216] J. Lee, E.S. Koteles, M.O. Vassell, Luminescence linewidths of excitons in GaAs quantum wells below 150 K, **Phys. Rev. B. 33 (1986)** 5512–5516. https://doi.org/10.1103/PhysRevB.33.5512.

[217] Z. W. Wang, Y. Xiao, J. P. Deng, Y. Cui, Z. Q. Li, Multiphonon Raman scattering mediated by the exciton states in monolayer transition metal chalcogenides, **Phys. Rev. B. 100 (2019)** 125308. https://doi.org/10.1103/PhysRevB.100.125308.

[218] E. Mulazzi, Raman scattering in resonance with the exciton transition in pure polar crystals, **Phys. Rev. Lett. 25 (1970)** 228–231. https://doi.org/10.1103/PhysRevLett.25.228.

[219] Q. A. Akkerman, A.L. Abdelhady, L. Manna, Zero-Dimensional Cesium Lead Halides: History, Properties, and Challenges, **J. Phys. Chem. Lett. 9 (2018)** 2326–2337. https://doi.org/10.1021/acs.jpclett.8b00572.

[220] M. E. Kamminga, H. H. Fang, M. R. Filip, F. Giustino, J. Baas, G. R. Blake, M. A. Loi, T.T.M. Palstra, Confinement Effects in Low-Dimensional Lead Iodide Perovskite Hybrids, **Chem. Mater. 28 (2016)** 4554–4562. https://doi.org/10.1021/acs.chemmater.6b00809.

[221] M. Hu, C. Ge, J. Yu, J. Feng, Mechanical and Optical Properties of Cs 4 BX 6 (B = Pb, Sn; X = Cl, Br, I) Zero-Dimension Perovskites, **J. Phys. Chem. C. 121 (2017)** 27053–27058. https://doi.org/10.1021/acs.jpcc.7b10629.

[222] N. Wang, W. Liu, Q. Zhang, Perovskite-Based Nanocrystals: Synthesis and Applications beyond Solar Cells, **Small Methods. 2 (2018)** 1700380. https://doi.org/10.1002/smtd.201700380.

[223] S. Seth, A. Samanta, Fluorescent Phase-Pure Zero-Dimensional Perovskite-Related Cs_4PbBr_6 Microdisks: Synthesis and Single-Particle Imaging Study, **J. Phys. Chem. Lett. 8 (2017)** 4461–4467. https://doi.org/10.1021/acs.jpclett.7b02100.

[224] H. Zhang, X. Liu, J. Dong, H. Yu, C. Zhou, B. Zhang, Y. Xu, W. Jie, Centimeter-Sized Inorganic Lead Halide Perovskite $CsPbBr_3$ Crystals Grown by an Improved Solution Method, **Cryst. Growth Des. 17 (2017)** 6426–6431. https://doi.org/10.1021/acs.cgd.7b01086.

[225] L. Wang, K. Wang, B. Zou, Pressure-Induced Structural and Optical Properties of Organometal Halide Perovskite-Based Formamidinium Lead Bromide, **J. Phys. Chem. Lett. 7 (2016)** 2556–2562. https://doi.org/10.1021/acs.jpclett.6b00999.

[226] A. Jaffe, Y. Lin, C.M. Beavers, J. Voss, W.L. Mao, H.I. Karunadasa, High-pressure single-crystal structures of 3D lead-halide hybrid perovskites and pressure effects on their electronic and optical properties, **ACS Cent. Sci. 2 (2016)** 201–209. https://doi.org/10.1021/acscentsci.6b00055.

[227] J. C. Beimborn, L. M. G. Hall, P. Tongying, G. Dukovic, J.M. Weber, Pressure Response of Photoluminescence in Cesium Lead Iodide Perovskite Nanocrystals, **J. Phys. Chem. C. 122 (2018)** 11024–11030. https://doi.org/10.1021/acs.jpcc.8b03280.

[228] G. Liu, L. Kong, J. Gong, W. Yang, H. Mao, Q. Hu, Z. Liu, R.D. Schaller, D. Zhang, T. Xu, Pressure-Induced Bandgap Optimization in Lead-Based Perovskites with Prolonged Carrier Lifetime and Ambient Retainability, **Adv. Funct. Mater. 27 (2017)** 1604208. https://doi.org/10.1002/adfm.201604208.

[229] J. H. Cha, J. H. Han, W. Yin, C. Park, Y. Park, T.K. Ahn, J.H. Cho, D. Y. Jung, Photoresponse of $CsPbBr_3$ and Cs_4PbBr_6 Perovskite Single Crystals, **J. Phys. Chem. Lett. 8 (2017)** 565–570. https://doi.org/10.1021/acs.jpclett.6b02763.

[230] M. De Bastiani, I. Dursun, Y. Zhang, B.A. Alshankiti, X.-H. Miao, J. Yin, E. Yengel, E. Alarousu, B. Turedi, J.M. Almutlaq, M.I. Saidaminov, S. Mitra, I. Gereige, A. AlSaggaf, Y. Zhu, Y. Han, I.S. Roqan, J.-L. Bredas, O.F. Mohammed, O.M. Bakr, Inside Perovskites: Quantum Luminescence from Bulk Cs_4PbBr_6 Single Crystals, **Chem. Mater. 29 (2017)** 7108–7113. https://doi.org/10.1021/acs.chemmater.7b02415.

[231] P. Arunkumar, H. Bin Cho, K. H. Gil, S. Unithrattil, Y.H. Kim, W. Bin Im, Probing molecule-like isolated octahedra via—phase stabilization of zero-dimensional cesium lead halide nanocrystals, **Nat. Commun. 9 (2018)** 4691. https://doi.org/10.1038/s41467-018-07097-x.

[232] J. Yin, P. Maity, M. De Bastiani, I. Dursun, O.M. Bakr, J.-L. Brédas, O.F. Mohammed, Molecular behavior of zero-dimensional perovskites, **Sci. Adv. 3 (2017)** e1701793. https://doi.org/10.1126/sciadv.1701793.

[233] W.G. Fateley, N.T. McDevitt, F.F. Bentley, Infrared and Raman Selection Rules for Lattice Vibrations: The Correlation Method, **Appl. Spectrosc. 25 (1971)** 155–173. https://doi.org/10.1366/000370271779948600.

[234] D. L. Rousseau, R. P. Bauman, S.P.S. Porto, Normal mode determination in crystals, **J. Raman Spectrosc. 10 (1981)** 253–290. https://doi.org/10.1002/jrs.1250100152.

[235] Z. Qin, S. Dai, V.G. Hadjiev, C. Wang, L. Xie, Y. Ni, C. Wu, G. Yang, S. Chen, L. Deng, Q. Yu, G. Feng, Z.M. Wang, J. Bao, Revealing the Origin of Luminescence Center in 0D Cs_4PbBr_6 Perovskite, **Chem. Mater. 31 (2019)** 9098–9104. https://doi.org/10.1021/acs.chemmater.9b03426.

[236] V. Dracopoulos, B. Gilbert, B. Brrensen, G. M. Photiadis, G. N. Papatheodorou, Vibrational modes and structure of rare earth halide–alkali halide binary melts YBr_3–ABr (A=Li, K, Cs) and YF_3–KF, J**. Chem. Soc. Faraday Trans. 93 (1997)** 3081–3088. https://doi.org/10.1039/a701864i.

[237] J. Yin, Y. Zhang, A. Bruno, C. Soci, O.M. Bakr, J.L. Brédas, O.F. Mohammed, Intrinsic Lead Ion Emissions in Zero-Dimensional Cs_4PbBr_6 Nanocrystals, **ACS Energy Lett. 2 (2017)** 2805–2811. https://doi.org/10.1021/acsenergylett.7b01026.

[238] Y. Wang, D. Yu, Z. Wang, X. Li, X. Chen, V. Nalla, H. Zeng, H. Sun, Solution-Grown $CsPbBr_3$/Cs_4PbBr_6 Perovskite Nanocomposites: Toward Temperature-Insensitive Optical Gain, **Small. 13 (2017)** 1–8. https://doi.org/10.1002/smll.201701587.

[239] N. Riesen, M. Lockrey, K. Badek, H. Riesen, On the origins of the green luminescence

in the "zero-dimensional perovskite" Cs_4PbBr_6 : conclusive results from cathodoluminescence imaging, **Nanoscale. 11 (2019)** 3925–3932. https://doi.org/10.1039/C8NR09255A.

[240] W. Chen, X. Xin, Z. Zang, X. Tang, C. Li, W. Hu, M. Zhou, J. Du, Tunable photoluminescence of $CsPbBr_3$ perovskite quantum dots for light emitting diodes application, **J. Solid State Chem. 255 (2017)** 115–120. https://doi.org/10.1016/j.jssc.2017.06.006.

[241] S. K. Balakrishnan, P. V. Kamat, Ligand Assisted Transformation of Cubic $CsPbBr_3$ Nanocrystals into Two-Dimensional $CsPb_2Br_5$ Nanosheets, **Chem. Mater. 30 (2018)** 74–78. https://doi.org/10.1021/acs.chemmater.7b04142.

[242] J. Xu, W. Huang, P. Li, D.R. Onken, C. Dun, Y. Guo, K.B. Ucer, C. Lu, H. Wang, S.M. Geyer, R.T. Williams, D.L. Carroll, Imbedded Nanocrystals of $CsPbBr_3$ in Cs_4PbBr_6 : Kinetics, Enhanced Oscillator Strength, and Application in Light-Emitting Diodes, **Adv. Mater. 29 (2017)** 1703703. https://doi.org/10.1002/adma.201703703.

[243] Q. A. Akkerman, S. Park, E. Radicchi, F. Nunzi, E. Mosconi, F. De Angelis, R. Brescia, P. Rastogi, M. Prato, L. Manna, Nearly Monodisperse Insulator Cs_4PbX_6 (X = Cl, Br, I) Nanocrystals, Their Mixed Halide Compositions, and Their Transformation into $CsPbX_3$ Nanocrystals, **Nano Lett. 17 (2017)** 1924–1930. https://doi.org/10.1021/acs.nanolett.6b05262.

[244] D. Han, H. Shi, W. Ming, C. Zhou, B. Ma, B. Saparov, Y.Z. Ma, S. Chen, M.H. Du, Unraveling luminescence mechanisms in zero-dimensional halide perovskites, **J. Mater. Chem. C. 6 (2018)** 6398–6405. https://doi.org/10.1039/c8tc01291a.

[245] H. Zhang, Q. Liao, Y. Wu, J. Chen, Q. Gao, H. Fu, Pure zero-dimensional Cs_4PbBr_6 single crystal rhombohedral microdisks with high luminescence and stability, **Phys. Chem. Chem. Phys. 19 (2017)** 29092–29098. https://doi.org/10.1039/c7cp06097a.